QCD Studies at LEP

Simon Bird

THE UNIVERSITY
of MANCHESTER

Particle Physics Group
Department of Physics and Astronomy

October 20, 1998

A thesis submitted to The University of Manchester for the degree of
Doctor of Philosophy in the Faculty of Science and Engineering

Contents

List of Figures

List of Tables

Abstract

Three-jet events with a symmetry such that the two lower energy jets were of approximately equal energy were selected from hadronic Z^0 decays observed in the OPAL detector at LEP. A tag based on the energy profile of the jet was used to anti-tag gluon jets and a gluon jet enhanced sample was compared with the inclusive lower energy jet sample. The tracks in each sample were analysed using an extended maximum likelihood fit to dE/dx information to extract the identified charged particle rates for each sample. A process of algebraic decomposition was then used to find the rates for pure gluon and quark jets. The ratios of identified charged particle production rates in gluon and quark jets were found to be

$1.10 \pm 0.01 \pm 0.02$ for all charged particles,
$1.17 \pm 0.01 \pm 0.05$ for $\pi^{\pm}$,
$0.96 \pm 0.03 \pm 0.12$ for $K^{\pm}$ and
$1.12 \pm 0.10 \pm 0.11$ for $p(\overline{p})$.

where the first errors are statistical and the second are systematic. The results were found to be consistent with previous analyses. The JETSET Monte Carlo results were in good agreement with the measurements, with the exception of that for $p(\overline{p})$. Charged particle momentum spectra in hadronic events have also been investigated at LEPII energies and the charged multiplicity and the peak of the ξ_p distribution have been studied. The predictions from Monte Carlo and analytic calculations were found to be in good overall agreement with the data, apart from the COJETS event generator, which does not implement coherent gluon emission.

Declaration

No portion of the work referred to in this thesis has been submitted in support of an application for another degree or qualification of this or any other university or other institute of learning.

The Author

Simon Bird attended Wood Green High School and Sixth Form, Wednesbury before reading physics as an undergraduate at Manchester University. The work presented here was undertaken at Manchester and CERN, Geneva.

Acknowledgements

As with all theses, many people deserve to be thanked for their support and encouragement. The members of the Manchester HEP group and the OPAL collaboration provided the hardware and the environment for the analysis. The financial support of PPARC is gratefully acknowledged. Special thanks must go to my supervisor, George Lafferty, for three years of help and putting up with often silly questions. Thanks must also go to Fred Loebinger, Andy Walkden, Brian Cox, David Eatough, David Futyan, Stan Bentvelsen, Stefan Kluth, Luis del Pozo, David Hutchcroft, Stephan Baumann and Michael Hauschild. Back in Manchester, Helen G, Andy M and Alex helped immensely.

In Geneva, many friends were made and I am grateful to them all; I'd particularly like to thank Scott, Chris, Helen, Kyle, Jon and Paul for the many Swiss beers we consumed. Outside particle physics, time was spent in French classes, where I'd like to thank David, Joe and Marc for bringing me back down to earth and giving a different perspective on life. There are many others who contributed, and they too deserve their share of the thanks.

A few more people deserve a special mention. I'd like to thank my parents and my brother for all their love and support over all the years. Finally, to Julie, thanks for being there and listening to me moan and groan my way through the last 18 months and helping me keep things in focus. You kept me going when I really needed it. Thanks. You're the best.

Chapter 1

Introduction

The study of particle physics has a distinguished history. From its origins in probing the structure of matter, it has progressed to the use of large particle accelerators such as the Large Electron Positron (LEP) collider at CERN to conduct experiments. Throughout this history, the experiments have examined structure at ever smaller scales.

The atom is made up of a nucleus of protons and neutrons that is surrounded by a cloud of electrons. The protons and neutrons are, in turn, made up of quarks. In the most widely accepted theoretical explanation of particle physics, the Standard Model, there are six quarks. These quarks interact by the exchange of gluons. The theory of these interactions is called Quantum Chromodynamics, or QCD.

The small scale of the system under consideration means that large energies are required to probe these quarks. At LEP there are four experiments which are located on a twenty-seven kilometre circumference ring. Electrons and positrons are accelerated around LEP until they are brought into collisions at the desired energy. The measurements described in this thesis are from hadronic events resulting from these collisions seen at OPAL, one of the four LEP experiments. QCD is studied and tested at a range of energies, reflecting the programme of work at LEPI and

LEPII.

This thesis describes two analyses of hadronic Z^0 decays selected from the OPAL data at LEPI and LEPII. In these events, a Z^0 is formed after the electron and positron are annihilated and this decays via the production of two primary quarks, which then produce hadrons. In the first analysis, hadronic Z^0 decays at a centre of mass energy $\sqrt{s} \approx M_{Z^0}$ were selected from the OPAL LEPI data. Events were studied in which 3 jets had been reconstructed using a CONE jet algorithm. A typical example of a 3-jet event may be seen in Figure 1.1. Two of these jets were initiated by the primary quarks from the hadronic Z^0 decay and the third was initiated by gluon bremsstrahlung. In events where the 3 jets have a symmetry such that the 2 lowest energy jets are of approximately equal energy, it is possible to study the charged particle content of gluon and quark jets of the same energy. Gluon jets are expected to be wider than quark jets of the same energy, have a higher charged particle multiplicity and a softer charged particle momentum spectrum.

Gluon jets were selected using an anti-tag based on their energy profile. This gluon jet enhanced sample was compared with the inclusive lower energy jet sample. An extended maximum likelihood fit to momentum and $\mathrm{d}E/\mathrm{d}x$ measurements was used to measure the momentum spectra for $\pi^{\pm}$, $K^{\pm}$ and $p(\overline{p})$ in each sample. A process of algebraic decomposition was then used to give the momentum spectra of these species in pure gluon and quark jets. The integral of each of these spectra yields the average multiplicity of each species in gluon and quark jets. The results of the JETSET Monte Carlo simulation were then compared to the data.

In the second analysis, hadronic events were selected from the OPAL LEPII data at $\sqrt{s} = 161$, 172 and 183 GeV and charged particle momentum spectra were investigated to determine the charged multiplicity. The peak of the $\xi_p = \ln(1/x_p)$ distribution was found and the predictions of Monte Carlo simulations were compared to the data. This analysis was performed with the support of the OPAL QCD working group.

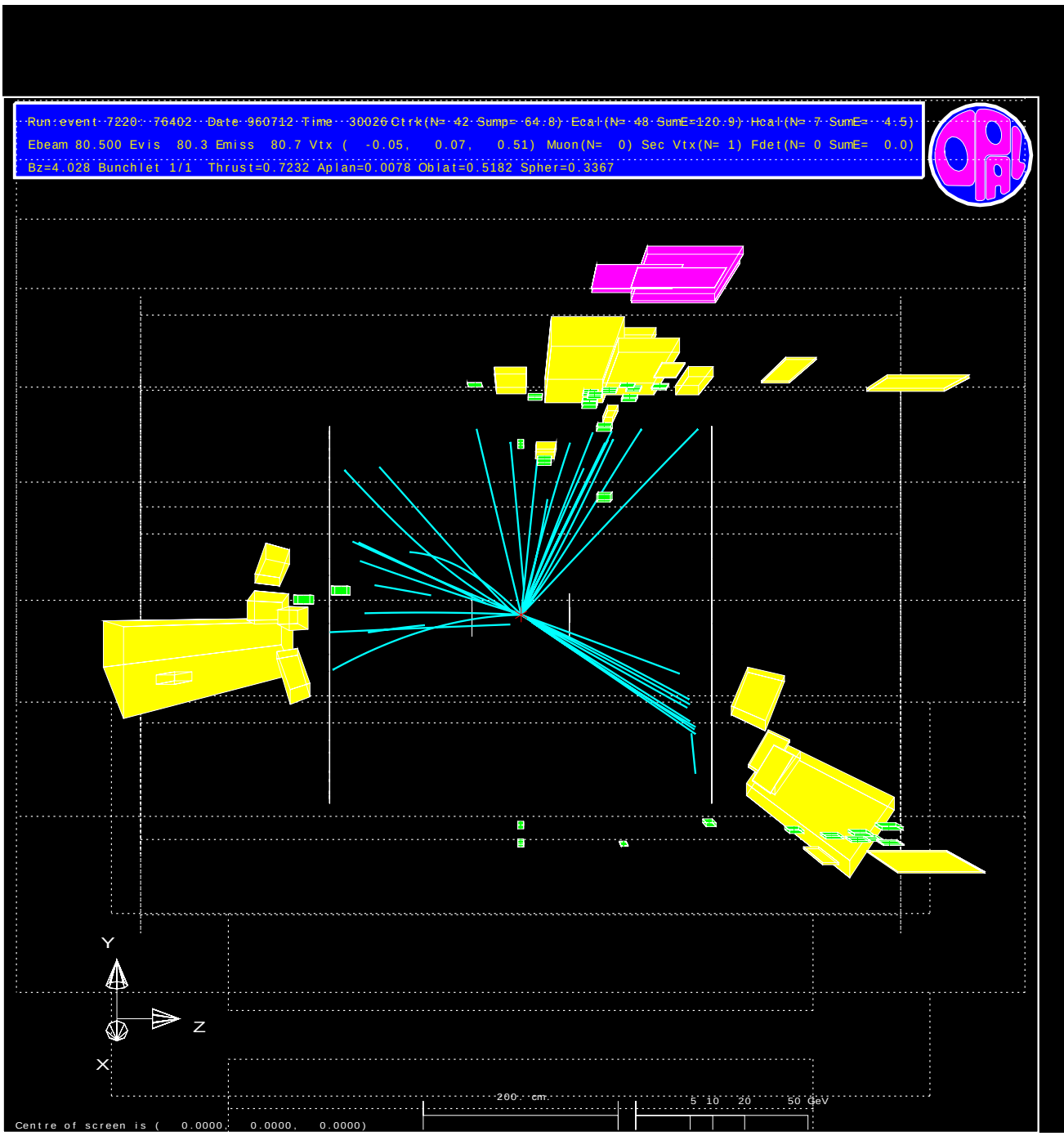

Figure 1.1: An example of a quark-anti-quark pair radiating a gluon, forming 3 hadronic jets in the OPAL detector at a centre of mass energy of 161 GeV.

The structure of this thesis is as follows: first, the OPAL detector is described in Chapter 2, then a theoretical outline of the Standard Model and QCD is given in Chapter 3. The identification of charged particles through the use of $\mathrm{d}E/\mathrm{d}x$ and the application of this technique to measure particle rates in gluon and quark jets at LEPI is the subject of Chapter 4. Charged particle momentum spectra at LEPII energies are discussed in Chapter 5.

Chapter 2

The OPAL Detector

The OPAL detector is one of four detectors situated on the LEP accelerator ring [1] at CERN which are used for the study of e^+e^- collisions. The LEP accelerator delivers e^- and e^+ beams of equal energies, which are brought into collision at the centre of each of the four LEP detectors. The resulting e^+e^- collisions provide a clean environment in which precision tests of electroweak theory and QCD can be performed. In the LEPI program, the accelerator operated at a centre of mass energy $\sqrt{s} \approx M_{Z^0}$. For LEPII, higher centre of mass energies were used. The OPAL detector was designed to reconstruct efficiently and identify the products of e^+e^- events over nearly the full solid angle. In hadronic Z^0 decays, the hadrons are observed as jets of particles in the detector. The reconstruction of the direction of the tracks which form these jets and the measurement of their momentum and energy using the tracking detectors and the electromagnetic calorimeter are important for the analyses described here. The detector was modified in 1995 in preparation for the LEPII program, so slightly different descriptions apply for the two analyses.

2.1 The OPAL detector

The OPAL detector [2] is a cylindrical system of subdetectors arranged around the LEP beampipe. Additional subdetectors form the end-caps of the detector. At the centre of OPAL lies a series of tracking detectors. These are surrounded by the calorimetry systems and the outer muon chambers. A schematic diagram is shown in Figure 2.1. The OPAL co-ordinate system is a right-handed co-ordinate system, defined with the origin at the interaction point, with the x axis pointing towards the centre of the LEP ring and the z axis pointing in the direction of the electron beam. Cylindrical co-ordinates are also defined: the polar angle θ and the azimuthal angle ϕ are defined with respect to the z- and x-axes, respectively, while r is the distance from the z-axis.

2.1.1 The central tracking system

The central tracking system consists of a series of detectors which measure the direction and momenta of charged tracks. This enables the reconstruction of the primary vertices of tracks. The tracking system lies within a solenoid of uniform axial magnetic field 0.435 T. The silicon microvertex detector [3] lies closest to the beam pipe and consists of two barrels, of radii 6 cm and 7.5 cm, of overlapping ladders of single-sided silicon microstrips covering the polar angle region $|\cos\theta| < 0.83$. In 1991, only $r-\phi$ readout was available, with 11 ladders in the inner barrel and 14 in the outer. The impact parameter of tracks at the point of closest approach to the origin, $|d_0|$, was measured with a resolution ≈ 18 μm. In 1993, the coverage was extended by additional $r-z$ microstrips. The $|d_0|$ resolution was improved to 17 μm and a resolution of 21 μm was achieved on the z co-ordinate at the point of closest approach, $|z_0|$. For LEPII, further ladders were inserted and the configuration was altered to improve the coverage in ϕ by allowing ladders to overlap, and the detector was extended along the z axis. Good vertex resolution is especially important for

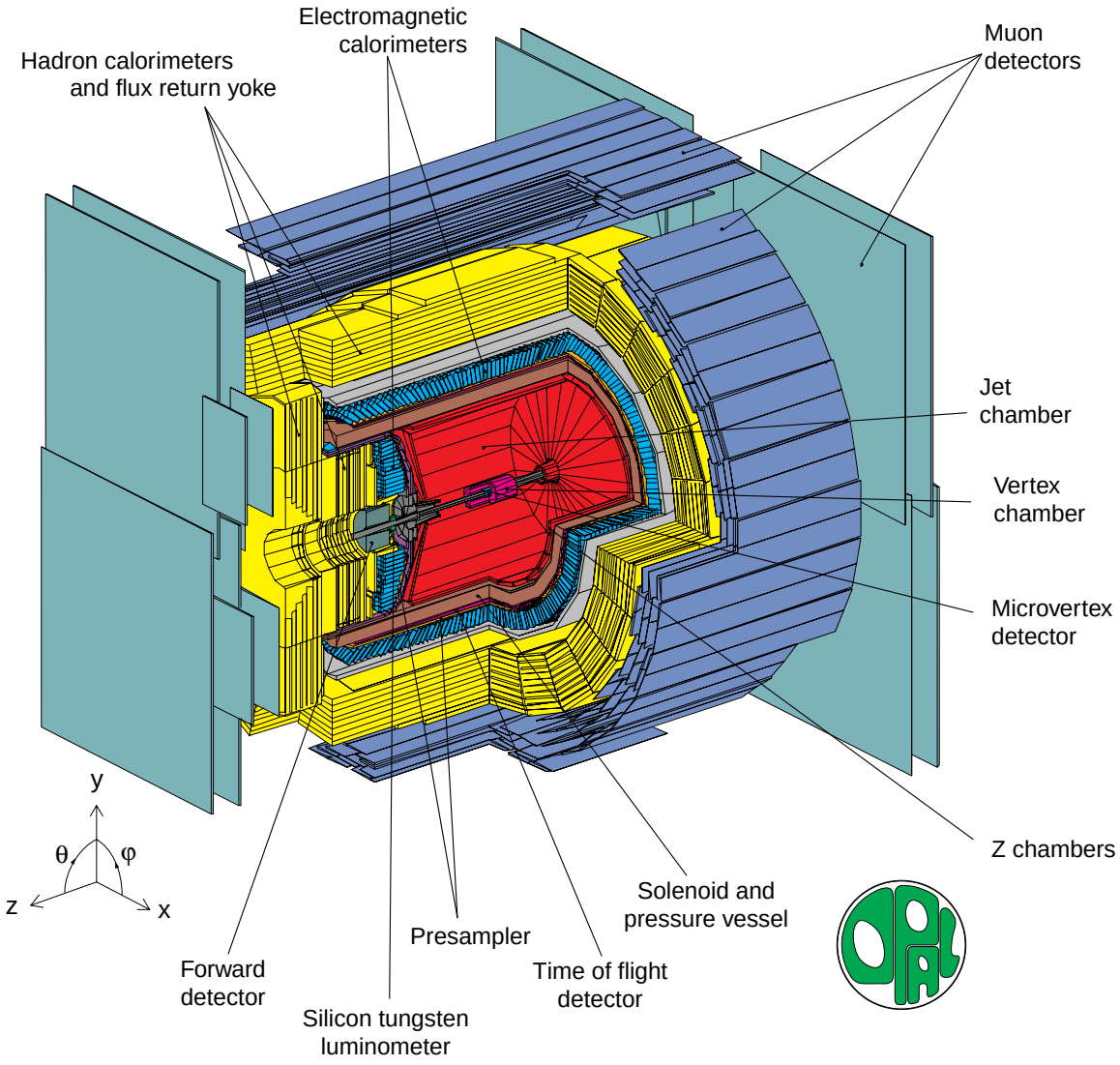

Figure 2.1: A schematic representation of the OPAL detector and its components.

heavy flavour physics.

A series of drift chambers complete the central tracking system. The inner layer of the central vertex detector [4], at a radius of 17.6 cm, contains axial sector sense wires, whilst the outer stereo sector, at a radius of 23.5 cm, contains wires inclined at an angle of approximately 4° to the axial wires. The drift time to the axial wires allows the $r - \phi$ position to be calculated with a resolution ≈ 55 μm and the combination of axial and stereo cell information provides a precise z co-ordinate

measurement for charged particles with a resolution of 700 μm. The axial wires cover $|\cos\theta| < 0.95$, whilst the axial and stereo combined cover $|\cos\theta| < 0.92$. This enables OPAL to locate the decay vertices of short-lived particles and to improve the track momentum resolution.

The central jet chamber [5,6] is a 4 m long cylinder of inner radius 25 cm and outer radius 185 cm, consisting of 24 sectors containing sense wires parallel to the beam direction. It is designed to measure the spatial position of tracks and the energy loss of particles by multiple sampling of the ionisation along a track. The drift time and the radial position of wire on which the signal is measured determine the co-ordinates in the $r-\phi$ plane, whilst a charge division technique provides the z position. The central jet chamber assists in particle identification by measuring the specific energy loss, $\mathrm{d}E/\mathrm{d}x$, along the track by summing the charge at each end of a wire. The radius of curvature of the track in the magnetic field gives momentum information.

The detector is normally operated to optimise the $\mathrm{d}E/\mathrm{d}x$ separation of particle species. A high gas pressure results in multiple scattering which adversely affects the momentum resolution, whilst a low pressure limits spatial resolution through diffusion effects. The gas gain is approximately 10^4 [5]. The drift field is 890 V/cm and the Lorentz angle by which the drift paths are deflected due to the magnetic field is 20.0°. Drift times are typically less than 5 μs.

Each sector of the jet chamber contains 159 sense wires bounded by 2 planes of cathode wires. The gas employed in the chamber is a combination of argon (88.2%), methane (9.8%) and isobutane (2.0%) at a pressure of 4 bar. The drift distance for electrons varies with the radius of the chamber, from 3 to 25 cm. The sense wires are equally spaced at 10 mm intervals and lie between radii of 255 mm and 1835 mm. They are alternately staggered by ± 100 μm to the left and right of the plane defined by the cathode wires to resolve left-right ambiguities. The voltage at the cathode wires determines the gas gain, and is typically -2.38 kV. Seventy three

percent of the solid angle is covered with 159 sense wires and 95% of 4π is covered by at least 8 wires.

The spatial resolution in the $r-\phi$ plane is 130 μm. In the $r-z$ plane, a spatial resolution of 6 cm is achieved for tracks in hadronic Z^0 decays. The momentum, p_{xy}, of a track in the x-y plane is measured with a precision parameterised by $\sigma_p/p_{xy} = \sqrt{(0.02)^2 + (0.0015 \cdot p_{xy}[\mathrm{GeV}/c])^2}$. Single tracks are found with a 97.9% efficiency for momenta $p > 1$ GeV/c.

The z chambers [7] are designed to make precise measurements of the z co-ordinates of charged particles. They cover 94% of the azimuthal angle and the polar angle range $|\cos\theta| < 0.72$ and have a resolution of 300 μm for the z co-ordinate. The z chambers consist of 24 drift chambers, divided into 8 cells in z. The chambers use the same gas as the jet chamber and operate with a drift field of 800 V/cm. Each cell has 6 anode wires at increasing radii with a 4 mm spacing and a stagger of ± 250 μm to resolve left-right ambiguities. The ϕ co-ordinate is determined by a charge division technique.

2.1.2 The dE/dx measurement at OPAL

The OPAL central jet chamber is designed to measure the momentum and specific energy loss of charged particles. At OPAL, a specific energy loss resolution $\sigma(\mathrm{d}E/\mathrm{d}x)/\mathrm{d}E/\mathrm{d}x = 2.8\%$ has been achieved [6]. This leads to a separation of at least 2σ up to momenta of 13 GeV/c for electrons and pions and up to 20 GeV/c for pions and kaons. For kaons and protons, separation of up to 1.5σ is possible in the momentum range $6 < p < 30$ GeV/c [6].

The measurement of the specific energy loss requires stability of the gas density, ρ, the drift field, E_d, the readout electronics pedestals (flash analogue-to-digital convertors are used) and the electronics gain. To achieve a gas gain G stable to within 1%, we require $\Delta\rho/\rho \approx 0.2\%$, $\Delta E_d < 1.2$ V/cm and the pedestals and the

electronics gain must be known to within 1%.

Certain quality cuts are applied to the raw energy loss measurement before calculating the mean energy loss of a track [5]. Only 'hits' (signals in the detector) assigned to the track in the final fit in the $r-\phi$ plane are used in the determination of the mean. The hits should be well separated, with no second hit within ± 200 ns. If parts of 2 tracks are within the double hit resolution of ~ 3 mm, the individual hits are not resolved and only a single hit is found. These hits are discarded. The hits should be at least 2 mm from a sense wire and if a track crosses a sector boundary then hits within 1 cm of the boundary are discarded. On average, $\sim 35\%$ of the hits for tracks in multihadronic events are rejected by these cuts.

Corrections derived from data for 45 GeV/c muons and minimum ionising pions ($p = 400-800$ MeV/c) are used to account for saturation, multiple hits, track length and cross talk [5]. Saturation occurs when the electric field near the sense wire is screened by the ions produced by the first electrons to reach the wire. This screening depends on the inclination of the track to the wire and an empirical correction is applied to the measured charge to account for this. To correct for multiple hits, the charge deposited by any subsequent hit is corrected for the tail of the preceding pulse using a reference pulse shape. The measured charges are approximately proportional to the track length and are normalised to a 1 cm gas sample thickness according to the track direction. Finally, cross talk occurs when signals are induced on neighbouring wires. A passive resistor network is used to compensate for this.

Following the quality cuts which are applied to the raw data, the independent energy loss measurements are used to calculate the specific energy loss. A maximum likelihood fit of the measured distribution with a Landau distribution is the most precise way to extract the energy loss information; the method of a truncated mean [8] used here is almost as accurate and uses less computer time. The top 30% of the measured $\mathrm{d}E/\mathrm{d}x$ values are rejected, which optimises the resolution [5]. This

results in a dependence on the number of samples used, N:

$$\frac{\sigma(\mathrm{d}E/\mathrm{d}x)}{\mathrm{d}E/\mathrm{d}x} \propto N^{-0.43} \tag{2.1}$$

Here, the exponent is not exactly -0.5, indicating the slightly non-Gaussian behaviour. The value of the truncated mean gives the mean differential energy loss, $\langle \mathrm{d}E/\mathrm{d}x \rangle$.

For the operation of the chamber, particle separation is more important than the resolution itself. The particle separating power for two particles A and B is defined as [6]:

$$D = \frac{|(\mathrm{d}E/\mathrm{d}x)_A - (\mathrm{d}E/\mathrm{d}x)_B|}{\sqrt{\sigma(\mathrm{d}E/\mathrm{d}x)_A^{\,2} + \sigma(\mathrm{d}E/\mathrm{d}x)_B^{\,2}}} \tag{2.2}$$

2.1.3 The Bethe-Bloch formula

The expected value of $\mathrm{d}E/\mathrm{d}x$ for a given momentum depends on the particle species. To determine the most likely particle hypothesis, a parameterisation of the energy loss formula is required over the entire momentum range up to 45 GeV/c. The OPAL experiment uses the Sternheimer-Peierls parameterisation of the Bethe-Bloch formula [9].

In the jet chamber, the energy loss occurs due to collisions with the chamber gas molecules which result in a Landau distribution of measurements with a long tail due to the production of δ-electrons in hard collisions. The typical mean energy loss observed in this experiment is smaller than the limit where one can treat the bound electrons as free particles (typically at energy transfers, η, of 10-100 keV/cm), so the Bethe-Bloch formula is valid. The mean differential energy loss as a function of particle velocity β and charge Q is [5]:

$$\langle \mathrm{d}E/\mathrm{d}x \rangle = \xi \frac{Q^2}{\beta^2} \left\{ \ln\left(\frac{2m_e c^2 \eta}{I^2}\right) + \ln \beta^2\gamma^2 - \beta^2 - \delta(\beta) \right\} \tag{2.3}$$

where $\gamma^2 = (1-\beta^2)^{-1}$ and $\xi = \nu.(2\pi n_e e^4/m_e c^2)$.

Here n_e is the electron density of the gas, m_e is the electron mass, I is the mean ionisation potential of the gas and ν is the fraction of electrons able to interact with the particle. The density function $\delta(\beta)$ takes into account the polarisation effect in the gas. This describes the behaviour of all particle species, but the energy loss formulae separate as a function of particle momentum for different species as shown in Figure 2.2.

The energy loss depends on the charge squared, Q^2, and the particle velocity, β. As β increases, the mean falls as $1/\beta$, reaches a minimum, then rises logarithmically (the region of relativistic rise) until it saturates at the Fermi plateau. The $\delta(\beta)$ contains the influence of the density and it is this that is described by the Sternheimer-Peierls parameterisation of [5]:

- $\delta = 0$ for $X < X_0$
- $\delta = b(X - X_A) + a(X_1 - X)^m$ for $X_0 < X \leq X_1$
- $\delta = b(X - X_A)$ for $X_1 < X$

where $X = \log(\beta\gamma)$, $m = 3$ and $b = 2\ln 10$. The values of the remaining free parameters are determined by a fit to data.

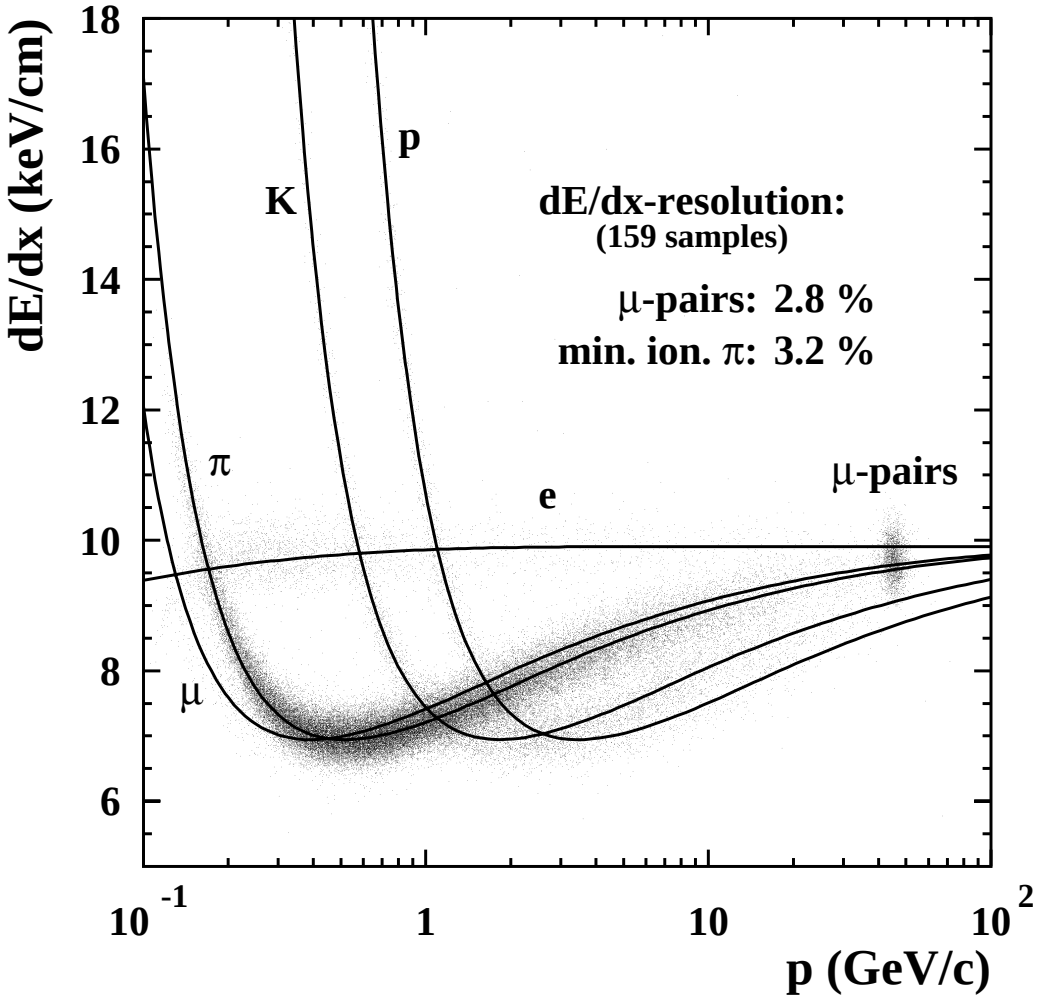

Figure 2.2: The measured energy loss $\mathrm{d}E/\mathrm{d}x$ for tracks from multihadronic events and for muon-pairs, together with the expected functional form. Tracks were required to be within $|\cos\theta| < 0.7$ and have at least 130 $\mathrm{d}E/\mathrm{d}x$ hits.

2.1.4 The electromagnetic calorimeter

The magnet coil is surrounded by a lead glass electromagnetic calorimeter [10], split into a barrel and two endcaps, which covers 98% of the solid angle. This system is designed to identify electrons and photons. These particles produce clusters of energy which help determine event shape variables, such as the thrust axis of the event. Presamplers are installed in front of the lead glass to measure the position and energy of showers beginning in the solenoid or pressure vessel in front of the electromagnetic calorimeter. In front of this is the time-of-flight system. In the barrel region, this consists of 160 scintillators that act as a cosmic ray veto. The time resolution is $\approx$ 300 ps. In 1996, an additional scintillator detector was added in the endcap in the forward region to enhance trigger information [11]. The time resolution of this subdetector is 3 ns.

The presampler barrel consists of 16 chambers of radius 239 cm and length 662 cm, covering $|\cos\theta| < 0.81$. Each chamber consists of two layers of drift tubes operating in the limited streamer mode which provide a strip readout [12]. Together with a measurement of the charge at each end of the wires, this gives the spatial position. The energy deposited is proportional to the hit multiplicity. In the end cap [13], a multi-wire proportional chamber is used. The barrel lead glass calorimeter is a cylindrical array of 9440 lead glass blocks at a radius of 246 cm, covering the polar angle range $|\cos\theta| < 0.81$. Each block corresponds to 24.6 radiation lengths and subtends an angle of approximately 40×40 mrad^2 at the origin. Cerenkov light is detected by phototubes at the base of each block. The energy resolution of the system is $\sigma_E/E = 0.2\% + 6.3\%/\sqrt{E}$. In the end cap, lead glass blocks of 22 radiation lengths are used for the region $0.81 < |\cos\theta| < 0.98$. These blocks are read out by vacuum photo triodes which can operate in the magnetic field. The resolution of the end cap is $\sigma_E/E = 5\%/\sqrt{E}$ at low energy.

2.1.5 The hadron calorimeter and muon chambers

The hadron calorimeter [14] consists of chambers separated by layers of the iron magnet return yoke and covers 97% of 4π with 4 nuclear interaction lengths. The barrel and endcap regions consist of limited streamer tube devices strung with anode wires with a gas mixture of isobutane and argon (75%:25%). Induced charges on the pads and strips on the surfaces of the chambers provide the signal. The sum of these analogue signals provides the hadron shower energy. The chambers also give muon tracking information. These are supplemented by the multi-wire proportional chambers of the hadron pole-tip calorimeter, which extend the range of the calorimetry from $|\cos\theta| = 0.91$ to 0.99. The energy resolution is $\sigma_E/E = 120\%/\sqrt{E}$.

The outermost detectors are the muon barrel [15] and endcap [16]. The endcap consists of four layers of limited streamer tubes in the plane perpendicular to the beam line, covering $0.67 < |\cos\theta| < 0.985$ with a spatial resolution of 0.3 cm. The barrel consists of 220 drift chambers covering $|\cos\theta| < 0.72$. For the barrel region, the drift time onto the anode wire provides the position in the $x - y$ plane to an accuracy of better than 0.15 cm. The z co-ordinate is found by using induced signals on two sets of cathode pads whose diamond shape repeats every 17.1 cm and 171 cm respectively. This results in a z co-ordinate accurate to 0.2 cm. The hadron calorimeter and muon chamber information is not used in the analyses described in this thesis but their details are included for completeness.

2.1.6 Luminosity measurement

The luminosity delivered to OPAL is determined by the rate of low angle Bhabha ($e^+e^- \rightarrow e^+e^-$) events [17], which provides a normalization for measured reaction rates. These Bhabha events are detected in the forward detector [18] and the silicon tungsten detector [19]. The forward detector is situated between 47 and 120 mrad from the interaction point, outside the beam pipe. It consists of a calorimeter,

proportional tube chambers to give the position of shower centroids, a ring of lead scintillator known as the gamma catcher and the far forward monitor, a system of small lead-scintillator calorimeters that detect electrons scattered outward by the LEP quadropoles. The silicon tungsten detector is a sampling calorimeter with an angular acceptance of 25 to 59 mrad, which consists of a layer of silicon to detect pre-showering, followed by layers of tungsten and silicon.

2.2 The trigger and event reconstruction

The OPAL trigger system [20] is used to control which physics events are recorded by the data acquisition system. The trigger must reject cosmic rays and signals due to beam-gas or beam-wall events and reduce the 45 kHz beam crossing rate to about the 5 Hz physics event rate limit of the data acquisition system. The trigger must also have an efficiency of close to 100% for physics events.

Events have to pass a series of trigger and, for data from 1993 onwards, pre-trigger [21] conditions. The trigger logic examines signals from subdetectors in a $\theta - \phi$ matrix to select good physics events in about 15 μs. The track trigger (which combines information from the components of the central tracking system), the time-of-flight trigger and the electromagnetic calorimeter trigger are important for selecting multihadronic events. Other trigger inputs come from the muon chambers, the hadron calorimeter and the forward detectors. The pre-trigger was introduced to deal with the shorter time between beam crossings which was introduced when LEP operated in 8 on 8 bunch train mode rather then 4 on 4. The pre-trigger operates on 'stand-alone' conditions, such as multiplicity counts and energy sums. The pre-trigger decision time is about 5 μs.

Events which have been selected by the trigger are read out from each subdetector and are assembled by the event builder in a VME crate. These events are then passed

to the filter software [22] which checks the events and analyses them using more data than the trigger to decide whether they are useful physics events. The filter also monitors the events, producing online histograms, before compressing the events and recording them on to disk. The filter rejects some 15-35% of events.

The ROPE [23](Reconstruction of OPAL Events) farm is a collection of work stations which reconstruct the events. ROPE carries out pattern recognition on the digitised data using calibration constants and detector geometry information to identify particle tracks or energy clusters. ROPE enables data to be reprocessed if the calibration constants change and provides the framework for analyses of the OPAL data. A permanent record of the data is made on an optical disk and the reconstructed events are copied to the SHIFT computer at CERN for permanent disk storage and off-line analysis. ROPE also processes Monte Carlo simulations of physics events.

The GOPAL [24] simulation of the OPAL detector is based on the GEANT3 package [25]. GOPAL contains a geometrical description of the OPAL detector in the form of a series of volumes specifying the materials and tracking parameters of the detector. From a given set of particle 4-vectors generated by a Monte Carlo program, GOPAL tracks the particles through the detector, noting any scattering, showering, decays or other interactions that may occur and provides the detector response to 'hits' to simulate the data which the detector would have produced. The output of the Monte Carlo programs with detector simulation is in the same form as the data. This information is used to correct the data for acceptances and detector effects.

2.3 Data and Monte Carlo samples

The analyses described in this thesis are conducted on samples of hadronic Z^0 decays (multihadronic events). The OPAL multihadronic event selection criteria are detailed in [26] and [27]. A brief summary follows.

2.3.1 Multihadronic event selection criteria

The selection of multihadronic events is based on the properties of the tracks and clusters of energy within the detector. Energy clusters in the electromagnetic calorimeter are groups of neighbouring lead glass blocks which register significant energy deposition in an event. Good clusters in the electromagnetic calorimeter were defined as having a raw energy $E_{\rm raw} \geq 100$ MeV in the barrel region of the detector, or 200 MeV for the endcaps. In addition, clusters must be spread over at least 2 good blocks in the endcap. There is no minimum number of blocks required in the barrel. At least 7 good clusters were required for the event to be selected.

Tracks are reconstructed from hits in the central detector. Tracks were considered as good tracks if they had at least 20 hits in the central detector, and impact parameters $|d_0| < 2.0$ cm in the $x-y$ plane and $|z_0| < 40.0$ cm in the z direction relative to the beam spot position. The first hit recorded must have been within 60.0 cm of the beam spot. The transverse momentum of the track in the $x-y$ plane was required to satisfy $p_{xy} \geq 50$ MeV/c. The track must have been well contained within the detector, lying within the polar angle range $|\cos\theta| \leq 0.995$. The tracks were required to have a $\chi^2_{r-\phi} < 999$ for the track fit in the $r-\phi$ plane and $\chi^2_{s-z} < 999$ for the track fit in $s-z$, where $s-z$ is the $r-\phi$ path integral. Five or more good tracks were required.

The energy deposition in the electromagnetic calorimeter was required to satisfy the following: $R_{\rm vis} \geq 0.10$ and $|R_{\rm bal}| \leq 0.65$ where $R_{\rm vis} = E_{\rm shw}/2.E_{\rm beam}$ and $R_{\rm bal} =$

$E_{\rm bal}/E_{\rm shw}$, where the shower energy, $E_{\rm shw}$, is the sum of the raw energy of the good clusters in the electromagnetic calorimeter and $E_{\rm bal}$ is the sum over the projection of the energies, $E_{\rm raw}\cos\theta$.

These selection criteria are 98.4% efficient for multihadronic events [26]. The $R_{\rm vis}$ cut rejects two-photon ($\gamma\gamma \rightarrow q\bar{q}$) events and the requirement of 5 good tracks and 7 clusters removes events with lepton-pair final states. The remaining backgrounds are $e^+e^- \rightarrow \tau^+\tau^-$ events (0.11 %) and $\gamma\gamma \rightarrow q\bar{q}$ events (0.07 %) [26].

2.3.2 LEPI data

The LEPI data consists of the entire OPAL hadronic Z^0 event dataset of 4.4 million events, from years 1990-1995, collected at $\sqrt{s} \approx M_{Z^0}$. The majority of the data was collected at $\sqrt{s} = M_{Z^0}$, but some was collected at $M_{Z^0} \pm 2$ GeV and some at $M_{Z^0} \pm 1$ GeV. The Monte Carlo sample consisted of 6.6 million hadronic Z^0 events, generated at $\sqrt{s} = M_{Z^0}$ using the JETSET 7.408 Monte Carlo [28]. Some of the variable parameters in the JETSET program were changed from their default values by the OPAL collaboration (details of the event shape tuning are given in [29] and the tune to particle rates is discussed in [30]). This version of JETSET is referred to as the 'OPAL-tuned' JETSET Monte Carlo. The Monte Carlo exists at the 'generator level' (this does not include initial state radiation or detector simulation and allows all charged and neutral particles with lifetimes less than 3.10^{-10} s to decay) and 'detector level', where the generated events have been passed through a full simulation of the OPAL detector and event reconstruction and were required to satisfy the same event selection criteria as the data. The 4-vectors of the particles at the end of the JETSET parton shower are referred to as the 'parton level'.

2.3.3 LEPII data

The data in the LEPII analysis consists of three samples at different centre of mass energies. The first sample corresponds to an integrated luminosity of $\mathcal{L} = 10.00 \pm 0.04 \pm 0.04$ pb^{-1} at a centre of mass energy $\sqrt{s} = 161.3$ GeV [31], the second to a luminosity of $\mathcal{L} = 10.42 \pm 0.06$ pb^{-1}, collected at a mean energy of 172.1 GeV [32] and the third to an integrated luminosity of $\mathcal{L} = 55.22 \pm 0.02$ pb^{-1}, recorded at a centre of mass energy of 182.6 GeV [33].

The PYTHIA 5.722 [28], HERWIG 5.8d [34], ARIADNE 4.08 [35] and COJETS 6.23 [36] Monte Carlo generators provided the multihadronic event Monte Carlo samples and were used to test different hadronisation models. These different models are discussed in more detail in Section 3.3. The grc4f 1.2 [37] and EXCALIBUR [38] Monte Carlos were used for four-fermion background simulation. This background consists of events of the type $e^+e^- \rightarrow (Z^0/\gamma)^* \rightarrow f\bar{f}f\bar{f}$ with quark or leptonic final states, produced by s channel or t channel processes (where possible), including W^+W^- events but excluding those processes with Feynman diagrams with intermediate gluons.

The grc4f Monte Carlo simulates four-fermion processes using matrix elements and allows for initial and final state radiation. JETSET is used for the parton shower and hadronisation of any final state quarks. The EXCALIBUR Monte Carlo simulates all four-fermion processes in e^+e^- collisions using matrix elements. EXCALIBUR includes $\mathcal{O}(\alpha^2)$ initial state radiation but, unlike grc4f, uses massless fermions. JETSET is used for hadronisation and to account for fermion masses.

Chapter 3

QCD and Hadronisation

The Standard Model [39] is the theoretical framework for modern particle physics. In the Standard Model, fermions are grouped into families and generations; in particular, there are six leptons and six quarks. The interactions between these particles are mediated by gauge bosons. In this chapter, the Standard Model is summarised, with particular emphasis on QCD, before hadronisation models are discussed. A more complete account of the Standard Model may be found in [40].

3.1 The electroweak sector of the Standard Model

Electroweak theory describes the interaction of charged particles and the weak interaction through the exchange of a massless photon, γ, and massive gauge bosons, Z^0, W^+ and W^-. Electroweak theory is a quantum field theory based on the group $SU(2) \otimes U(1)$. The Lagrangian is required to be invariant under any local and global gauge transformations of this group.

The fermions manifest themselves as a left handed SU(2) doublet and a right handed U(1) singlet as may be seen below for the first generation of leptons:

$$\psi_1(x) = \begin{pmatrix} e \\ \nu_e \end{pmatrix}_L , \ \psi_2(x) = e_R \tag{3.1}$$

and similarly for quarks:

$$\psi_1(x) = \begin{pmatrix} u \\ d' \end{pmatrix}_L , \ \psi_2(x) = u_R, \ \psi_3(x) = d'_R \tag{3.2}$$

where d' is the 'Cabbibo rotated' d-field. The eigenstates of the weak interaction are not the same as the quark mass eigenstates, with the mixing described by the Cabbibo-Kobayashi-Maskawa matrix:

$$\begin{pmatrix} d' \\ s' \\ b' \end{pmatrix} = \begin{pmatrix} V_{ud} & V_{us} & V_{ub} \\ V_{cd} & V_{cs} & V_{cb} \\ V_{td} & V_{ts} & V_{tb} \end{pmatrix} \begin{pmatrix} d \\ s \\ b \end{pmatrix} \tag{3.3}$$

The electroweak interaction between these fermions is described by vector fields; linear combinations of these fields make up the physical gauge bosons. The charged current interaction between fermions, mediated by the W^+ and W^- bosons, corresponds to the fields

$$W_\mu = (W^1_\mu + iW^2_\mu)/\sqrt{2}, \ W^\dagger_\mu = (W^1_\mu - iW^2_\mu)/\sqrt{2} \tag{3.4}$$

and the neutral current interaction, mediated by the Z^0 and γ, corresponds to the fields

$$Z_\mu = W^3_\mu \cos\theta_W - B_\mu \sin\theta_W , \ A_\mu = W^3_\mu \sin\theta_W + B_\mu \cos\theta_W \tag{3.5}$$

where θ_W is the weak mixing angle. The gauge bosons (and the fermions) gain their masses through the Higgs Mechanism, which breaks the symmetry of the Lagrangian.

3.2 Quantum Chromodynamics

Unlike Quantum Electrodynamics, QCD is a non-Abelian SU(3) gauge theory, based on the exchange of gluons between quarks. Quarks were first postulated to explain the observed baryon and meson spectra, with baryons as three-quark states and mesons as $q\overline{q}$ states. The introduction of colour followed the need to preserve the total anti-symmetry of the baryon wave function after the discovery of *sss* states. The charges of the colour field are red, green and blue, with observed hadrons being colourless (ie colour singlets), and quarks and the colour field quanta, gluons, carrying colour charge. The colourless nature of hadrons leads to the idea that quarks are confined. Quarks are also believed to exhibit asymptotic freedom due to the variation of the strong coupling constant α_s with the distance between two coloured partons. At small separations, α_s is small, and quarks act as free particles.

The interactions of quarks and gluons are described by the QCD Lagrangian, which contains a term corresponding to gluon field self-interactions. It is this term that gives rise to the non-Abelian nature of QCD. The coupling constant determines the strength of the interactions in QCD and may be written as

$$\alpha_s = g^2/4\pi \tag{3.6}$$

where $\alpha_s(Q^2)$ is the running coupling constant, dependent on the energy scale Q and g is the strong coupling constant.

For SU(3) QCD, the colour factors C_F and C_A associated with the colour charge carried by the quark and gluon are $C_F = \frac{4}{3}$ and $C_A = 3$ respectively. The colour factor associated with a gluon is just over twice as large as that associated with a quark, which implies that, in a parton shower, gluons tend to radiate more gluons than quarks do.

3.2.1 Fragmentation functions

Fragmentation functions may be defined in terms of the production cross-section, σ, of hadrons of type h from an e^+e^- collision at a centre of mass energy $\sqrt{s}$ and the total hadronic cross-section, $\sigma_{\rm had}$, as

$$F^h(x_p, s) = 1/\sigma_{\rm had}\ \mathrm{d}\sigma/\mathrm{d}x_p(e^+e^- \to hX) \tag{3.7}$$

where $x_p = 2p_h/\sqrt{s} \leq 1$ is the scaled hadron momentum. The scaled energy $x = 2E_h/\sqrt{s}$ is sometimes used instead. The integral of the fragmentation function yields the average multiplicity of the hadrons:

$$\langle n_{\rm ch} \rangle = \int_0^1 F^h(x_p, s)\mathrm{d}x_p \tag{3.8}$$

The fragmentation function may be represented as a sum of contributions from each of the primary partons, i = u,d,...,g:

$$F^h(x_p, s) = \sum_i \int_{x_p}^1 C_i(s; z, \alpha_s) D_i^h(x_p/z, s)\frac{\mathrm{d}z}{z} \tag{3.9}$$

where z is the momentum fraction carried by parton i, D_i^h is the fragmentation function for parton i fragmenting into hadron h and $C_i = g_i(s)\delta(1-z)$ for quarks where g_i is the appropriate electroweak coupling. The coefficient function for gluons, C_g, is zero in lowest order calculations. Due to the non-pertubative nature of hadronisation, the D_i^h cannot be calculated. However, the fragmentation of partons of type i into type j can be calculated, at an energy-squared scale t, using

$$D_i^j(x_p, t) = \sum_k \int_{x_p}^1 K_i^k(z, t, s) D_k^j(x_p/z, s)\mathrm{d}z \tag{3.10}$$

where the kernel function K_i^k is perturbatively calculable. Local Parton Hadron Duality [41] is then employed, allowing D_i^j to be replaced by D_i^h, and the equation is then applied to hadronic fragmentation functions.

The fragmentation functions change when the scale is increased from t to $t+\delta t$. Such a change is associated with the splitting of a parton in this scale interval. The fragmentation functions satisfy an evolution equation similar to that for parton distribution functions:

$$t\frac{\partial}{\partial t}\mathrm{D}_i(x_p,t) = \sum_j \int_{x_p}^1 \frac{\mathrm{d}z}{z}\frac{\alpha_s}{2\pi}P_{ji}(z,\alpha_s)D_j(x_p/z,t) \tag{3.11}$$

where P_{ji} is the Altarelli-Parisi splitting function [42] for the splitting of parton type i into j in the scale interval δt.

3.2.2 Evolution of the mean charged multiplicity in QCD

It can be shown [42] that the average charged particle multiplicity of hadrons can be written as

$$\langle n_{\mathrm{ch}}\rangle = \int_0^1 F^h(x_p,s)\mathrm{d}x_p \propto \exp\frac{1}{b}\sqrt{\frac{6}{\pi\alpha_s(s)}} \sim \exp\sqrt{\frac{6}{\pi b}\ln\left(s/\Lambda^2\right)} \tag{3.12}$$

where Λ is a scale parameter and $b = \frac{1}{12\pi}(33-2n_f)$ where n_f is the number of flavours. The strong coupling constant can be written as

$$\alpha_s(Q^2) = \frac{1}{b\ln\left(Q^2/\Lambda^2\right)} \tag{3.13}$$

which implies asymptotic freedom for $n_f < 17$.

The behaviour of the fragmentation function at small x_p may be examined by considering [42]

$$x_pF^h(x_p,s) \propto \exp\left(-\frac{1}{2\sigma^2}(\xi_p-\xi_0)^2\right) \tag{3.14}$$

which is a Gaussian function in the variable $\xi_p = \ln\left(1/x_p\right)$ whose peak position is

$$\xi_0 = \frac{1}{4b\alpha_s(s)} \simeq \frac{1}{4}\ln\left(\frac{s}{\Lambda^2}\right) \tag{3.15}$$

and whose width is

$$\sigma = \left(\frac{1}{24b}\sqrt{\frac{2\pi}{C_A\alpha_s^3(s)}}\right)^{1/2} \tag{3.16}$$

These analytical predictions for the energy dependence of the average charged particle multiplicity and the peak of the ξ_p distribution can be compared with experimental observations.

3.2.3 Gluon and quark jet differences

In multihadronic Z^0 events, the Z^0 decays to two primary quarks which then form hadrons ($e^+e^- \rightarrow Z^0 \rightarrow q\bar{q}$ events). The momenta of these quarks are equal and opposite in the laboratory frame, which is also the rest frame of the Z^0. These two primary quarks might be expected to form back-to-back jets of hadrons and this is often the case. However, events are also observed with 3 or more jets in the final state.

The 3-jet final states ($e^+e^- \rightarrow Z^0 \rightarrow q\bar{q}g$ events) arise when one of the primary quarks radiates a hard gluon (gluon bremsstrahlung) before hadronisation occurs. The Feynman diagram for this process is shown in Figure 3.1. A hard gluon, which is well-separated in phase-space from the quarks, develops into a separate jet of hadrons. In these 3-jet final states, where only one hard gluon has been emitted, it is usual to see one high energy jet and two lower energy jets. Experimentally, it has been observed that there are certain differences between jets which have been initiated by a hard gluon and jets arising from a quark of the same energy.

The average charged particle multiplicity in a given process can be calculated in QCD [43,44]. The resulting equations are valid to the next-to-leading logarithm and the average charged particle multiplicity of an e^+e^- event can be written as $\langle n_{\rm ch}\rangle_{e^\pm} = 2\langle n_{\rm ch}\rangle_q$ where $\langle n_{\rm ch}\rangle_q$ is the average charged particle multiplicity of a quark jet. This is consistent with the average charged particle multiplicity obtained

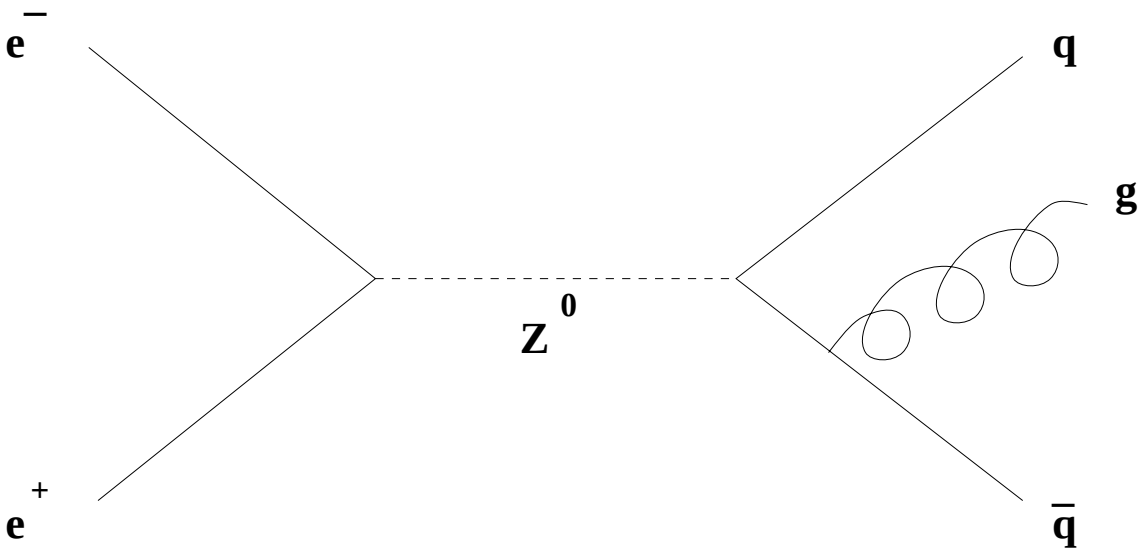

Figure 3.1: Feynman diagram for the process $e^+e^- \rightarrow Z^0 \rightarrow q\bar{q}g$.

above, and the asymptotic behaviour leads to a relation between the average charged particle multiplicity in a quark jet and the average charged particle multiplicity in a gluon jet at an energy-squared scale t:

$$\langle n_{\rm ch} \rangle_q(t) \sim \frac{C_F}{C_A} \langle n_{\rm ch} \rangle_g(t) \propto \frac{1}{b} \sqrt{\frac{2C_A}{\pi \alpha_s(t)}} \tag{3.17}$$

This suggests that the average multiplicity in a gluon jet should be 9/4 times that in a quark jet (asymptotically). This arises from the greater effective colour charge of the gluon, which is proportional to $\sqrt{C_A}$, as opposed to $\sqrt{C_F}$ for the quark. In addition, the fragmentation function of a gluon is expected to be softer than that of a quark jet and the height of the peak of the ξ_p distribution is expected to vary asymptotically in the ratio $C_F : C_A$ for quarks compared to gluons. A similar softness is expected in heavy quark fragmentation functions; in this case, however, it arises because of the soft nature of the heavy quark decay products.

Another characteristic difference is that gluon jets are expected to be broader

than quark jets of the same energy. This was originally an experimental observation, but it can be shown [42] from a consideration of the Sterman-Weinberg two jet fraction for e^+e^- annihilation, $f_2 = \sigma_2/\sigma_{\rm had}$, where σ_2 is the two-jet final state cross-section and $\sigma_{\rm had}$ is the total hadronic cross-section, that the angular width of a quark jet for a given small energy fraction ϵ is:

$$\delta_q \sim \exp\left(\frac{\pi(1-f_2)}{4C_F\alpha_s(s)\ln\epsilon}\right) \tag{3.18}$$

for a Sterman-Weinberg fraction f_2. As $1/\alpha_s(s)$ increases logarithmically with energy, quark jets become more collimated as the energy scale increases. The corresponding expression for a two gluon jet final state has a factor of C_A rather than C_F and so the decrease of the angular width of gluon jets is less marked than that of quark jets. In addition, for a fixed energy scale, the expected width of a gluon jet is larger than that of a quark jet. It should be noted that all the above applies asymptotically and the differences between gluon and quark jets at current energy scales are expected to be less marked than the asymptotic behaviour.

3.3 Hadronisation models

In the case of QCD, complete perturbative calculations have only been performed to a few orders in α_s; in most cases the calculations are to next-to-leading order. However, higher order terms may give large corrections and thus should not be ignored. Detailed simulations of the process of e^+e^- annihilation and the final state hadrons are required for physics analysis, which implies that finite order perturbative calculations will not provide an accurate description of the data. One solution to this problem is to evolve the primary partons using perturbative QCD, which aims to take account of important higher order terms, for momentum transfer scales $t > t_0$, where the infra-red cut-off $t_0 \approx 1$ GeV^2. A non-perturbative phenomenological

model of the subsequent hadronisation process is then used at scales below t_0 to describe the observed hadrons.

The parton shower approach is often used as the approximate perturbative treatment, since the probability of a given parton branching (radiating a gluon) can be calculated in QCD through the Altarelli-Parisi evolution equations. The Altarelli-Parisi, or DGLAP, evolution equations are similar to Equation 3.11. The calculation of the probability can then be employed in a Monte Carlo algorithm [28, 42]. The parton shower develops with each parton continuing branching, until partons are produced of a low enough virtual mass that the algorithm does not generate any more branching and the shower terminates. The progression of a parton shower is shown diagramatically in Figure 3.2. A hadronisation model is then used to convert the partons into physically observable hadrons, some of which may be unstable and are decayed according to decay tables.

An approach based on matrix elements, which relies on the currently available calculations to evolve the partons, may be used instead of the parton shower. Problems arise for certain observables when large logarithmic terms in these calculations do not completely cancel. Colour coherence effects can also be important: long wavelength quanta are sensitive to the presence of neighbouring charged partons. Dipoles then become the effective radiating unit [41], leading to a suppression of soft gluons between the neighbouring partons. This may produce effects at any stage in the evolution; in the parton shower this can be included by angular ordering so that successive branchings are nested [45] as in the modified leading log approximation (MLLA). This colour coherence limits soft particle production and leads to the 'hump-backed plateau' of the ξ_p distribution and slows the rise with $\sqrt{s}$ of both ξ_0 and $\langle n_{\rm ch} \rangle$ compared to incoherent (LLA and DLA) calculations.

One general approach to hadronisation is the hypothesis of local parton hadron duality [41], which states that the momentum transfer and flow of quantum numbers at parton level should be followed at the hadron level, so that the flavour of a quark

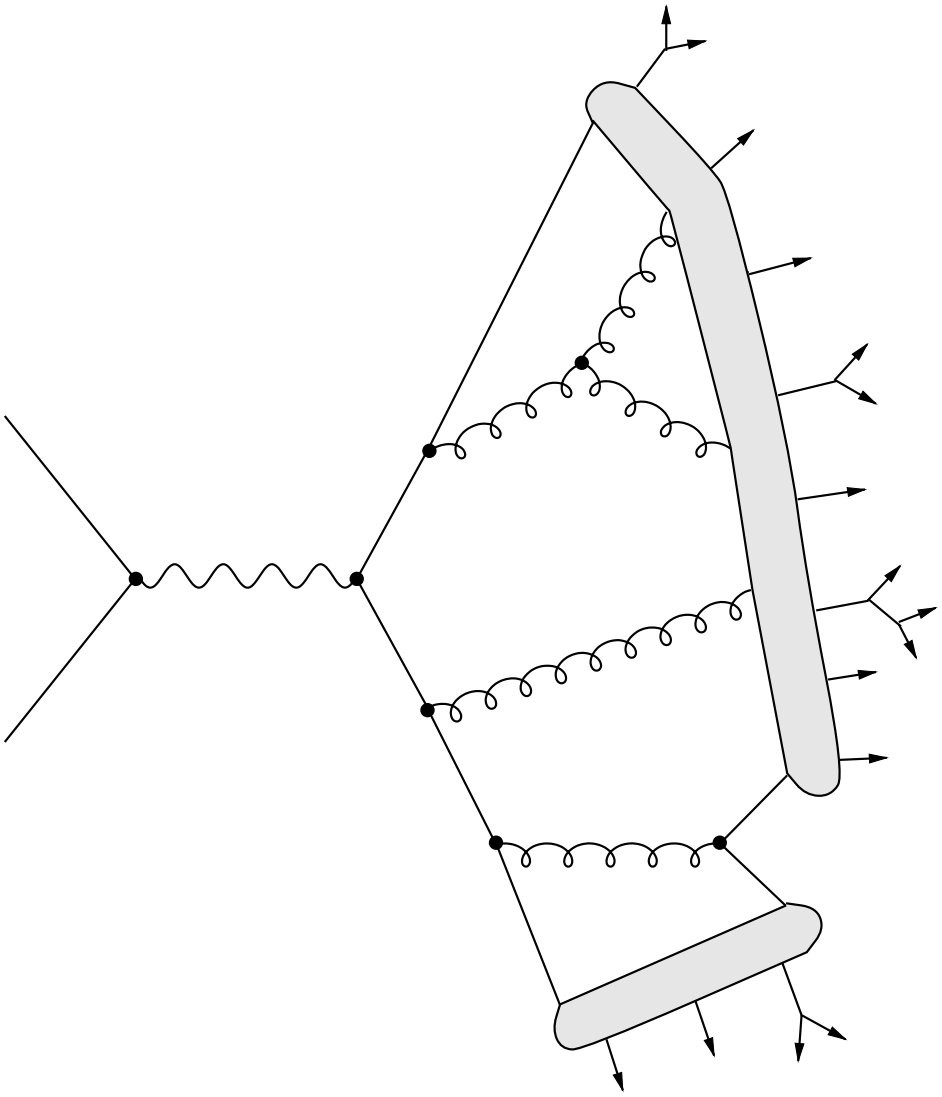

Figure 3.2: The parton shower process and string model hadronisation in e^+e^- annihilation (from [42]).

which initiates a jet should be found in a hadron near the jet axis. Over the years, several models have been developed. In all of these models the hadronisation process occurs locally in space-time. A summary is given below, but more details may be found in [46].

3.3.1 Independent fragmentation

The approach of Field and Feynman [47,48] remains the simplest one; each parton fragments independently. The fragmenting quark is combined with an anti-quark from a $q\overline{q}$ created from the vacuum to produce a meson with an energy fraction z. The other quark is fragmented in the same way and the process continues until the energy fraction falls below some cut-off. Gluons are first split into a $q\overline{q}$ pair, either assigning all of the gluon's momentum to one or other of the quarks with equal probability, so that the gluon acts as a quark of random flavour, or by using the Altarelli-Parisi splitting function for gluons. It is necessary to suppress the production of strange quarks ($u : d : s = 1 : 1 : 0.33$) and of diquarks ($q'q' : q \approx 1 : 9$).

This model relies on a small number of parameters to describe the fragmentation function, the transverse momentum distribution and the ratio of vector to pseudoscalar meson production. However, the fragmentation depends on the energy of the parton rather than its virtuality, leading to momentum conservation problems, and Lorentz invariance is difficult to implement. The final parton has to be removed from the jet at the end of fragmentation and colinear jets remain distinct rather than merging as expected. This model is implemented in the event generators ISAJET [49], COJETS [36], which uses a virtuality-ordered parton shower without colour coherence, and FIELDAJET [50].

3.3.2 The string model

In the string model [51,52], neglecting gluon bremsstrahlung, the quark and anti-quark from the Z^0 move apart in opposite directions; the colour field between them forms a string with uniform energy per unit length, $\kappa \approx 1$ GeV/fm, which corresponds to a linear quark confining potential. The string then fragments iteratively into hadrons through $q\overline{q}$ pair production. If gluons are present, then kinks are in-

troduced to the string. The transverse size of the string is small compared to its length, and the string is usually modelled as having no transverse excitations.

As the $q\overline{q}$ pair move apart, the potential energy of the string increases until the string breaks by the production of a $q'\overline{q}'$ pair, so that two colour singlet systems exist. If the invariant masses of these two string fragments are large enough, further breaks are possible. The slowest moving fragments are produced first, near the centre of the string. In the Lund string model [53], this continues until on-mass-shell hadrons are produced. The $q'\overline{q}'$ pairs are produced by quantum mechanical tunnelling and this leads to a flavour independent Gaussian distribution of the transverse momentum, $p_\perp$, of the $q'\overline{q}'$ pairs. The $p_\perp$ of these pairs is locally zero to ensure that the string does not have any tranverse excitations. This tunnelling also ensures that heavy quark and strange quark production is suppressed within the string. Heavy quarks in e^+e^- annihilation thus either come from perturbative gluon splitting or are the primary quarks from the Z^0.

In the classical picture, a $q'\overline{q}'$ pair with a mass or transverse momentum relative to the string is produced a certain distance apart, with the field energy between the quarks transforming into the transverse momentum. In quantum mechanics, they are produced at the same point (to conserve flavour locally) and then tunnel out. The tunnelling probability for a common transverse mass $m_\perp$ of the $q'\overline{q}'$ pair is [46]:

$$\exp\left(-\frac{\pi m_\perp^2}{\kappa}\right) = \exp\left(-\frac{\pi m^2}{\kappa}\right)\exp\left(-\frac{\pi p_\perp^2}{\kappa}\right) \tag{3.19}$$

where κ is the energy per unit length of the string. This leads to a Gaussian transverse momentum distribution for the $q'\overline{q}'$ pairs. It also implies a suppression of strange quark and heavy quark production in fragmentation in the ratio $u : d : s : c \approx 1 : 1 : 0.3 : 10^{-11}$.

Mesons are produced when a quark and an anti-quark from adjacent string breaks are combined. The string model uses an algorithm based on the number of spin states using (2J+1) spin counting factors to produce pseudoscalar and vector mesons. In

addition, the wavefunction of the quark produced in a string break must match onto the wavefunction of the meson. Baryons are produced through a tunnelling mechanism similar to that for $q'\overline{q}'$ production; the string can break either by $q'\overline{q}'$ production or by diquark ($q'q'$-$\overline{q}'\overline{q}'$) production. For diquark production, the tunnelling probability has to take into account the relative probabilty to pick out a $q'q'$ compared to a q, the extra suppression if a $q'q'$ contains a strange quark and the suppression of spin-1 diquarks relative to spin-0. The diquark then joins with a quark to form a baryon. An alternative is the popcorn mechanism, where $q'\overline{q}'$ pairs are produced one after the other. Schematic representations of the popcorn and diquark models are shown in Figure 3.3. In the popcorn model, if a $q'\overline{q}'$ pair is formed between another $q'\overline{q}'$ pair of the same colour, one would expect two colour singlet systems to arise. If the central pair is a different colour from the outer pair, then a net field can exist between the two systems. If an additional pair is now created in this central field, a baryon-anti-baryon system may be formed. There is also the possibility of forming baryon-meson-anti-baryon systems (other configurations are possible but the probability of forming them is small).

Fragmentation functions, $F(z)$, are used to select the energy and longitudinal momentum of the hadron, which takes a fraction z of the available energy and longitudinal momentum. The parton fragmentation functions and local parton hadron duality motivate the form of these fragmentation functions. The Lund string model uses the parameterisation of :

$$F(z) \propto z^{-1}(1-z)^a \exp(-bm_\perp^2/z) \tag{3.20}$$

which is known as the Lund symmetric fragmentation function, but others are available, such as the Peterson fragmentation function which is designed for the fragmentation of heavy quarks.

In the case of gluon bremsstrahlung, the situation is more complicated. As mentioned above, the gluon is modelled as a kink on the string, carrying energy and momentum. The $q\overline{q}g$ string will fragment in such a way that to a first approximation

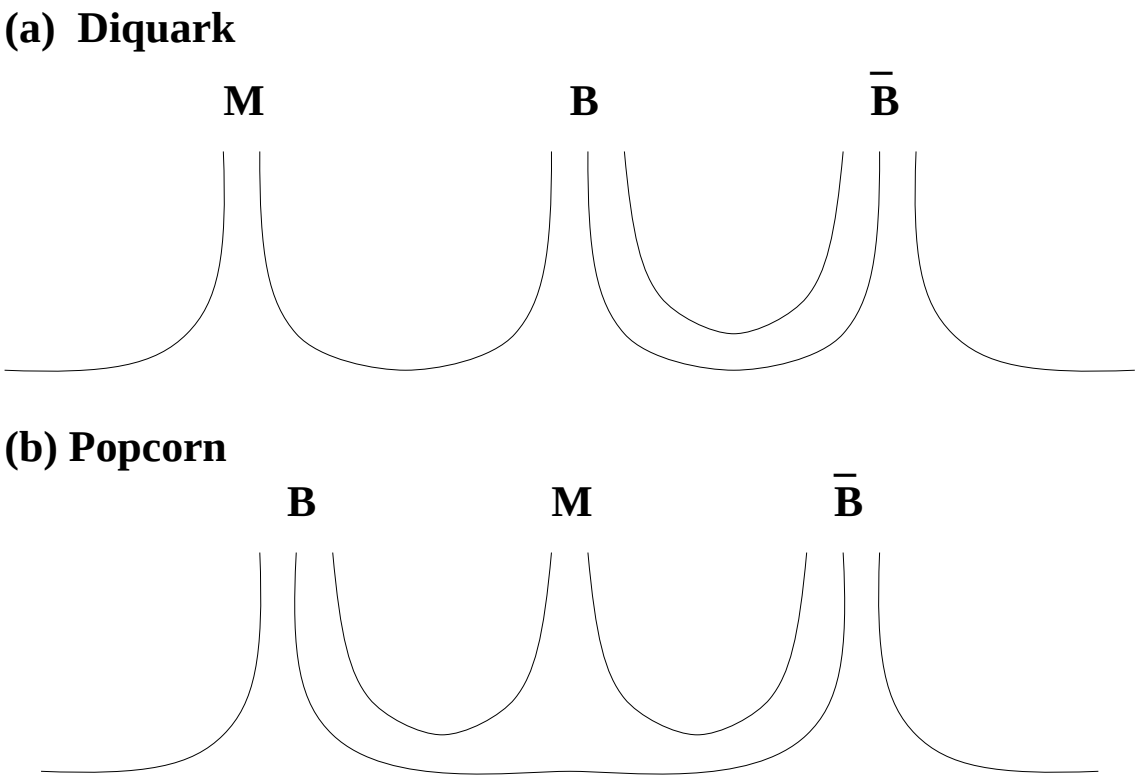

Figure 3.3: A schematic representation of baryon production in (a) the diquark and (b) the popcorn models, leading to MB$\bar{\text{B}}$ and BM$\bar{\text{B}}$ configurations respectively (from [46]).

there is a fragmenting piece of string between the gluon and each of the quarks, with a hadron straddling the gluon. The process then continues as detailed above.

After the hadronisation, it is necessary to consider the decay of resonances and other short-lived particles using decay tables to produce the final state particles.

Overall, the string model presents a more consistent and covariant picture than the independent fragmentation model and is generally in better agreement with experimental results. The Lund string model is implemented in the JETSET [28,54] event generator which uses a virtuality-ordered parton shower with an imposed angular ordering constraint to take into account colour coherence. JETSET also handles e^+e^- annihilation, particle decays and final-state parton showers; this hadronisation

scheme is combined with initial and final state parton branching in PYTHIA [28] for collisions between leptons, hadrons or photons, and in LEPTO [55] for lepton-hadron collisions. The parton shower may be re-cast in terms of colour dipole splitting, which implies colour coherence, and this is implemented in ARIADNE [35] which uses JETSET for hadronisation. One drawback of JETSET is that it has a large number of variable parameters, but it is considered to be the most faithful simulation currently available. Other variants of the string model exist, such as the UCLA model [56] in which the fragmentation function dictates the species of the hadron as well as its momentum, and the Cal-Tech scheme [57], which attempts to combine features of both the string and cluster models.

3.3.3 The cluster model

In the cluster model [58], the property of preconfinement of colour is used, so that colour-singlet clusters of partons form after the perturbative phase and then hadronise. Colour preconfinement implies that, at the end of the shower, the mass and spatial distributions of the colour-singlet clusters have a universal distribution regardless of the energy of the primary quark. The hadronisation then proceeds through the non-perturbative splitting of gluons into $q\overline{q}$ pairs; quarks and anti-quarks then combine into colour singlets. The clusters typically have masses of a few GeV ($\approx \sqrt{t_0}$). This approach is used in the HERWIG [34] event generator with a parton shower [59] algorithm that takes into account colour coherence and gives quite a good account of the data with few parameters, with the exception of the baryon sector, where recent results have shown HERWIG to be at odds with the data [46].

In the HERWIG event generator [34], the masses of the clusters are treated in three classes. First, light clusters: sometimes a cluster is too light to decay into two hadrons. In this case it is decayed into the lightest hadron and its remaining four-

momentum transferred to a neighbouring cluster. Clusters of average mass ($\approx \sqrt{t_0}$) undergo two-body decay. Hadrons are formed from quark or diquark pairs selected at random and then accepted or rejected according to their phase-space weight. If accepted, the decay is isotropic in the the rest frame of the cluster. Finally, heavy clusters are forcibly split into daughter clusters whose masses are chosen using a power law spectrum.

Since two-body decays dominate, the clusters mainly decay based on pure phase-space, resulting in few free parameters. However, the details of the heavy cluster splitting remain important for the light baryon yield and heavy hadron production. The single-body decay is important for rare heavy states. The low average mass of the clusters limits transverse momentum and strange and heavy hadrons are suppressed because of their masses.

3.3.4 Implications for gluon and quark jets

The current range of Monte Carlo models all take account of the fact that gluons carry a larger colour charge than quarks and are thus expected to radiate more gluons in a parton shower. It is expected that gluon-initiated jets will have a higher multiplicity, softer spectrum and wider angular distribution than quark jets. Experimental observations support this, but also show that b-quark jets have similar properties [30,60]. It should be noted that the differences between gluon and quark jets are less than those predicted in the asymptotic case. Experimental evidence also indicates that the topology of a jet is important in determining such properties [61].

The models discussed above treat hadrons in the same way regardless of which jet they arise from. A 'leading particle' effect would be expected so that, for example, s-quark jets should give rise to more strange particles than gluon jets. Alternative models of gluon jet fragmentation such as the recombination model [62] predict a softer pion spectrum and enhanced baryon production in gluon jets.

Chapter 4

Charged Particle Rates in Gluon and Quark Jets

4.1 Introduction

Recently, there have been investigations of the identified charged particle rates in gluon and quark jets for strange particles (K^0_S and Λ) using a tag based on the energy profile of the jet to anti-tag gluon jets [67]. The rate of these particles has been measured in previous analyses using a jet energy-ordering technique [67]. This energy-ordering technique has also been used to measure the $e^{\pm}$, $\pi^{\pm}$, $K^{\pm}$ and $p(\overline{p})$ rates in gluon and quark jets [68]. Other work has centred on using vertex tags to anti-tag gluon jets [27,30,60,65,66].

The analysis described below differs from the energy-ordering technique in that the selected gluon and quark jets are of approximately the same energy. Thus particle production is compared for jets of the same energy. The selection of jets of equal energy minimises the sensitivity of the analysis to the jet energies and simplifies the interpretation of the results.

In this analysis, 3-jet events with a symmetry such that the two lower energy jets were of approximately equal energy were selected from the OPAL data. A tag based on the energy profile of the jet was used to anti-tag gluon jets. The inclusive sample of lower energy jets was compared with the anti-tagged sample and an extended maximum likelihood fit to $\mathrm{d}E/\mathrm{d}x$ measurements was used to determine the charged particle rates in each of these two samples. A process of algebraic decomposition [27] was then used to find the identified charged particle rates in pure gluon and quark jets.

4.2 Monte Carlo and data samples

The Monte Carlo sample consisted of 6.6 million hadronic Z^0 events, generated at a centre of mass energy $\sqrt{s} = M_{Z^0}$, whilst the data consisted of 4.4 million hadronic Z^0 events from years 1990-1995, collected at $\sqrt{s} \approx M_{Z^0}$. The Monte Carlo sample was the entire available sample of OPAL-tuned JETSET 7.408 [28]. The Monte Carlo exists at both detector level (which has been passed through a full simulation of the OPAL detector and was required to satisfy the same selection criteria as the data) and at generator level (this does not include initial state radiation or detector effects and allows all charged particles with lifetimes less than 3.10^{-10} s to decay).

4.3 Event selection

To select events with gluon and quark jets of approximately the same energy, events conforming to the following requirements were selected: they must have been planar 3-jet hadronic events with one high energy jet of approximate energy $\sqrt{s}/2$ and two lower energy jets of approximately equal energies. This resulted in a Y-shaped topology for the events, with the two lower energy jets at approximately 150° to the higher energy jet. The expected background from leptonic processes such as

$e^+e^- \rightarrow \tau^+\tau^-$ and two-photon events of the type $\gamma\gamma \rightarrow q\bar{q}$ was less than 1% [67] and was neglected.

The events were required to satisfy the criteria for OPAL multihadronic events [26] with the standard OPAL definition of good tracks and clusters [27]. Events were selected if they had at least 5 good tracks. Events were then processed using the MT software package [69] to associate charged tracks and clusters of energy within the detector to reduce the double counting of particle momentum. Tracks and clusters were associated if they had the same spatial position, i.e. if the track 'pointed' at the cluster. If the energy of an associated cluster was below the expected energy response of the calorimeter for a track of that momentum then only the track momentum was used. If the energy of the cluster exceeded this threshold, then the difference between the cluster energy and the threshold was taken together with the track momentum and was used in the subsequent analysis.

Jet finding was performed using the CONE jet finder [27] and the event was selected if three jets were found with at least 2 good particles per jet. The polar angle of each jet was required to lie within the region $|\cos\theta_{\rm jet}| < 0.9$. The CONE jet finder treats each particle in turn as the axis of a cone of half angle R and sums the momenta within the cone. If the direction of the momentum sum and the cone axis do not coincide, the direction of the momentum sum is taken as a new cone axis and the process is repeated, otherwise the particles within the cone are deemed to constitute a 'proto-jet'. Proto-jets which are not identical to a previous proto-jet, and which have a total particle energy greater than ϵ, are accepted as jets. In this analysis, the resolution parameters for the CONE jet finder were a cone size $R = 30^\circ$ and a minimum jet energy $\epsilon = 5.E_{\rm vis}/\sqrt{s}$ GeV where $\sqrt{s}$ is the centre of mass energy and $E_{\rm vis}$ is the visible energy of the event. As a systematic check, a value of $\epsilon = 10$ GeV was also used.

Planar 3-jet events were selected by requiring that the sum of the angles between the jets exceeded 358°. The visible energy of a jet was required to exceed 5 GeV.

The angles between the jets were used to calculate the energies of the jets assuming massless kinematics, and the calculated and visible energies of a jet were required to agree within 20%. To ensure that events were well contained within the detector, the polar angle of the thrust axis of the event was required to satisfy $|\cos\theta_T| < 0.9$. Finally, a symmetric 3-jet configuration was selected by projecting the event into the event plane and requiring that the angle between the highest energy jet and each of the two lower energy jets be $150^\circ \pm 10^\circ$. The event plane was defined as the plane having as its normal the eigenvector associated with the smallest momentum tensor eigenvalue. A sphericity analysis was performed to find these eigenvectors, since the eigenvectors of the momentum tensor are the same as the eigenvectors of the sphericity matrix. These criteria resulted in the selection of 262 115 lower energy jets in Monte Carlo and 142 245 lower energy jets in data. The numbers of events which were selected at each stage are given in Table 4.1 for Monte Carlo and data. For the data, the mean energy of the two lowest energy jets was 24.31 GeV.

Additional cuts were applied to select tracks for the extended maximum likelihood fit. Charged tracks were included in the fit if they had greater than 20 $\mathrm{d}E/\mathrm{d}x$ hits in the jet chamber and if they had a transverse momentum of at least 0.15 GeV/c. Tracks were also required to have impact parameters with the interaction point of $|d_0| < 5$ cm for the $r-\phi$ plane and $|z_0| < 50$ cm in the z direction.

4.4 Jet tagging

Jets were tagged by considering the fraction of the visible energy of a jet within a cone of half angle 7°, co-axial with the jet axis as in Figure 4.1. In the case of the two lowest energy jets, the ratio $F_7 = E_{\mathrm{subcone}}/E_{\mathrm{jet}}$ was calculated. The resulting Monte Carlo distributions are shown in Figure 4.2 for gluon and quark jets. It can be seen that the ratio has predominantly high values for quark jets and lower values for gluon jets, as expected from experimental observations [30,60,65,66,70] that gluon

Selection Cut	No. of MC events	Data
1. Multihadronic events	6 625 467	4 372 353
2. (1) + ≥ 5 tracks + 3 jets	1 902 196 (28.7%)	1 236 263 (28.3%)
3. (2) + $> 358^\circ$	1 771 518 (26.7%)	1 102 627 (25.2%)
4. (3) + jet energy cuts	1 609 902 (24.3%)	990 384 (22.7%)
5. (4) + $\lvert\cos\theta_{\rm jet}\rvert$ and $\lvert\cos\theta_T\rvert < 0.9$	1 275 805 (19.3%)	783 734 (17.9%)
6. (5) + Y-shape	131 698 (2.0%)	74 800 (1.7%)

Table 4.1: Breakdown of the effect of selection cuts on the Monte Carlo and data.

jets are broader than quark jets. This is explained in QCD through the enhanced colour charge of the gluon compared to the quark; gluons radiate more gluons than quarks of the same energy, resulting in a broader jet with less visible energy close to the jet axis. If the value of F_7 for a jet exceeded $F_7 = 0.66$, then the other low energy jet in the event was assigned to a gluon-jet enhanced sample irrespective of its F_7 value. The cut was placed at $F_7 = 0.66$ to minimise the statistical error on the ratio of the rates of charged tracks in gluon and quark jets, as discussed in Section 4.11. The gluon-jet enhanced sample is termed the 'anti-tagged' sample, whilst the inclusive sample of lower energy jets is termed the 'normal mixture' sample.

4.5 The fit to $\mathrm{d}E/\mathrm{d}x$ information

An extended maximum likelihood fit was used to find the number of charged tracks in each sample in a given momentum range which were consistent with a given particle hypothesis. The momentum ranges which were used are given in Table 4.2. A likelihood function was constructed from the probability distributions for each of the four particle hypotheses, $\mathrm{e}^\pm$, $\pi^\pm$, $\mathrm{K}^\pm$ and $\mathrm{p}(\overline{\mathrm{p}})$, with the particle rates as free parameters of the likelihood function. The $\mathrm{e}^\pm$ hypothesis is included in the fit for

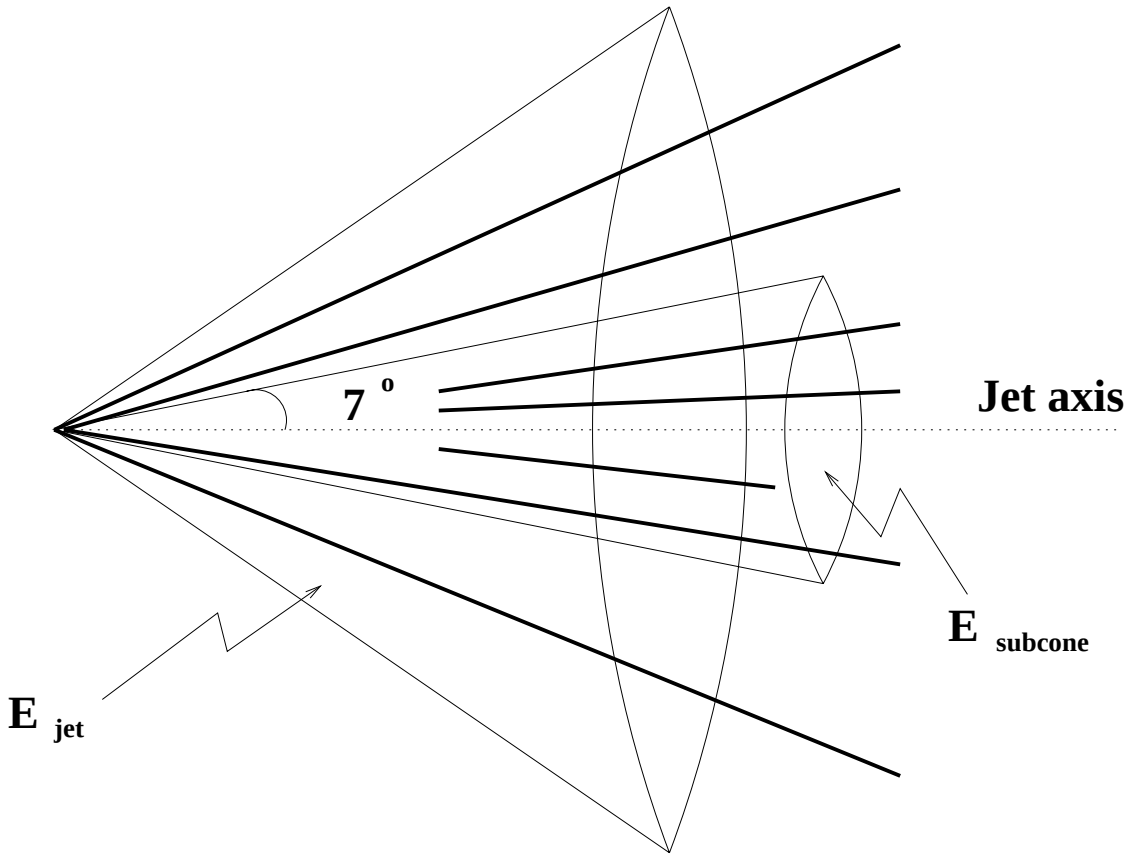

Figure 4.1: The ratio $F_7 = E_{\rm subcone}/E_{\rm jet}$ was constructed by considering a subcone of half angle 7°, co-axial with the jet axis. If tracks (here illustrated by the thick lines) lie within the subcone, they contribute to the visible energy of the subcone, $E_{\rm subcone}$.

completeness, but due to the large error on the photon conversion rate [46,71] which provides a large systematic error, results for $e^{\pm}$ are not reported. The likelihood function was

$$\mathcal{L}(\mathrm{d}E/\mathrm{d}x_1, \ldots, \mathrm{d}E/\mathrm{d}x_N; \underline{a}) = \frac{e^{-\nu}}{N!} \prod_{i=1}^{N} Q((\mathrm{d}E/\mathrm{d}x)_i, \underline{a}) \qquad (4.1)$$

where $\underline{a} = (a_\pi, a_K, a_p, a_e)$ are the number of each particle species in the given momentum range, $\nu = \sum_{j=\pi,K,p,e} a_j$ is the total number of expected tracks, N is the number of observed tracks and $(\mathrm{d}E/\mathrm{d}x)_i$ is the value of the specific energy loss

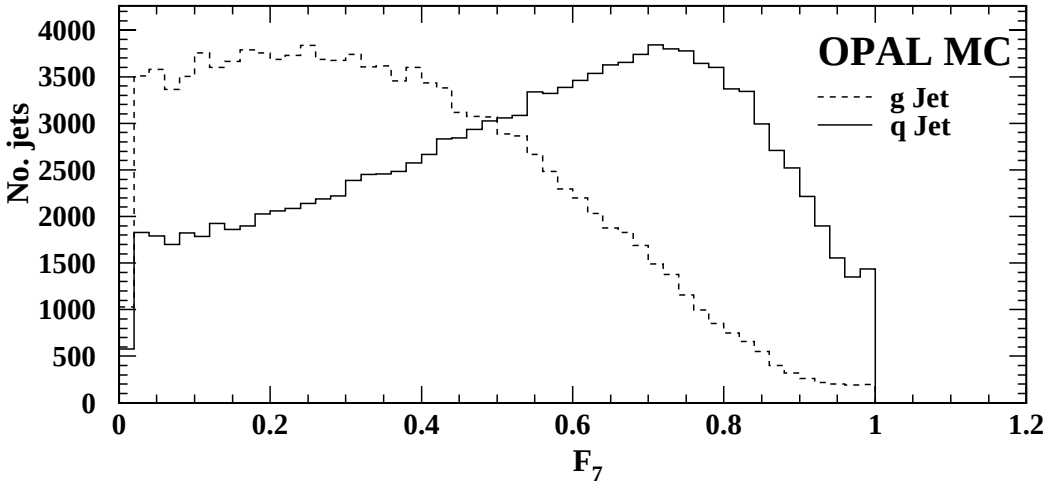

Figure 4.2: The fraction of the visible energy of a jet lying within 7° of the jet axis for gluon and quark jets (from Monte Carlo).

for track i. This is an extended maximum likelihood fit because the distribution function, Q, is normalised such that $\int Q(\mathrm{d}E/\mathrm{d}x;\underline{a})\mathrm{d}(\mathrm{d}E/\mathrm{d}x) = \nu$. The Poisson term in the likelihood function takes into account the probability of getting N tracks from a mean ν. The likelihood must incorporate the fact that tracks were observed with the $\mathrm{d}E/\mathrm{d}x$ values $(\mathrm{d}E/\mathrm{d}x)_1,\ldots,(\mathrm{d}E/\mathrm{d}x)_N$ and the fact that N tracks were observed when ν were expected. Thus the Q describes the shape and size of the expected $\mathrm{d}E/\mathrm{d}x$ distribution [72]. Appendix A gives the derivation of this likelihood function.

The distribution function, Q, is the sum of the products of the individual particle probability density functions and the number of each particle species,

$$Q((\mathrm{d}E/\mathrm{d}x)_i,\underline{a}) = \sum_{j=\pi,K,p,e} a_j P_j((\mathrm{d}E/\mathrm{d}x)_i;\mu_j(p_i),\sigma_j,\underline{\alpha}) \qquad (4.2)$$

Bin	Momentum range (GeV/c)	Bin	Momentum range (GeV/c)
1	0.23 - 0.27	13	1.42 - 1.61
2	0.27 - 0.32	14	1.61 - 1.92
3	0.32 - 0.37	15	1.92 - 2.23
4	0.37 - 0.43	16	2.23 - 2.59
5	0.43 - 0.50	17	2.59 - 3.00
6	0.50 - 0.58	18	3.00 - 3.49
7	0.58 - 0.67	19	3.49 - 4.06
8	0.67 - 0.78	20	4.06 - 7.39
9	0.78 - 0.90	21	7.39 - 13.46
10	0.90 - 0.98	22	13.46 - 29.96
11	0.98 - 1.22	23	29.96 - 45.60
12	1.22 - 1.42		

Table 4.2: The momentum ranges in which the extended maximum likelihood fit was applied.

where P_j is the single particle $\mathrm{d}E/\mathrm{d}x$ distribution for particle species j, μ_j is the expected mean $\mathrm{d}E/\mathrm{d}x$ measurement for species j, σ_j is the width of the distribution and p_i is the momentum of track i. P_j is the probability of obtaining the measurement $(\mathrm{d}E/\mathrm{d}x)_i$ under the particle hypothesis j.

The single particle distributions P_j are normalised to 1 and fulfill the requirements of a probability. They may be approximated by Gaussians of mean μ_j and width σ_j, with an additional tail described by the parameters $\underline{\alpha} = (\alpha_1, \alpha_2, \alpha_3)$. The Sternheimer-Peirls parameterisation of the Bethe-Bloch equation is used to compute the expected energy loss, $\mu_j(p_i)$, of track i with momentum p_i for the particle hypothesis j. The width σ_j is the expected experimental error which is determined from the experimental error $\sigma_{(\mathrm{d}E/\mathrm{d}x)_i}$ and the measured energy loss, $(\mathrm{d}E/\mathrm{d}x)_i$, of track i [5]:

$$\sigma_j = \frac{\sigma_{(\mathrm{d}E/\mathrm{d}x)_i}}{(\mathrm{d}E/\mathrm{d}x)_i}\mu_j(p_i) \tag{4.3}$$

For a given range of momenta, the $\mathrm{d}E/\mathrm{d}x$ distribution for a given charged particle species is approximately Gaussian with a tail which can be parameterised by a Breit-Wigner [68]. For the case of more than one particle species, the $\mathrm{d}E/\mathrm{d}x$ distributions can be approximated by a set of overlapping Gaussians (Figure 4.3).

In general, the $\mathrm{d}E/\mathrm{d}x$ distributions show a tail at large $\mathrm{d}E/\mathrm{d}x$ values which is due to the limited double track resolution of the jet chamber [5]; two nearby tracks may be reconstructed as a single track which results in a $\mathrm{d}E/\mathrm{d}x$ measurement that is too large. A small tail is also seen at low $\mathrm{d}E/\mathrm{d}x$ due to detector effects in a dense tracking environment which the Monte Carlo does not simulate.

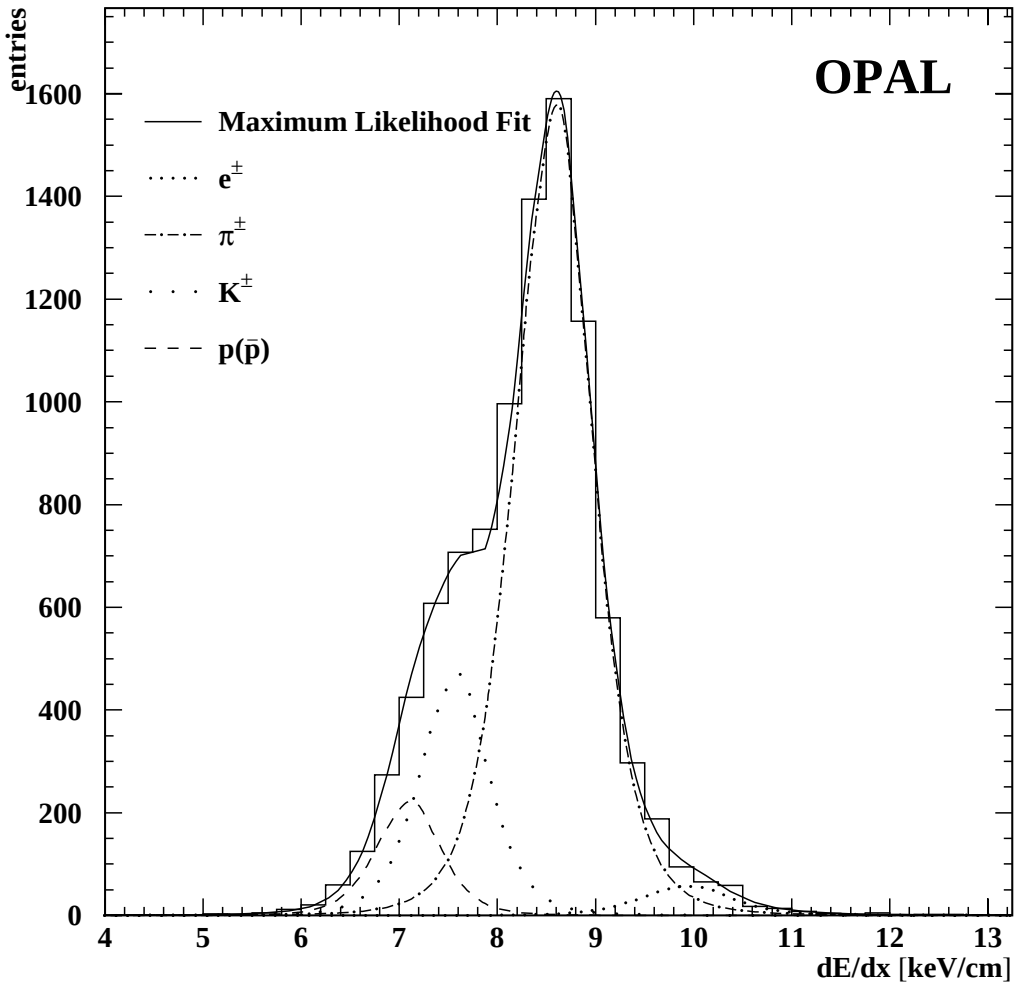

Figure 4.3: The $\mathrm{d}E/\mathrm{d}x$ distributions in the momentum range 3.669 - 3.857 GeV/c. The results of the extended maximum likelihood fit and the probability distributions of the individual particle species are shown (from [68]).

Parameter	Monte Carlo	Data
α_1	0.056 ± 0.002	0.102 ± 0.007
α_2	1.84 ± 0.02	0.37 ± 0.06
α_3	1.30 ± 0.02	1.14 ± 0.07

Table 4.3: Values of the parameters that determine the Breit-Wigner contribution for data and Monte Carlo.

The single particle distributions are parameterised by the ideal Gaussian and an additional Breit-Wigner term,

$$P_j((\mathrm{d}E/\mathrm{d}x)_i;\mu_j(p_i),\sigma_j,\underline{\alpha}) = \frac{1}{1+\alpha_1}\left\{\frac{1}{\sqrt{2\pi}\sigma_j}\exp\left(-\frac{1}{2}\left(\frac{(\mathrm{d}E/\mathrm{d}x)_i-\mu_j(p_i)}{\sigma_j}\right)^2\right) + \frac{\alpha_1}{\pi}\frac{\sigma_j\alpha_3/2}{((\mathrm{d}E/\mathrm{d}x)_i-\mu_j(p_i)-\sigma_j\alpha_2)^2+(\sigma_j\alpha_3/2)^2}\right\} \quad (4.4)$$

where the parameters $\underline{\alpha}$ determine the Breit-Wigner contribution. The values for $\underline{\alpha}$ are given in Table 4.3. The differences between the values of $\underline{\alpha}$ used for the data and the Monte Carlo are due to the fact that the Monte Carlo does not simulate the tail of the distribution at low $\mathrm{d}E/\mathrm{d}x$.

The parameterisation of the P_j was obtained from a study of the normalised $\mathrm{d}E/\mathrm{d}x$,

$$(\mathrm{d}E/\mathrm{d}x)_{norm,i} = \frac{(\mathrm{d}E/\mathrm{d}x)_i-\mu_j(p_i)}{\sigma_j} \quad (4.5)$$

where $(\mathrm{d}E/\mathrm{d}x)_i$ is the measured $\mathrm{d}E/\mathrm{d}x$ of track i. The values of $\underline{\alpha}$ used have been obtained from a study of $\pi^\pm$ from K^0_S decays [68] and are not expected to depend on particle species. This has been verified by examining identified protons from Λ decays [68].

The single particle $\mathrm{d}E/\mathrm{d}x$ distributions for $\mathrm{e}^\pm$, $\pi^\pm$, $\mathrm{K}^\pm$ and $\mathrm{p}(\overline{\mathrm{p}})$ were parameterised as described above and the extended maximum likelihood fit was performed with `MINUIT` [73] to find the number of each species in each bin of momentum. The

term in $N!$ is a constant, allowing the negative log likelihood to be written as

$$-\ln(\mathcal{L}) = -\sum_{i=1}^{N} \ln Q((\mathrm{d}E/\mathrm{d}x)_i; \underline{a}) + \nu \tag{4.6}$$

which was minimised for a given range of momentum. From the results of the fit in each momentum range (see Table 4.2), a momentum-dependent distribution of the number of each particle species in the normal mixture and anti-tagged jet samples was constructed. The momentum ranges were converted to ranges of x_p, where $x_p = 2p/\sqrt{s}$ and p is the track momentum, and x_p distributions were constructed. These distributions were then normalised by the jet production cross-section for each sample, σ_{jet}, to give $1/\sigma_{\mathrm{jet}}\ \mathrm{d}\sigma/\mathrm{d}x_p$ distributions. The integrals of these normalised distributions give the average number of identified charged particles per jet for the normal mixture and anti-tagged jet samples.

The fit efficiency has been investigated for Monte Carlo, and is shown in Figure 4.4 for 132 000 Monte Carlo events which satisfied the selection criteria for inclusion in the fit. Here the ratio of the results returned by the fit to the true particle rate determined using Monte Carlo information is shown as a function of x_p for the three particle species, $\pi^{\pm}$, $\mathrm{K}^{\pm}$ and $\mathrm{p}(\overline{\mathrm{p}})$ for momenta above 0.23 GeV/c. The expected values of $\mathrm{d}E/\mathrm{d}x$ for the species $\mathrm{e}^{\pm}$, $\pi^{\pm}$, $\mathrm{K}^{\pm}$, $\mathrm{p}(\overline{\mathrm{p}})$ and $\mu^{\pm}$ are also shown as a function of x_p. The performance of the fit in the chosen ranges of x_p is typically good to within 10%. In certain regions, the fit fails because the $\mathrm{d}E/\mathrm{d}x$ curves for different species overlap. Monte Carlo information was used to interpolate the data x_p distributions in these regions, which lie between the vertical dotted lines.

4.6 Correction for background contributions

Due to the similar values of $\mathrm{d}E/\mathrm{d}x$ for $\pi^{\pm}$ and $\mu^{\pm}$ for a given momentum, the $\pi^{\pm}$ rate contains a contribution from muons that the extended maximum likelihood

fit cannot resolve. The muon background to the $\pi^{\pm}$ rate was subtracted using Monte Carlo information. JETSET 7.4 Monte Carlo was examined at the detector level and Monte Carlo information was used to allow perfect identification of $\mu^{\pm}$ and $\pi^{\pm}$ and a determination of the $\mu^{\pm}$ and $\pi^{\pm}$ rates. For each range of momentum, the predicted $\mu^{\pm}$ rate was subtracted from the fit results for $\pi^{\pm}$. This correction is less than 5% over the entire momentum range [68]. The error on the muon background rate was assumed to be less than 10% [75] and was fed through to the systematic error. It should be noted that the muon chambers were not used for this correction because low momentum muons do not reach the muon chambers. There is also a $\Sigma^{\pm}$ and $\Xi^{\pm}$ background in the proton rate. This amounts to a correction of less than 2% for momenta above 20 GeV/c and was neglected.

There is a substantial contribution to the $e^{\pm}$ rate from photon conversions (up to a maximum of 80% for momenta below 1 GeV/c [68]). The rate of all charged tracks was corrected for this effect using Monte Carlo information. The photon conversion rate is known to 5% [46, 71], and it was assumed that the detector simulation for the conversion rate was correct to within 5%.

In the momentum range $p < 1$ GeV/c nuclear interactions within the detector are a large background for positively charged tracks; for this reason, only negatively charged tracks were used for this momentum range and the rate was then doubled using charge conservation to find the true particle rate. Monte Carlo information was then used to correct for any remaining backgrounds due to nuclear interactions in each of the normal mixture and anti-tagged samples. This correction is typically of the order of 10% for $\pi^{\pm}$ [68]. The error on the number of tracks arising from nuclear interactions was assumed to be less than 20% [75]. The error on this correction was fed through to the systematic error and was combined in quadrature with the other sources of systematic errors.

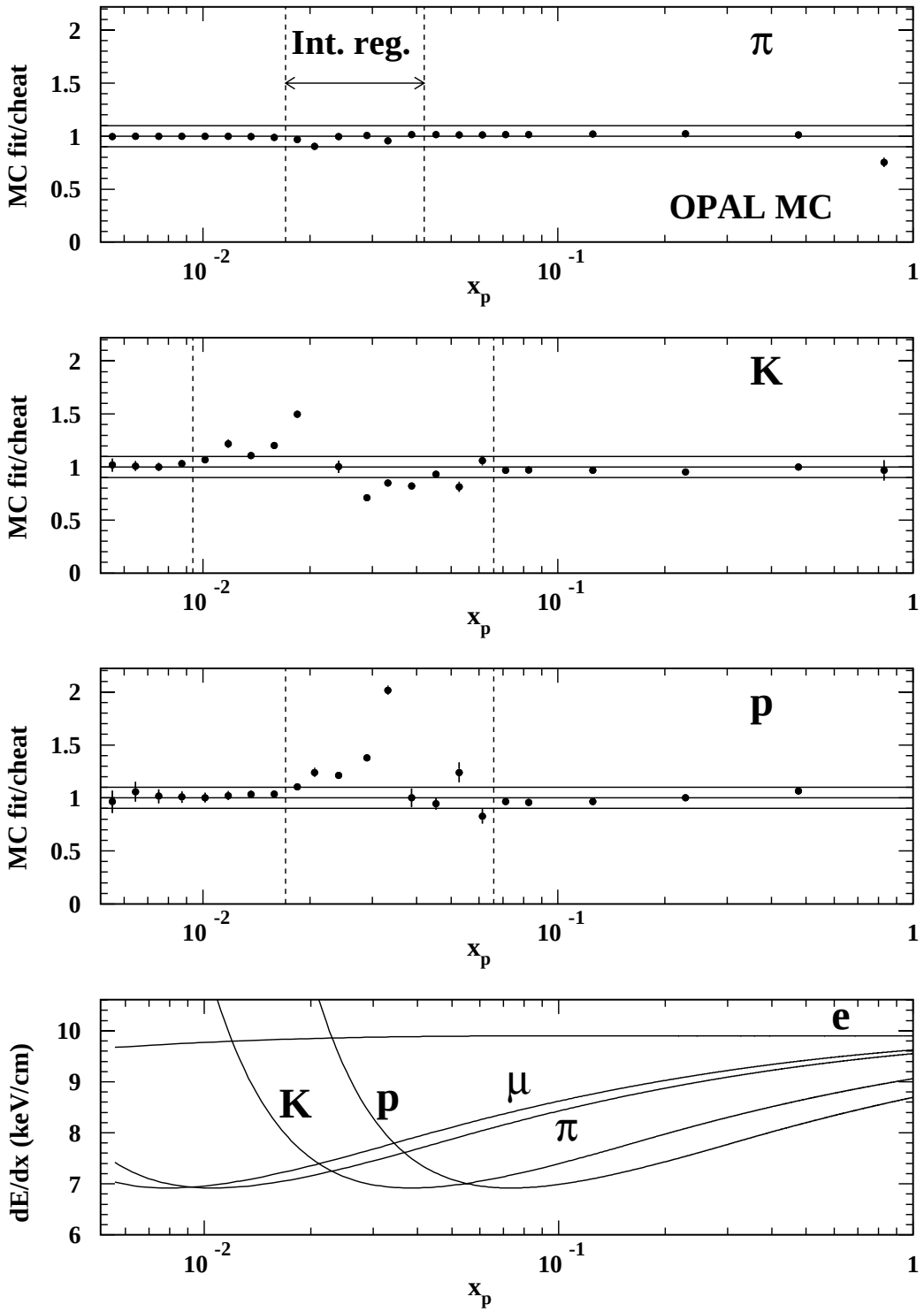

Figure 4.4: The peformance of the maximum likelihood fit is compared with the true rate ('MC cheat') as a function of x_p for each of the three species in Monte Carlo. The bottom plot shows the expected $\mathrm{d}E/\mathrm{d}x$ values.

4.7 Pure gluon and quark jets

The extended maximum likelihood fit returned the identified charged particle rates in the normal mixture and anti-tagged samples, defined as the average number of identified charged particles per jet for each sample. A process of algebraic decomposition [27] was used to extract the distributions and the rates of identified charged particles in gluon and quark jets.

The tagging rate, $\mathcal{P}_{\rm tag}$, was defined as being the fraction of selected events which contained jets that were anti-tagged. The anti-tagging purity, ρ_g, was defined as being the fraction of anti-tagged Monte Carlo detector level jets that were associated with a gluon at the parton level. According to Monte Carlo studies, the normal mixture purity, ρ_{nm}, defined as the fraction of normal mixture detector level jets associated with a gluon, was $48.67 \pm 0.03\%$ whilst $\rho_g = 75.02 \pm 0.44\%$ and $\mathcal{P}_{\rm tag} = 47.57\%$.

If we take the production rate of particle i in a bin of x_p in the normal mixture sample to be $D^i_{nm}(x_p)$, we can write

$$D^i_{nm}(x_p) = \rho_{nm} G^i(x_p) + (1 - \rho_{nm}) Q^i(x_p) \tag{4.7}$$

where ρ_{nm} is the gluon jet content of the normal mixture sample, $G^i(x_p)$ is the production rate of particle i in pure gluon jets and $Q^i(x_p)$ is the production rate in pure quark jets. The rate in the anti-tagged sample may be written as

$$D^i_{atag}(x_p) = \rho_g G^i(x_p) + (1 - \rho_g) Q^i(x_p) \tag{4.8}$$

where ρ_g is the anti-tagging purity. From Equations 4.7 and 4.8, the rate of a given species i in pure gluon jets as a function of x_p may be expressed as:

$$G^i(x_p) = \frac{(1 - \rho_{nm}) D^i_{atag}(x_p) - (1 - \rho_g) D^i_{nm}(x_p)}{\rho_g - \rho_{nm}} \tag{4.9}$$

Similarly, the rate of a given species in pure quark jets as a function of x_p may be written as:

$$Q^i(x_p) = \frac{\rho_{nm} D^i_{atag}(x_p) - \rho_g D^i_{nm}(x_p)}{\rho_{nm} - \rho_g} \tag{4.10}$$

and hence their ratio

$$\mathcal{R}^i_{gq} = \frac{\int G^i(x_p)\mathrm{d}x_p}{\int Q^i(x_p)\mathrm{d}x_p} = \frac{G^i}{Q^i} \tag{4.11}$$

where G^i is the total production rate of particle i in gluon jets and Q^i is the total production rate of particle i in quark jets.

4.8 Detector corrections

The identified charged particle rates are presented as $1/\sigma_{\mathrm{jet}}\ \mathrm{d}\sigma/\mathrm{d}x_p$ distributions of particle i in gluon and quark jets. Corrections for detector effects and acceptance were applied to these distributions after the algebraic decomposition on a bin-by-bin basis. These correction factors were derived from a study of OPAL-tuned JETSET 7.408 Monte Carlo [28] at the generator level and detector level.

The distributions have already been corrected for any background in the measured production rates, and the algebraic decomposition yields pure gluon and quark jet distributions. Because this result is specific to the energy of the jets, there is no need to correct for the topology of the event or for the rejection of, e.g, di-jet events.

The detector level Monte Carlo was required to satisfy the same event selection criteria as the data, and jet finding was performed with the same parameters as described above. Monte Carlo information was then used to identify the gluon and quark jets (removing the tagging dependence) and to allow perfect identification of each particle species. The $1/\sigma_{\mathrm{jet}}\ \mathrm{d}\sigma/\mathrm{d}x_p$ distribution was then constructed for each species in gluon and quark jets.

This was then repeated for the generator level Monte Carlo. Monte Carlo information was used to allow perfect gluon and quark identification and particle

identification, after jet finding had been performed on the generator level events passing the same selection criteria as the data, with the exception of the $\cos\theta_T$ and $\cos\theta_{\rm jet}$ cuts.

To achieve the association between a jet and an underlying gluon or quark, the Monte Carlo events were examined at the parton level. The directions of the primary quark and anti-quark after the termination of the parton shower were compared with the directions of the hadronic jets at detector level and the two hadronic jets closest in angle to the directions of the primary quark and anti-quark were classified as detector level quark jets. The remaining jet was then identified as the gluon jet. A similar procedure associated a quark or gluon with a generator level hadronic jet.

For each particle species in gluon and quark jets, the correction factors were calculated by considering the $1/\sigma_{\rm jet}\ {\rm d}\sigma/{\rm d}x_p$ distributions of that particle in generator level jets and in detector level jets. Each x_p range of the data distribution was corrected by the ratio of the value of the distribution in the corresponding generator level x_p range to the value of the distribution in the corresponding detector level range. The fully corrected distributions are shown in Figure 4.6 for $\pi^{\pm}$, Figure 4.7 for $\rm K^{\pm}$ and Figure 4.8 for $\rm p(\overline{p})$.

4.9 The Monte Carlo interpolation

In the region where the ${\rm d}E/{\rm d}x$ curves overlap, the extended maximum likelihood fit cannot distinguish between the particle species. Monte Carlo information was used to interpolate the distributions in these regions. The solid lines in Figures 4.6, 4.7 and 4.8 were used for the interpolation.

For each distribution, the generator level Monte Carlo prediction was multiplied by a factor of $x_p^{\gamma}(1-x_p)^{\delta}$, where γ and δ were determined by a fit to the data. The motivation for this comes from the Lund symmetric fragmentation function, which

Species, gluon jets	γ	δ
$\pi^{\pm}$	0.003 ± 0.005	-0.141 ± 0.182
$K^{\pm}$	-0.024 ± 0.028	-0.746 ± 0.287
$p(\overline{p})$	-0.123 ± 0.045	0.121 ± 0.481
Species, quark jets	γ	δ
$\pi^{\pm}$	0.007 ± 0.004	-0.118 ± 0.220
$K^{\pm}$	0.024 ± 0.033	-2.566 ± 0.544
$p(\overline{p})$	-0.006 ± 0.037	2.075 ± 0.709

Table 4.4: Values of the parameters that determine the scaling of the Monte Carlo interpolation for the 3 species in gluon and quark jets.

has the form

$$F(x_p) \propto x_p^{-1}(1-x_p)^a \exp(-bm_\perp^2/x_p) \tag{4.12}$$

so the scaling chosen here alters the shape of the Lund symmetric fragmentation function. For each distribution, the value of the Monte Carlo scaled using the relevant value of γ and δ was used as an interpolation. As a systematic check these values were altered by their errors and the interpolation was repeated. The values of the fitted parameters are shown in Table 4.4.

Generator level Monte Carlo information was used to extrapolate the identified charged particle rates below $p = 0.23$ GeV/c. The integrals of these distributions, using the data where available and the fit based on the Monte Carlo in the region where the dE/dx curves overlap, give the identified charged particle production rates in gluon and quark jets for species i, G^i and Q^i respectively, and hence their ratio.

4.10 Results

The fully corrected $1/\sigma_{\rm jet}\ {\rm d}\sigma/{\rm d}x_p$ distributions for gluon and quark jets are shown in Figure 4.6 for $\pi^{\pm}$, Figure 4.7 for $\rm K^{\pm}$ and Figure 4.8 for $\rm p(\overline{p})$, together with the fit based on the JETSET Monte Carlo which was used for the interpolation. The JETSET generator level predictions are also shown for gluon and quark jets. The distributions for all charged tracks are shown in Figure 4.5, where the softer nature of the gluon fragmentation function can clearly be seen.

The total number of tracks seen in the two samples is detailed in Table 4.6. After the interpolation with the Monte Carlo, the distributions were integrated and the rates of the identified charged particles in gluon jets, defined as the average number of identified charged particles per gluon jet, were found to be

$$\begin{aligned} G^{\rm all} &= 6.54 \pm 0.05 \pm 0.07 \\ G^{\pi} &= 5.89 \pm 0.04 \pm 0.17 \\ G^{\rm K} &= 0.75 \pm 0.02 \pm 0.10 \\ G^{\rm p} &= 0.39 \pm 0.03 \pm 0.03 \end{aligned}$$

where the first errors are statistical and the second are systematic. For quark jets the rates were

$$\begin{aligned} Q^{\rm all} &= 5.92 \pm 0.06 \pm 0.04 \\ Q^{\pi} &= 5.01 \pm 0.04 \pm 0.12 \\ Q^{\rm K} &= 0.78 \pm 0.02 \pm 0.12 \\ Q^{\rm p} &= 0.35 \pm 0.02 \pm 0.03 \end{aligned}$$

where the first errors are statistical and the second are systematic. Details of the components of the systematic error are given in Table 4.9.

The fully corrected ratios of identified charged particle production rates in gluon and quark jets were found to be

$$\begin{aligned}
\mathcal{R}_{gq}^{\mathrm{all}} &= 1.10 \pm 0.01 \pm 0.02 \\
\mathcal{R}_{gq}^{\pi} &= 1.17 \pm 0.01 \pm 0.05 \\
\mathcal{R}_{gq}^{\mathrm{K}} &= 0.96 \pm 0.03 \pm 0.12 \\
\mathcal{R}_{gq}^{\mathrm{p}} &= 1.12 \pm 0.10 \pm 0.11
\end{aligned}$$

where the first errors are statistical and the second are systematic. Details of the contributions to the systematic error are given in Table 4.10. These results may be compared with the JETSET 7.4 values of 1.17 for all charged tracks, 1.18 for $\pi^{\pm}$, 0.99 for $\mathrm{K}^{\pm}$ and 1.72 for $\mathrm{p}(\overline{\mathrm{p}})$. The Monte Carlo predictions and the fully corrected data values are shown in Table 4.7 and Table 4.8.

Previous OPAL analyses have examined identified charged particle rates in gluon and quark jets in various topologies. A similar analysis to that described above has been carried out for $\mathrm{K}_{\mathrm{S}}^{0}$ and Λ particles [67] in which the ratios of particle production rates in gluon and quark jets were found to be $\mathcal{R}_{gq}^{\mathrm{all}} = 1.12 \pm 0.01 \pm 0.01$, $\mathcal{R}_{gq}^{\mathrm{K}_{\mathrm{S}}^{0}} = 1.05 \pm 0.08 \pm 0.09$ and $\mathcal{R}_{gq}^{\Lambda} = 1.32 \pm 0.11 \pm 0.18$. An earlier OPAL analysis [27] found $\mathcal{R}_{gq}^{\mathrm{all}} = 1.10 \pm 0.02 \pm 0.02$.

An OPAL analysis using vertex information to anti-tag gluon jets and the DURHAM ($k_{\perp}$ algorithm) jet finder [74] found $\mathcal{R}_{gq}^{\mathrm{all}} = 1.25 \pm 0.02 \pm 0.03$ [27], whilst a similar DELPHI analysis found $\mathcal{R}_{gq}^{\mathrm{all}} = 1.24 \pm 0.02 \pm 0.03$ [65] and ALEPH have found $\mathcal{R}_{gq}^{\mathrm{all}} = 1.19 \pm 0.04 \pm 0.02$ [60]. These results tend to be higher than the values found when the CONE jet finder is used. This is thought to be due to the fact that the DURHAM jet finder requires all tracks to be assigned to a jet, so some particles far away from the jet axis may be included in the jet. This is not the case for the CONE jet finder.

An analysis based on the ordering of the jet energy [67,68] has also been performed (the gluon jet is often the lowest energy jet). In these previous analyses, the ratios of the rates of identified charged particles in gluon and quark jets were normalised by the ratio for all charged particles. In the current analysis, this procedure

Species	$\mathcal{R}^i_{gq}/\mathcal{R}^{\rm all}_{gq}$	Analysis
$\pi^\pm$	$1.06 \pm 0.02 \pm 0.05$	This analysis
$K^\pm$	$0.87 \pm 0.03 \pm 0.11$	This analysis
$K^\pm$	$0.93 \pm 0.04 \pm 0.02$	DELPHI, equal energy jets [66]
K^0_S	$0.94 \pm 0.07 \pm 0.07$	OPAL, equal energy jets [67]
K^0_S	$1.13 \pm 0.09 \pm 0.13$	DELPHI, equal energy jets [66]
$p(\overline{p})$	$1.01 \pm 0.09 \pm 0.10$	This analysis
$p(\overline{p})$	$1.12 \pm 0.11 \pm 0.04$	DELPHI, equal energy jets [66]
Λ	$1.18 \pm 0.10 \pm 0.17$	OPAL, equal energy jets [67]
Λ	$1.40 \pm 0.30 \pm 0.23$	DELPHI, equal energy jets [66]
$\pi^\pm$	$1.02 \pm 0.01 \pm 0.01$	OPAL, jet energy ordering [68]
$K^\pm$	$0.95 \pm 0.02 \pm 0.03$	OPAL, jet energy ordering [68]
K^0_S	$1.10 \pm 0.02 \pm 0.02$	OPAL, jet energy ordering [67]
$p(\overline{p})$	$1.10 \pm 0.02 \pm 0.03$	OPAL, jet energy ordering [68]
Λ	$1.41 \pm 0.04 \pm 0.04$	OPAL, jet energy ordering [67]

Table 4.5: A comparison of the results with the values from previous analyses.

yields:

$$\begin{aligned}
\mathcal{R}^{\pi}_{gq}/\mathcal{R}^{\rm all}_{gq} &= 1.06 \pm 0.02 \pm 0.05 \\
\mathcal{R}^{\rm K}_{gq}/\mathcal{R}^{\rm all}_{gq} &= 0.87 \pm 0.03 \pm 0.11 \\
\mathcal{R}^{\rm p}_{gq}/\mathcal{R}^{\rm all}_{gq} &= 1.01 \pm 0.09 \pm 0.10
\end{aligned}$$

The corresponding values for JETSET are 1.02 for $\pi^\pm$, 0.86 for $K^\pm$ and 1.47 for $p(\overline{p})$. Table 4.5 compares these results with a previous OPAL analysis for strange particles in jets of the same energy [67], OPAL jet energy ordering analyses [67,68] and a DELPHI analysis of jets of approximately the same energy, which anti-tagged gluon jets through vertex information [66].

The JETSET results, with the exception of the $p(\overline{p})$ rate in quark jets, are in good agreement with the data. The difference in the $p(\overline{p})$ rate in quark jets accounts for the difference in $\mathcal{R}_{gq}^{p}$ and in the ratio normalised by $\mathcal{R}_{gq}^{all}$. The results reported here for the ratio of the rate of all charged particles in gluon and quark jets agree well with previous results. The JETSET ratios normalised by $\mathcal{R}_{gq}^{all}$ are in excellent agreement with the data with the exception of the result for $p(\overline{p})$, and the data are consistent with previous results.

It should be noted that the jet energy-ordering method utilises far higher statistics, accounting for the smaller errors. The jet energy-ordering analysis does not, in general, use jets of equal energies, so topology and jet energy considerations become important [61] in the interpretation of the results.

4.11 Choice of the F_7 cut

The Monte Carlo prediction of the expected statistical error on the ratio of the rate of all charged tracks in gluon jets to that in quark jets was investigated as a function of the cut placed on F_7. The expected value of the ratio, $\mathcal{R}_{gq}^{all}$, of the rate of charged tracks in a gluon jet to the rate of charged tracks in a quark jet, calculated as in Section 4.7, is shown in Figure 4.9(a) and the percentage error is shown in Figure 4.9(b). It can be seen that $\mathcal{R}_{gq}^{all}$ is stable over a wide range of cut values. A second order polynomial was fitted to the percentage error distribution and the position of the minimum of the polynomial was calculated. This was found to be at $F_7 = 0.66$.

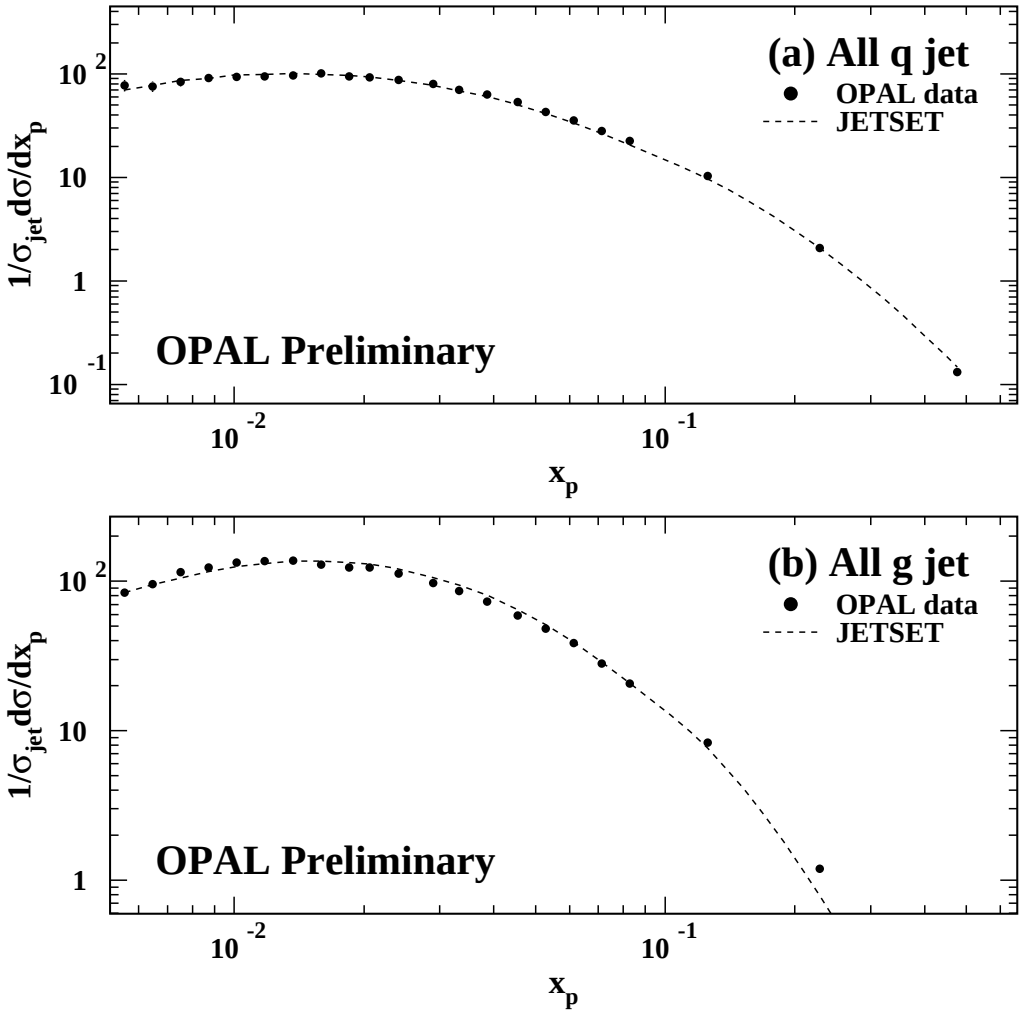

Figure 4.5: The x_p distributions for all charged tracks in (a) quark jets and (b) gluon jets and the JETSET generator level predictions.

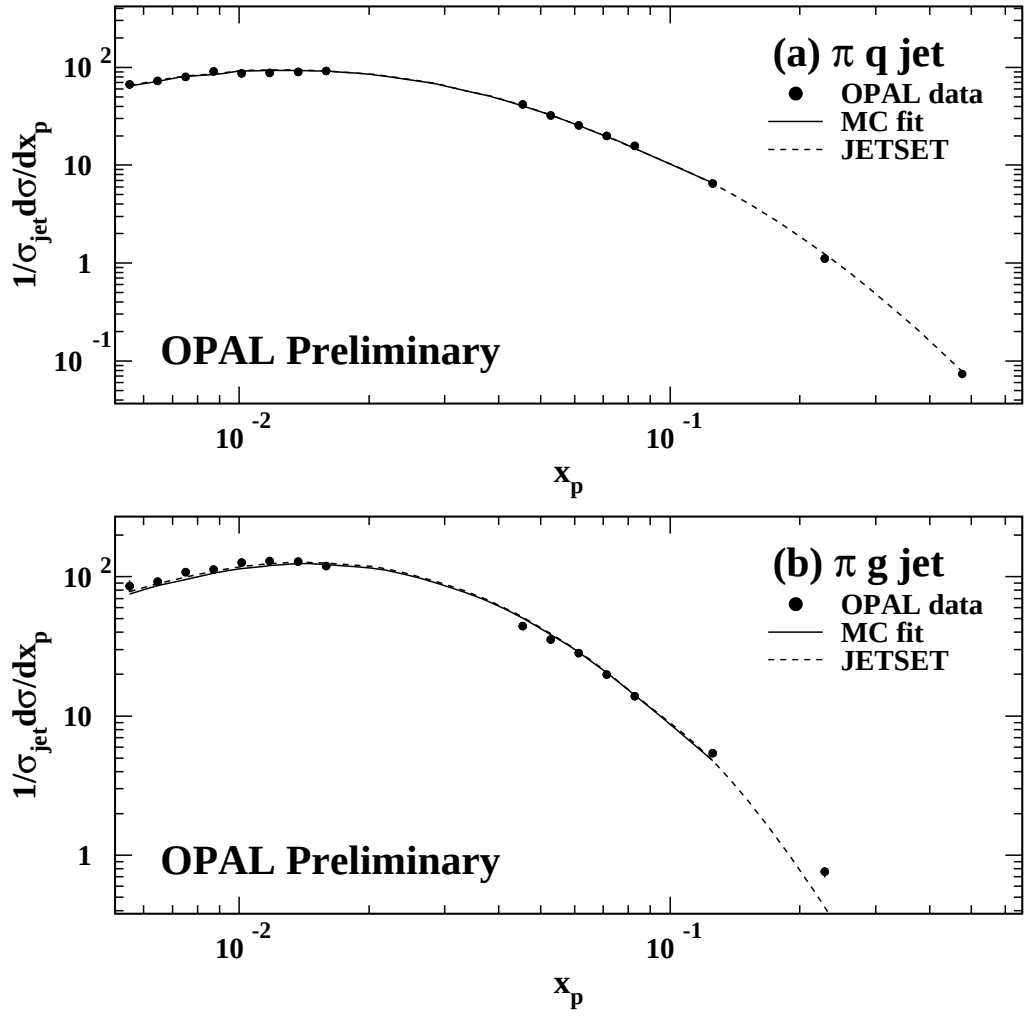

Figure 4.6: The x_p distributions for $\pi^{\pm}$ in (a) quark jets and (b) gluon jets, with the JETSET generator level predictions as the dotted line. The solid line indicates a fit based on the JETSET Monte Carlo.

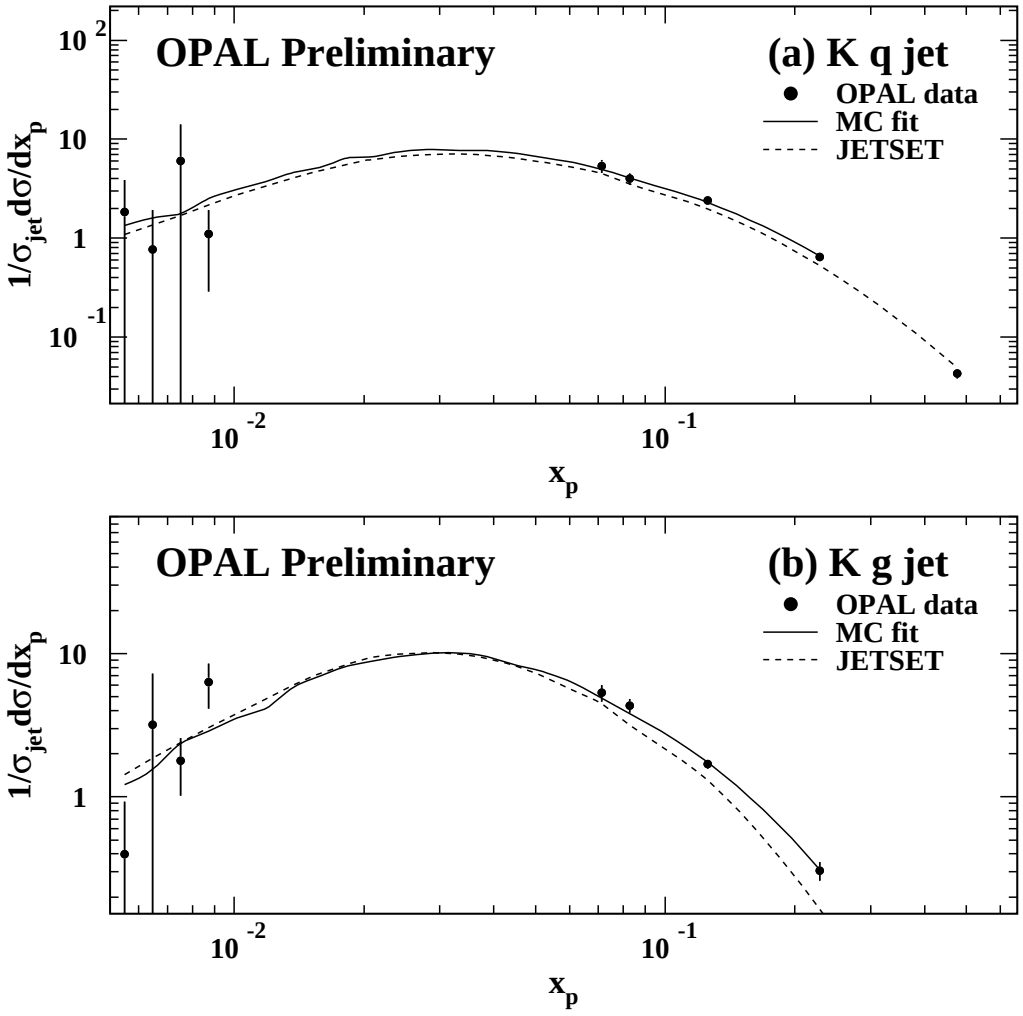

Figure 4.7: The x_p distributions for $K^{\pm}$ in (a) quark jets and (b) gluon jets, with the JETSET generator level predictions as the dotted line. The solid line indicates a fit based on the JETSET Monte Carlo.

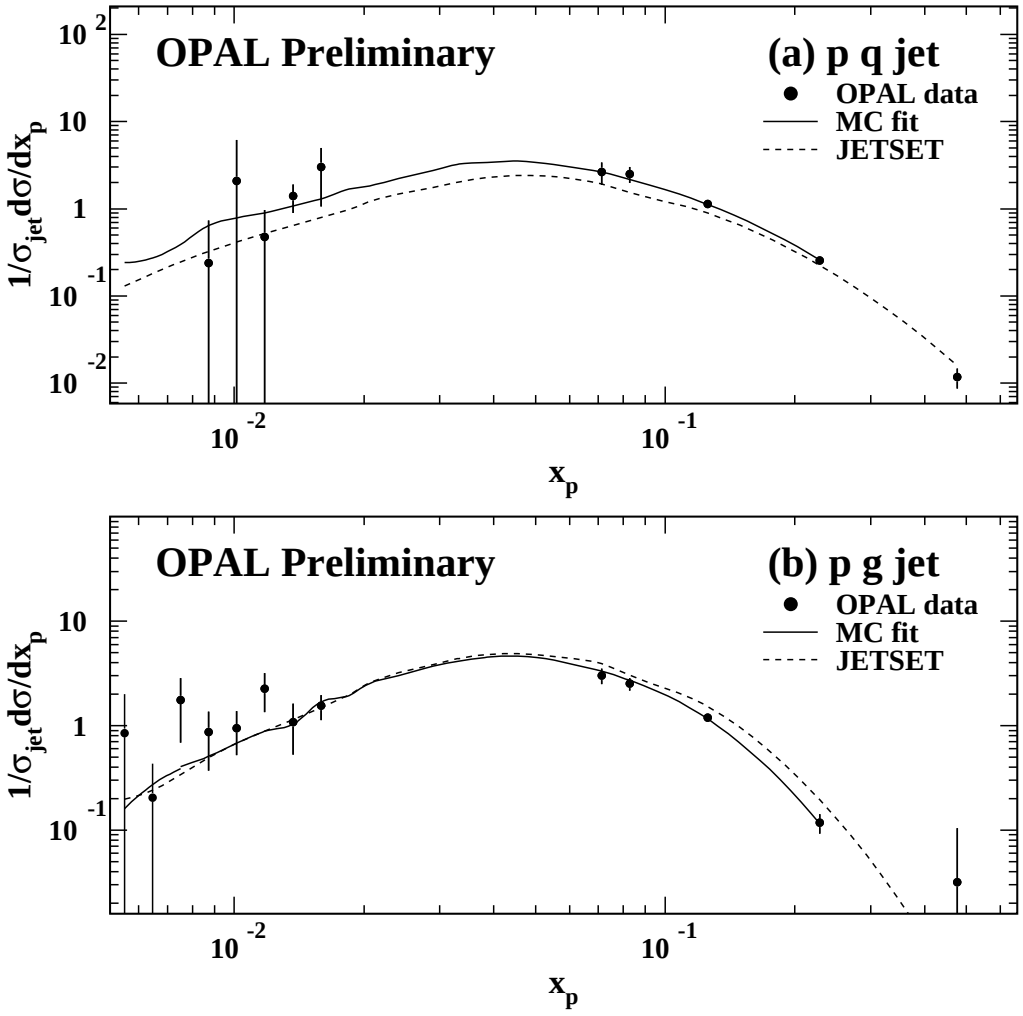

Figure 4.8: The x_p distributions for p($\overline{\text{p}}$) in (a) quark jets and (b) gluon jets, with the JETSET generator level predictions as the dotted line. The solid line indicates a fit based on the JETSET Monte Carlo.

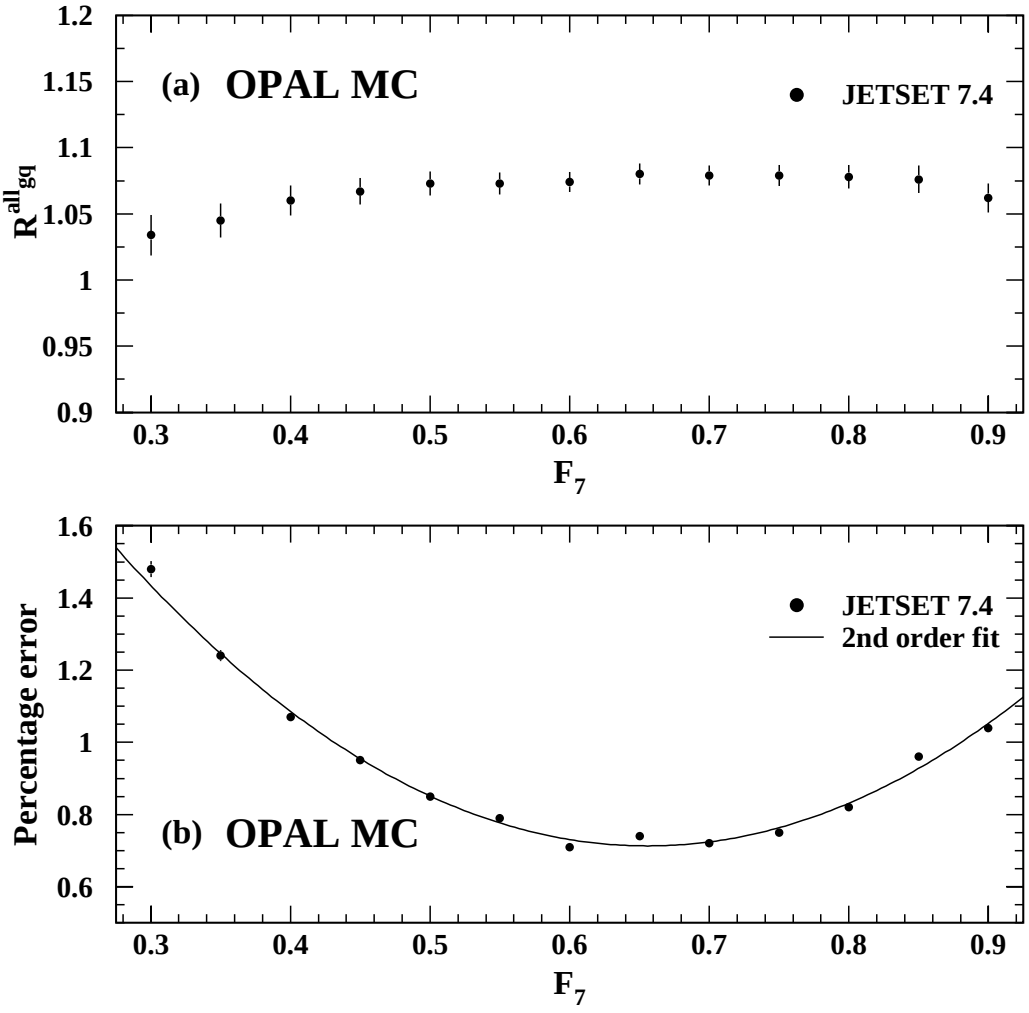

Figure 4.9: (a) Dependence of the ratio of the rate of charged tracks in gluon jets to the rate of charged tracks in quark jets on the value of F_7 chosen to denote the anti-tagged sample. (b) Variation of the percentage error on the ratio with the value of F_7 chosen to denote the anti-tagged sample.

	MC Det. nm	MC Det. atag	MC Det. q	MC Det. g	MC Gen. q	MC Gen. g	Data nm	Data atag
No. tracks	1 475 931	357 438	710 090	765 841	807 963	714 665	801 969	199 082
No. jets	262 115	62 300	134 555	127 560	140 783	106 635	142 245	35 103
$\langle n_{\rm ch}\rangle$/jet	5.631	5.737	5.277	6.004	5.739	6.702	5.638	5.671
Nucl. bkgnd/jet	0.086	0.079	0.085	0.086	0.0	0.0	0.086	0.079
γ conv./jet	0.299	0.295	0.296	0.301	0.0	0.0	0.299	0.295
($\langle n_{\rm ch}\rangle$− bkgnd)	5.246	5.363	4.895	5.617	5.739	6.702	5.253	5.297
No. $\pi^{\pm}$	1 128 559	273 721	538 876	589 683	657 839	589 835	603 190	150 567
$\langle n_{\pi^{\pm}}\rangle$/jet	4.306	4.394	4.005	4.623	4.673	5.531	4.241	4.289
Nucl. bkgnd/jet	0.069	0.060	0.070	0.068	0.00	0.00	0.069	0.060
($\langle n_{\pi^{\pm}}\rangle$− bkgnd)/jet	4.237	4.334	3.935	4.555	4.673	5.531	4.172	4.229
No. $K^{\pm}$	138 573	32 579	71 794	66 779	93 818	70 361	93 409	22 792
$\langle n_{K^{\pm}}\rangle$/jet	0.529	0.523	0.534	0.524	0.666	0.660	0.657	0.649
Nucl. bkgnd/jet	0.003	0.004	0.003	0.003	0.00	0.00	0.003	0.004
($\langle n_{K^{\pm}}\rangle$− bkgnd)/jet	0.526	0.519	0.531	0.521	0.666	0.660	0.654	0.645
No. $p(\bar{p})$	76 068	21 012	28 328	47 740	34 630	46 169	50 166	12 543
$\langle n_{p(\bar{p})}\rangle$/jet	0.290	0.337	0.211	0.374	0.246	0.433	0.353	0.357
Nucl. bkgnd/jet	0.013	0.015	0.011	0.014	0.00	0.00	0.013	0.015
($\langle n_{p(\bar{p})}\rangle$− bkgnd)/jet	0.277	0.322	0.200	0.360	0.246	0.433	0.340	0.342

Table 4.6: Breakdown of results for data and Monte Carlo including background, before the algebraic decomposition, interpolation or detector corrections.

	All	$\pi^{\pm}$	$K^{\pm}$	$p(\overline{p})$
$G^i_{\rm det}$	5.54 $\pm$ 0.02	4.72 $\pm$ 0.02	0.52 $\pm$ 0.01	0.38 $\pm$ 0.01
$Q^i_{\rm det}$	5.10 $\pm$ 0.03	4.37 $\pm$ 0.02	0.55 $\pm$ 0.01	0.20 $\pm$ 0.01
$G^i_{\rm det}/Q^i_{\rm det}$	1.09 $\pm$ 0.01	1.08 $\pm$ 0.01	0.95 $\pm$ 0.03	1.91 $\pm$ 0.11
$G^i_{\rm gen}$	6.70 $\pm$ 0.01	5.53 $\pm$ 0.01	0.66 $\pm$ 0.01	0.43 $\pm$ 0.01
$Q^i_{\rm gen}$	5.74 $\pm$ 0.01	4.67 $\pm$ 0.01	0.67 $\pm$ 0.01	0.25 $\pm$ 0.01
$G^i_{\rm gen}/Q^i_{\rm gen}$	1.17 $\pm$ 0.01	1.18 $\pm$ 0.01	0.99 $\pm$ 0.02	1.72 $\pm$ 0.08

Table 4.7: Ratios of the multiplicities for all species in Monte Carlo, after taking account of nuclear and photon conversion backgrounds, the extrapolation, and performing the algebraic decomposition for the detector level Monte Carlo. All errors are statistical only. The values for the average rates for gluon and quark jets differ from those quoted in Table 4.6 due to the extrapolation and the algebraic decomposition.

4.12 Systematic errors

For each of the systematic errors discussed below, the analysis was repeated with the appropriate changes, to give the particle rates in gluon and quark jets and their ratios. The difference between these values and the results for the standard analysis were taken as systematic errors. The systematic errors were then combined in quadrature to give the overall systematic errors on the particle rates in gluon and quark jets and their ratios. The systematic errors on the ratios are expected to be smaller than those on the particle rates because when the ratio is computed, some of these systematics may cancel. A breakdown of the systematic error on the rates is given in Table 4.9 and a breakdown for the ratios is given in Table 4.10.

The effects of the parameterisation of the Bethe-Bloch equation and the dE/dx resolution were investigated by examining the dE/dx distributions of $\pi^{\pm}$ resulting

	All	$\pi^{\pm}$	$K^{\pm}$	$p(\bar{p})$
G^i	$6.54 \pm 0.05 \pm 0.07$	$5.89 \pm 0.04 \pm 0.17$	$0.75 \pm 0.02 \pm 0.10$	$0.39 \pm 0.03 \pm 0.03$
Q^i	$5.92 \pm 0.06 \pm 0.04$	$5.01 \pm 0.04 \pm 0.12$	$0.78 \pm 0.02 \pm 0.12$	$0.35 \pm 0.02 \pm 0.03$
$\mathcal{R}^i_{gq}$	$1.10 \pm 0.01 \pm 0.02$	$1.17 \pm 0.01 \pm 0.05$	$0.96 \pm 0.03 \pm 0.12$	$1.12 \pm 0.10 \pm 0.11$
$\mathcal{R}^i_{gq}/\mathcal{R}^{\rm all}_{gq}$	-	$1.06 \pm 0.02 \pm 0.05$	$0.87 \pm 0.03 \pm 0.11$	$1.01 \pm 0.09 \pm 0.10$
MC gen $\mathcal{R}^i_{gq}$	1.17 ± 0.01	1.18 ± 0.01	0.99 ± 0.02	1.72 ± 0.08

Table 4.8: Ratios of the multiplicities for all species in data, after all corrections. The generator level predictions are also given. The first errors are statistical, the second are systematic.

from K^0_S decays [68]. The mean, μ_j, and width, σ_j, of the single particle dE/dx distributions were seen to vary by 10% and 3% respectively. The analysis was repeated with these variations and the maximum difference with respect to the standard analysis was taken as a systematic error.

The errors on the parameterisation of the tails of the single particle dE/dx distributions (the Breit-Wigner component) were taken into account by varying the parameters (α_1, α_2 and α_3 in Table 4.3) by their errors. This resulted in a change of typically less than 1% [68] and was not included in the systematic error.

To consider systematic effects associated with the jet tagging, the half-angle of the cone used in the jet tagging procedure was varied from 7° to 8° and the analysis was repeated. To evaluate possible systematics in the jet finding procedure, the parameter ϵ was changed to a value of 10 GeV in the CONE jet finder and the difference seen with respect to the standard analysis was taken as a systematic error.

The systematic error due to the interpolation of each distribution was taken to be the maximum difference observed in the value of the rate returned when (i) the interpolation range was altered by removing the 2 bins on either side of the interpolation region in the standard analysis or (ii) the scaling parameters γ and δ were varied by their errors ($\pm 1\sigma$).

The systematic error due to the extrapolation with Monte Carlo information was taken to be the variation in the rate observed when the prediction of the Monte Carlo-based fit to the data was used instead of the standard Monte Carlo.

The jet purities, ρ_x, were varied by their errors ($\pm 1\sigma$) when the rates were extracted and the maximum difference was taken as a systematic. The errors were derived from a Monte Carlo study with the Monte Carlo divided into subsets. The RMS of the jet purities was used to provide a statistical uncertainty on the jet purities. In addition, there is an ambiguity as to whether a jet is really a gluon or

quark jet [30]. Monte Carlo studies were performed as in [27] and the purity and tag rate determined. Monte Carlo information was used to associate detector level jets with either a gluon or a quark, as in Section 4.8. Monte Carlo studies have shown that the percentage of those jets classified as gluons using this method that are indeed associated with a gluon at the parton level is $\approx 97\%$ [27]. The impurity arises from the case where the highest energy jet is the gluon and leads to double tagged events where both lower energy jets are selected as quark jets (in this case the analysis proceeded as normal and both jets are anti-tagged and therefore analysed so as not to bias the analysis).

As mentioned above, the Monte Carlo predictions for the background rates have an associated error. Each of the background rates was varied independently by its associated error and the resulting differences were taken as systematic errors. It should be noted that the finite Monte Carlo statistics result in statistical uncertainties in the detector corrections, which must be taken into account. Variation of the angular configuration of the three jets and changes in the track and cluster selection criteria have been found to have negligible effects and were not included in the systematic error [27]; variations in the cone size, R, were also investigated and the ratio $\mathcal{R}_{gq}^{\mathrm{all}}$ was found to increase with R [27].

G^i	All	$\pi^{\pm}$	$K^{\pm}$	$p(\overline{p})$
dE/dx	0.00	0.04	0.07	0.01
Jet tag	<0.01	<0.01	0.04	0.01
Jet finding	0.07	0.09	0.01	<0.01
MC Int.	0.00	0.14	0.05	0.02
MC Extr.	0.00	0.01	<0.01	0.00
ρ_g	<0.01	0.02	<0.01	0.01
ρ_{nm}	0.00	<0.01	<0.01	0.00
μ bkgnd	-	0.02	-	-
γ conv.	<0.01	-	-	-
Nucl. int.	<0.01	<0.01	<0.01	<0.01
Total	0.07	0.17	0.10	0.03

Q^i	All	$\pi^{\pm}$	$K^{\pm}$	$p(\overline{p})$
dE/dx	0.00	0.06	0.12	0.01
Jet tag	0.01	0.01	0.01	0.01
Jet finding	0.04	0.09	<0.01	0.01
MC Int.	0.00	0.04	0.04	0.02
MC Extr.	0.00	<0.01	0.00	<0.01
ρ_g	<0.01	0.00	0.01	0.01
ρ_{nm}	<0.01	0.00	<0.01	<0.01
μ bkgnd	-	0.02	-	-
γ conv.	<0.01	-	-	-
Nucl. int.	<0.01	<0.01	<0.01	<0.01
Total	0.04	0.12	0.12	0.03

Table 4.9: The contributions to the systematic error on the identified charged particle production rates in gluon and quark jets.

$\mathcal{R}^i_{gq}$	All	$\pi^\pm$	$K^\pm$	$p(\overline{p})$
dE/dx	0.00	0.01	0.07	0.02
Jet tag	<0.01	<0.01	0.06	0.05
Jet finding	0.02	0.04	0.02	0.03
MC Int.	0.00	0.03	0.09	0.09
MC Extr.	0.00	<0.01	<0.01	<0.01
ρ_g	<0.01	<0.01	<0.01	0.02
ρ_{nm}	0.00	0.00	<0.01	0.01
μ bkgnd	-	<0.01	-	-
γ conv.	0.00	-	-	-
Nucl. int.	0.00	0.00	<0.01	<0.01
Total	0.02	0.05	0.12	0.11

Table 4.10: The contributions to the systematic error on the ratios of the identified charged particle production rates in gluon and quark jets.

4.13 Summary of results

The identified charged particle rates in gluon and quark jets were determined in symmetric 3-jet events in which the two lower energy jets were of approximately equal energy. The fully corrected ratios of identified charged particle production rates in 24.31 GeV gluon and quark jets were found to be

$$\begin{aligned}
\mathcal{R}_{gq}^{\mathrm{all}} &= 1.10 \pm 0.01 \pm 0.02 \\
\mathcal{R}_{gq}^{\pi} &= 1.17 \pm 0.01 \pm 0.05 \\
\mathcal{R}_{gq}^{\mathrm{K}} &= 0.96 \pm 0.03 \pm 0.12 \\
\mathcal{R}_{gq}^{\mathrm{p}} &= 1.12 \pm 0.10 \pm 0.11
\end{aligned}$$

where the first errors are statistical and the second are systematic. JETSET 7.408 Monte Carlo predicts values of 1.17 for all charged tracks, 1.18 for $\pi^{\pm}$, 0.99 for $\mathrm{K}^{\pm}$ and 1.72 for $\mathrm{p}(\overline{\mathrm{p}})$. JETSET underestimates the production rate of $\mathrm{p}(\overline{\mathrm{p}})$ in quark jets compared to the data.

The ratio for all charged particles is consistent with previous analyses, and the ratio for $\mathrm{K}^{\pm}$ is consistent with the previously reported ratio for $\mathrm{K}_{\mathrm{S}}^{0}$. The ratio normalised by the ratio for all charged tracks has also been calculated:

$$\begin{aligned}
\mathcal{R}_{gq}^{\pi}/\mathcal{R}_{gq}^{\mathrm{all}} &= 1.06 \pm 0.02 \pm 0.05 \\
\mathcal{R}_{gq}^{\mathrm{K}}/\mathcal{R}_{gq}^{\mathrm{all}} &= 0.87 \pm 0.03 \pm 0.11 \\
\mathcal{R}_{gq}^{\mathrm{p}}/\mathcal{R}_{gq}^{\mathrm{all}} &= 1.01 \pm 0.09 \pm 0.10
\end{aligned}$$

The predictions for JETSET were found to be in good agreement with the data, with the exception of $\mathrm{p}(\overline{\mathrm{p}})$. The data values for $\pi^{\pm}$, $\mathrm{K}^{\pm}$ and $\mathrm{p}(\overline{\mathrm{p}})$ are consistent with values reported previously.

Chapter 5

Charged Particle Momentum Spectra at LEPII

In the summer of 1996, LEP entered a new phase of operations for an e^+e^- collider when it commenced operations at a centre of mass energy, $\sqrt{s}$, of 161 GeV. The LEPII programme continued at a higher centre of mass energy of 172 GeV towards the end of the 1996 run and then 183 GeV in the summer of 1997.

These new higher centre of mass energies presented not only new technical problems for the accelerator and its detectors, but a radically different physical environment, leading to new considerations for any data analysis. In the LEPII programme, initial state radiation plays a significant role in a large fraction of the events observed and hadronic W^+W^- decays form a background to the hadronic Z^0 decays under investigation.

In this chapter, charged particle momentum spectra from the process $e^+e^- \rightarrow (Z^0/\gamma)^* \rightarrow q\overline{q}$ are presented for the three centre of mass energies of 161 GeV, 172 GeV and 183 GeV. These charged particle momentum spectra allow tests of QCD at LEPII energies. The charged particle fragmentation function, $1/\sigma_{\rm had}\ {\rm d}\sigma/{\rm d}x_p$, and the $\xi_p = \ln(1/x_p)$ distribution, $1/\sigma_{\rm had}\ {\rm d}\sigma/{\rm d}\xi_p$, where $x_p = 2p/\sqrt{s}$, are constructed

from the momentum of the charged track, p. The integral of the x_p distribution yields the average charged particle multiplicity, $n_{\rm ch}$. The peak of the ξ_p distribution, ξ_0, is predicted by QCD. The rapidity distribution relative to the thrust axis, $y = |\ln \frac{E+p_\parallel}{E-p_\parallel}|$, and the distributions of track momentum components parallel, $p_\perp^{\rm in}$, and perpendicular, $p_\perp^{\rm out}$, to the event plane also allow tests of QCD.

5.1 Charged particle momentum spectra at 161 GeV

In the initial stage of the LEPII programme, e^+e^- beams were collided at $\sqrt{s} = 161.33 \pm 0.05$ GeV [76]. This lies just above the threshold for W^+W^- boson pair production. The cross section for this process rises above threshold, as shown in Figure 5.1, and the $W^+W^- \rightarrow q\overline{q}q\overline{q}$ decay channel shares many characteristics with the $e^+e^- \rightarrow (Z^0/\gamma)^* \rightarrow q\overline{q}$ channel. As mentioned above, the majority of hadronic $(Z^0/\gamma)^*$ events are radiative returns to the Z^0 pole where a high energy initial state photon is emitted (Figure 5.2). This initial state radiation, or ISR, reduces the effective centre of mass energy, $\sqrt{s'}$, below that of the nominal $\sqrt{s}$. These two processes constitute the main background to the signal channel which is $e^+e^- \rightarrow (Z^0/\gamma)^* \rightarrow q\overline{q}$ with less than 1 GeV of ISR. In Figure 5.3, the difference between the true centre of mass energy, $\sqrt{s}$, and $\sqrt{s'}$ is shown for hadronic events in the 161 GeV data. Monte Carlo predictions for the expected contribution from events with four-fermion final states ($e^+e^- \rightarrow f\overline{f}f\overline{f}$ events, including those Feynman diagrams with W^+W^- bosons), W^+W^- events alone, and radiative $(Z^0/\gamma)^*$ events, defined as those $(Z^0/\gamma)^*$ events with greater than 1 GeV of initial state radiation are also shown. The radiative returns to the Z^0 may be seen as the peak at $\sqrt{s} - \sqrt{s'} \approx 70$ GeV.

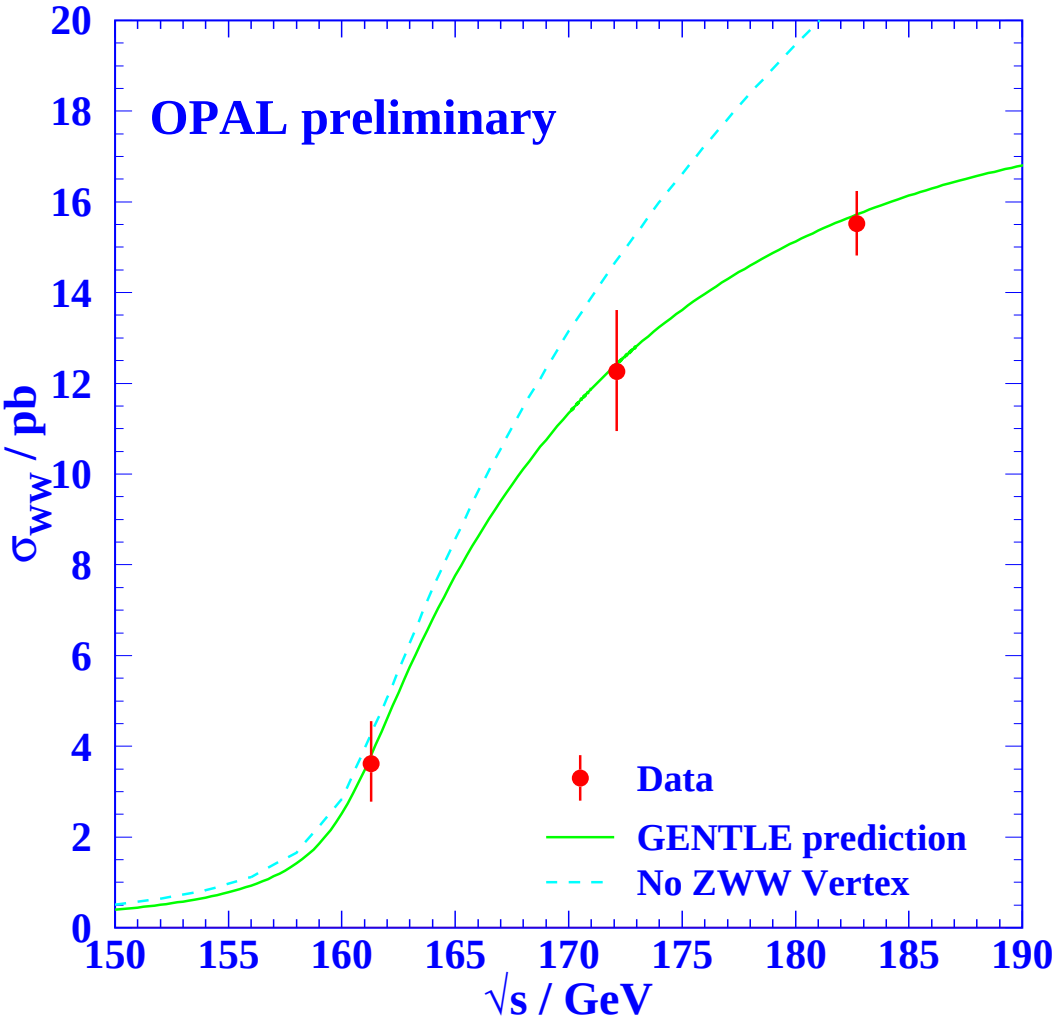

Figure 5.1: The dependence of $\sigma_{W^+W^-}$ on $\sqrt{s}$, as predicted by GENTLE semi-analytic program [77] for M_W= 80.35 GeV with OPAL data for 161, 172 and 183 GeV. The dashed curve shows the expected cross section if there is no Z^0 W^+W^- coupling (from [78]).

5.1.1 The 161 GeV analysis

The data in this analysis corresponds to an integrated luminosity of $\mathcal{L}$ = 10.00 $\pm$ 0.04 $\pm$ 0.04 pb^{-1} at a centre of mass energy $\sqrt{s}$ = 161.3 GeV. The PYTHIA

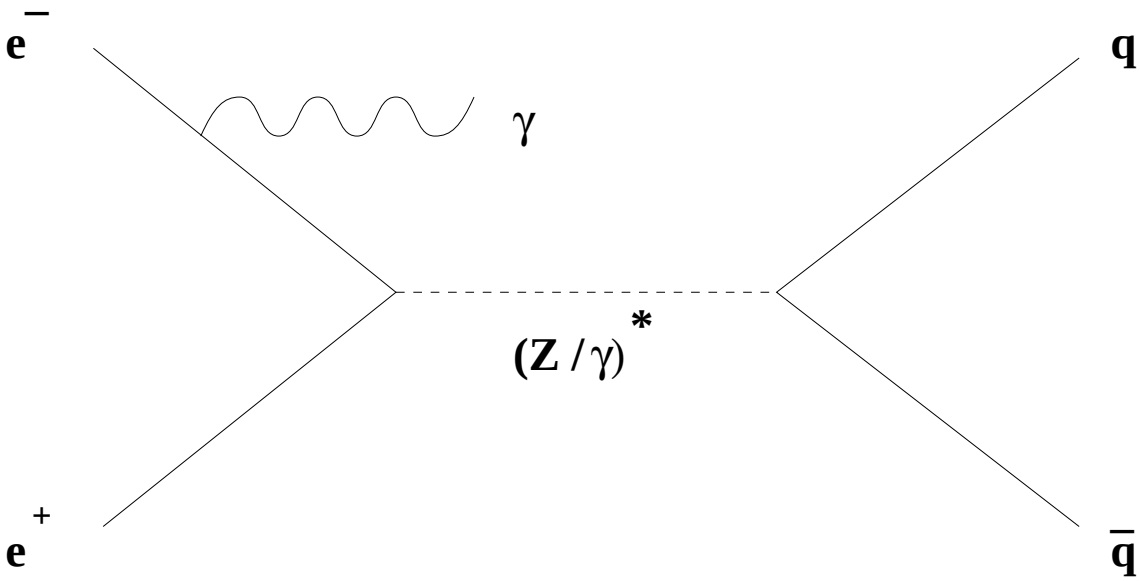

Figure 5.2: Feynman diagram for the process $e^+e^- \rightarrow Z^0/\gamma^* \rightarrow q\bar{q}$ with initial state radiation at $\sqrt{s} = 161$ GeV.

5.722 [28], HERWIG 5.8d [34], ARIADNE 4.08 [35] and COJETS 6.23 [36] QCD based Monte Carlo generators were compared to the data. The PYTHIA 5.722 parton shower Monte Carlo, with initial and final state radiation, and fragmentation handled by JETSET 7.408 [28] was used for detector simulation. As an alternative, HERWIG 5.8d parton shower Monte Carlo at 161.0 GeV was used. The grc4f 1.2 Monte Carlo [37] was used for four-fermion background simulation. This background consists of events of the type $e^+e^- \rightarrow (Z^0/\gamma)^* \rightarrow f\bar{f}f\bar{f}$ with quark or leptonic final states, produced by s channel or t channel processes (where possible), including W^+W^- events but excluding those processes with Feynman diagrams with intermediate gluons. As a cross check in the systematic checks, the EXCALIBUR Monte Carlo [38] was used for the four-fermion background. In the discussion that follows, the backgrounds have been normalised to the observed data luminosity.

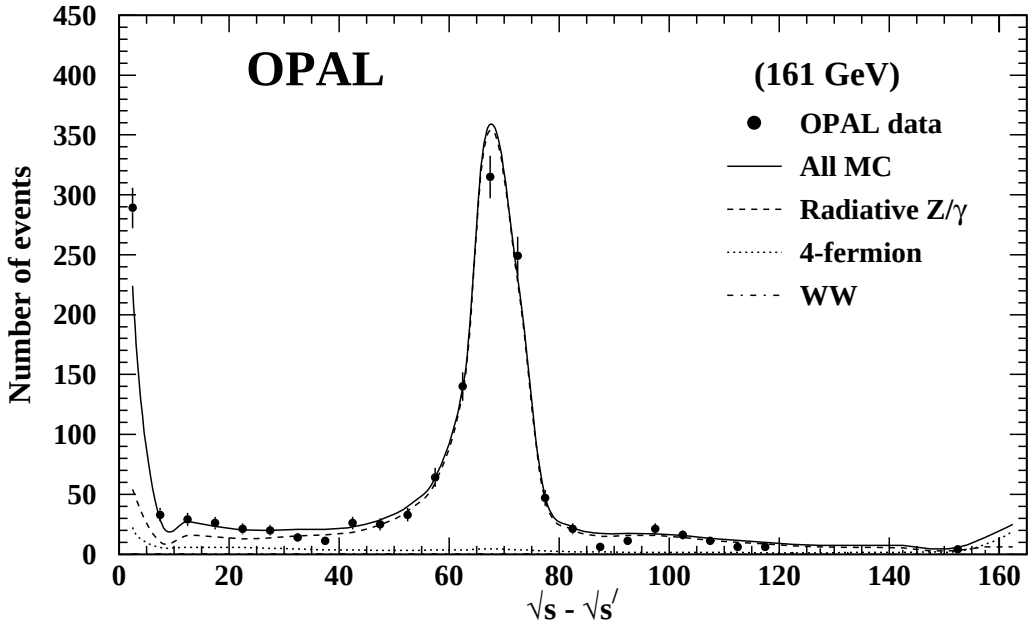

Figure 5.3: The $\sqrt{s}$ - $\sqrt{s'}$ distribution for 161 GeV. The Monte Carlo predictions for four-fermion processes, W^+W^- pairs and radiative $(Z^0/\gamma)^*$ events are also shown.

5.1.2 Event selection

The background at 161 GeV falls broadly into two categories: the radiative returns to the Z^0 pole that have a reduced $\sqrt{s'}$ and those events originating from four-fermion processes, including W^+W^- pair production events. An example of a Feynman diagram for a four-fermion event is shown in Figure 5.4 and examples of W^+W^- production are shown in Figure 5.5. Signal events are defined to be hadronic decays of a $(Z^0/\gamma)^*$ with less than 1 GeV of initial state radiation.

To enhance the fraction of signal events in the sample, a series of cuts were applied to the data sample. Events were only selected as good hadronic events if they passed the standard OPAL multihadron preselection which relies on the

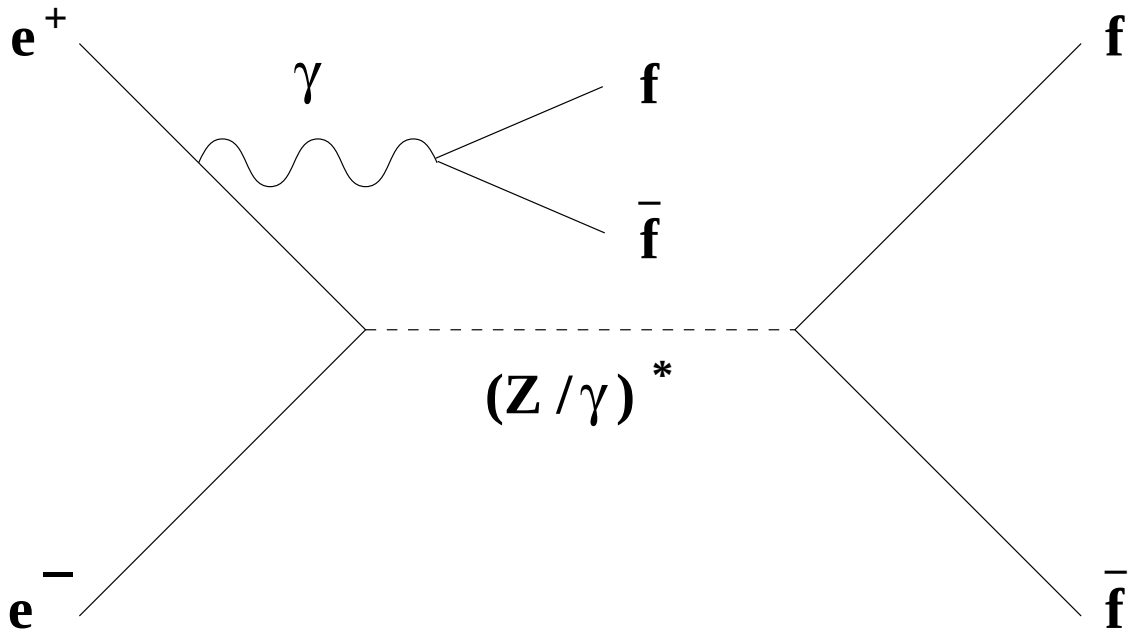

Figure 5.4: Feynman diagram for four-fermion production at LEPII, through the conversion of an initial state photon.

identification of good quality tracks and clusters in the OPAL detector [26,27].

To eliminate leptonic events at these higher energies, a more stringent selection of at least 7 good charged tracks per event was made. In addition, to ensure that the event was well contained within the detector, the cosine of polar angle of the thrust axis was constrained to lie in the region $|\cos\theta_T| \leq 0.9$.

Further selection was then used to enhance the fraction of hadronic events with less than 1 GeV of initial state radiation. To reject events with high initial state radiation, a kinematic fit was performed on the event [79], using the DURHAM jet finder [74] to reconstruct exactly 4 jets with a jet resolution parameter, $y_{cut} = 0.02$, then the jet energy was reconstructed using tracking and calorimetry information. A search in the detector for one or two clusters consistent with initial state photons was performed. If no photons were found, then the energy and momentum balance was used for the postulate of a photon travelling along the beam pipe. By using

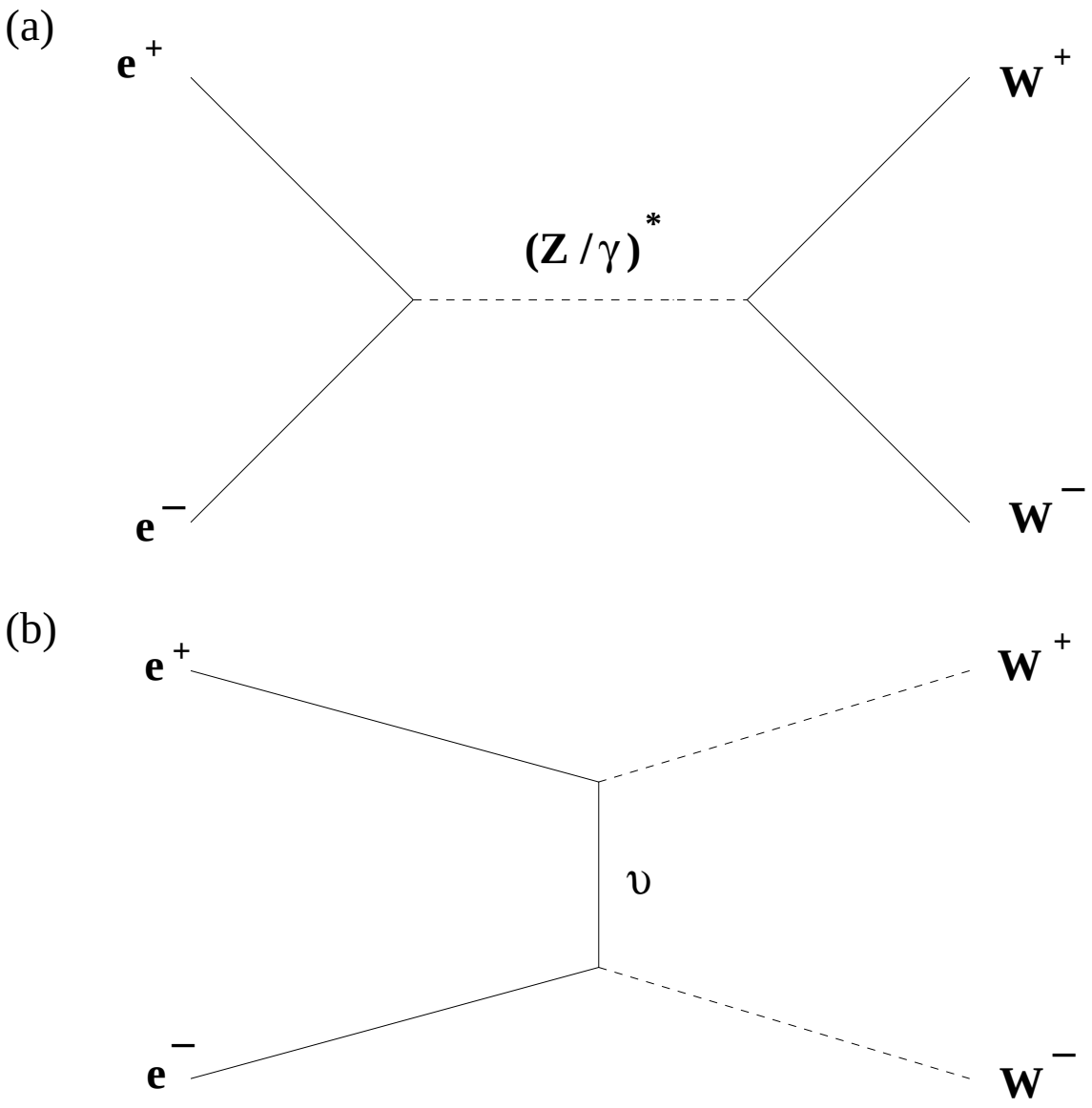

Figure 5.5: Feynman diagrams for the production of W^+W^-pairs at LEPII, from (a) $(Z^\circ/\gamma)^*$ decay or (b) via neutrino exchange.

the constraint of energy and momentum conservation, this fit returned the effective centre of mass energy, $\sqrt{s'}$. Events satisfying $\sqrt{s}$ - $\sqrt{s'}$ < 10 GeV were selected. These selection criteria selected a total of 307 data events. The distribution of the difference between $\sqrt{s}$ and $\sqrt{s'}$ is shown in Figure 5.3 for the data and the Monte Carlo.

This gave an efficiency (obtained from Monte Carlo studies) of 82% and an expected background of 7% of which 5.3% is estimated to arise from W^+W^- events (for the 161 GeV data luminosity, this corresponds to 21 four-fermion events, of which 16 are W^+W^- events). The expected contribution from $e^+e^- \rightarrow \tau^+\tau^-$ and $\gamma\gamma \rightarrow q\bar{q}$ events was less than 0.3% and was neglected.

5.1.3 Backgrounds and corrections

The four-fermion background remaining after the selection criteria described above was subtracted from the data using the grc4f Monte Carlo. The data were then unfolded to generator level using multiplicative correction factors derived from PYTHIA Monte Carlo. The correction factors are the ratio of the generator level Monte Carlo to the detector level Monte Carlo for each bin of the charged particle momentum spectra. These correction factors account for detector resolution and acceptance effects.

To estimate systematic effects, the analysis was repeated with the containment cut reduced to $|\cos\theta_T| \leq 0.7$, and with an alternative energy balance fit for the missing momentum instead of the $\sqrt{s'}$ kinematic fit [80]. In addition, the DURHAM jet finder was used to reconstruct four jets and a fit to the mass of di-jet pairs was performed. Any events that produced a fitted di-jet mass > 72 GeV/c^2 were rejected as possible W^+W^- events. This resulted in an efficiency of 68% and a background of 3%, which was then subtracted using Monte Carlo information. The use of this cut introduced a slight bias into the analysis. The maximum allowed impact parameter, $|d_0|$, was varied from 2 cm to 5 cm, to examine any effects of track selection. To take account of any systematic effects in the choice of hadronisation model, the analysis was repeated using the HERWIG Monte Carlo for the correction factors. To allow for any systematic error in the background, EXCALIBUR replaced grc4f as the background Monte Carlo and the difference was taken as a systematic. The

sum in quadrature of all of these (after the correction for statistical effects described below) was taken as the total systematic error.

Given the small statistics which were present in this analysis, it is possible that a systematic change could introduce a large fluctuation in the number of entries in a bin. Such a change is more properly classified as a statistical error, since it may not be present in a higher statistics analysis. To investigate the possible statistical contribution to systematic effects, 30 subsets of the PYTHIA Monte Carlo at detector level containing the same number of events as the data (after preselection cuts were applied) were analysed individually as data and unfolded using the remaining subsets [31]. The variation of the contents in each bin for each distribution was noted for the 30 subsets and the RMS of the variation was calculated. The systematic error quoted is

- $\sqrt{(\sigma_{syst}^2 - RMS^2)}$ for $\sigma_{syst} > RMS$
- 0 for $\sigma_{syst} < RMS$

where σ_{syst} is the error before the correction was applied.

This may result in bin to bin fluctuations in the systematic error, but avoids overestimating the systematic error. A breakdown of the contributions to the systematic error is given in Table 5.1 for the ξ_0 and $n_{\rm ch}$ measurements.

5.1.4 Results at 161 GeV

Charged particle momentum spectra have been studied at $\sqrt{s}$ = 161 GeV, 172 GeV and 183 GeV. In particular, the components of momentum parallel, $p_\perp^{\rm in}$, and perpendicular, $p_\perp^{\rm out}$, to the event plane, the rapidity with respect to the thrust axis, y, the fragmentation function, or x_p distribution, and the $\xi_p = \ln(1/x_p)$ distribution have been investigated. The momentum spectra exhibit similar behaviour at all

three centre of mass energies. The spectra are only shown for $\sqrt{s} = 183$ GeV, since that is the highest energy and the largest data sample.

For 161 GeV, the integration of the fragmentation function yields

$$\langle n_{\rm ch} \rangle (161 \text{ GeV}) = 24.25 \pm 0.43(\text{stat.}) \pm 0.55(\text{syst.}). \quad (5.1)$$

as the charged multiplicity. This is consistent with the value obtained from the rapidity distribution. The COJETS Monte Carlo predicts a value for $n_{\rm ch}$ of 28.3, which is 6σ above the measured value. PYTHIA and ARIADNE predict 25.9 and HERWIG predicts 25.5, which are about 2σ above the measured value.

A Next to Leading Log Approximation (NLLA) fit to the peak of the ξ_p distribution may be performed with a Gaussian with higher moments (skewed Gaussian). The peak position has been extracted and was found to be

$$\xi_0(161 \text{ GeV}) = 4.00 \pm 0.03(\text{stat.}) \pm 0.02(\text{syst.}). \quad (5.2)$$

5.2 Charged particle momentum spectra at 172 GeV

In the later part of the 1996 run, the LEPII programme advanced to e^+e^- collisions at 172 GeV. This energy lies above the W^+W^- pair production threshold; the W^+W^- cross-section rises steeply above threshold (see Figure 5.1) and so the potential background from W^+W^- events increases from 161 to 172 GeV. Initial state radiation still affects the majority of events, as mentioned above. The data referred to below correspond to a luminosity of $\mathcal{L} = 10.42 \pm 0.06$ pb^{-1}, collected at a mean energy of 172.1 GeV [32]. The PYTHIA, HERWIG, ARIADNE and COJETS Monte Carlos are again compared with the data. In the case of the 172 GeV analysis, HERWIG 5.9 was used instead of HERWIG 5.8d. All of the Monte

	ξ_0	$n_{\rm ch}$
Standard result	4.00	24.25
Stat. error	0.03	0.43
Energy Balance	< 0.01	-0.52
$\lvert d_0 \rvert < 5$ cm	< 0.01	$+0.03$
$\lvert \cos\theta_T \rvert < 0.7$	-0.01	< 0.01
$M_{\rm W}^{fit}$	$+0.02$	< 0.01
HERWIG	-0.01	-0.16
EXCALIBUR	< 0.01	-0.04
Total syst. error	0.02	0.55

Table 5.1: Values of the standard result and error breakdown for ξ_0 and $n_{\rm ch}$ for 161 GeV. The signs indicate the direction of the change in the result for each systematic check relative to the standard analysis.

Carlo event samples were generated at a centre of mass energy of 171.0 GeV. This difference in centre of mass energies has a negligible effect on the analysis. In the discussion which follows, the backgrounds have been normalised to the observed data luminosity.

5.2.1 Event selection

The event selection proceeded as for 161 GeV (see Section 5.1.2), except that, as mentioned above, the $\rm W^+W^-$ background had increased significantly. After the standard selection of good hadronic events, 7 good charged tracks, $\lvert \cos\theta_T \rvert < 0.9$ and the use of the kinematic fit to require $\sqrt{s}$ - $\sqrt{s'} < 10$ GeV, 273 data events were selected. According to Monte Carlo studies, the efficiency of this selection procedure was 81% and the estimated four-fermion background was 19% (the estimated

W^+W^- background was 17.7%). For this reason, an additional cut was imposed to reduce the background to a level similar to that at 161 GeV, so that a simple background subtraction could be performed. It should be noted that in the case of the 172 GeV analysis, the kinematic fit returned a $\sqrt{s'}$ that was considered with respect to $\sqrt{s}$ = 172 GeV and not 161 GeV. Figure 5.6 indicates the data distribution for the difference between $\sqrt{s}$ and $\sqrt{s'}$ and the Monte Carlo predictions for all processes, radiative $(Z^0/\gamma)^*$ events, the four-fermion background alone, and W^+W^- events only. As was the case at $\sqrt{s}$ = 161 GeV, the expected contribution from $e^+e^- \rightarrow \tau^+\tau^-$ and $\gamma\gamma \rightarrow q\bar{q}$ events was negligible and was neglected.

Among possible cuts considered to reduce the background level were a cut on the fitted di-jet mass as was used at 161 GeV as a systematic check, or a cut on y_{34}, the value of y_{cut} from the DURHAM jet scheme where the number of resolved jets changes from three to four. Both of these cuts would have introduced a heavy bias into the analysis. Instead, the QCD matrix element $W_{\rm QCD}$ was constructed from the momenta of the event using the EVENT2 program [81]. In the systematic checks, a change of this cut was used instead of the fit returning the di-jet masses.

The QCD matrix element tests the compatibility of the events with QCD-like production processes. The tree level, $\mathcal{O}(\alpha_s^2)$ [82], matrix element $|\mathcal{M}|^2$ for the processes $e^+e^- \rightarrow q\bar{q}q\bar{q}, q\bar{q}gg$ was calculated by forcing the events to a four-jet configuration, using the DURHAM scheme. Then

$$W_{\rm QCD} = \max_{\{p_1,p_2,p_3,p_4\}} \log\left(|\mathcal{M}(p_1,p_2,p_3,p_4)|^2\right) \tag{5.3}$$

where p_i is the momenta of the reconstructed jets. Since neither quark nor gluon identification was performed, the matrix element was calculated for each permutation of the jet-momenta and the permutation with the largest value for the matrix element was used to define $W_{\rm QCD}$.

$W_{\rm QCD}$ is expected to have large values for processes described by the QCD matrix element, originating from $(Z^0/\gamma)^* \rightarrow q\overline{q}$, and smaller values for W^+W^- events.

In Figure 5.6(b) the data distribution of $W_{\rm QCD}$ for events passing all cuts up to and including the kinematic fit are compared to the predictions of Monte Carlo simulations for four-fermion processes (including $\rm W^+W^-$ events) and all expected events ($(\rm Z^0/\gamma)^*$ and four-fermion predictions combined). A separation between the $(\rm Z^0/\gamma)^*$ and four-fermion events is achieved by demanding $W_{\rm QCD} \geq -0.5$.

After this requirement, the event sample consisted of a total of 229 hadronic events. The estimated four-fermion background was reduced from 19% of the data sample to 7% whilst the total efficiency for signal $(\rm Z^0/\gamma)^*$ events (less than 1 GeV of ISR) was reduced from 81% to 78%. The expected four-fermion background was then subtracted using the grc4f Monte Carlo.

The analysis then proceeded as for the 161 GeV data, with correction factors for detector resolution and acceptance effects, computed by considering the ratio of the generator and detector level distributions as in Section 5.1.3. The systematic checks of using the energy balance to find $\sqrt{s'}$, the variation of $|d_0|$ from 2 to 5 cm, requiring $|\cos\theta_T| < 0.7$ and the use of HERWIG to calculate the detector corrections were repeated. However, the cut on $W_{\rm QCD}$ was altered in the systematic checks instead of a cut on the di-jet mass; here, the cut on $W_{\rm QCD}$ was altered to 0.0 or -0.8, which corresponded to a variation of 50% in the four-fermion background. The maximum variation seen was taken as a systematic error. The use of EXCALIBUR as an alternative four-fermion Monte Carlo at $\sqrt{s} = 172$ GeV resulted in a negligible difference for the results and was not included in the systematic error. The statistical component of the systematic checks was then evaluated, as described in Section 5.1.3, and the systematic error was corrected. The corrected systematic errors were combined in quadrature to give the total systematic error.

5.2.2 Results from 172 GeV

The momentum spectra for the 172 GeV data are similar to those for the 183 GeV data and are not shown. For the 172 GeV data, an integration of the fragmentation function yields the charged multiplicity,

$$\langle n_{\rm ch} \rangle (172 \text{ GeV}) = 25.48 \pm 0.56(\text{stat.}) \pm 0.58(\text{syst.}). \tag{5.4}$$

The predicted Monte Carlo values for $n_{\rm ch}$ are 26.6 for PYTHIA, 26.5 for ARIADNE, 26.3 for HERWIG and 29.2 for COJETS, which is more than 3σ higher than the observed value.

An NLLA fit to the ξ_p distribution was performed as at 161 GeV. The peak of this skewed Gaussian is

$$\xi_0(172 \text{ GeV}) = 4.02 \pm 0.04(\text{stat.}) \pm 0.02(\text{syst.}). \tag{5.5}$$

where the systematic error includes a component due to a variation of the fit range which was not included at 161 GeV. The lower edge of the fit range was varied by plus or minus two bins, with the upper edge fixed, and then the upper edge of the fit range was varied in the same way, with the lower edge held fixed. The systematic error was taken to be half of the maximum difference between the values of the peak returned by these four fits. A full breakdown of the systematic errors for both ξ_p and $n_{\rm ch}$ are given in Table 5.2.

	ξ_0	n_{ch}
Standard result	4.02	25.48
Stat. error	0.04	0.56
Energy Balance	+0.01	+0.37
$\lvert d_0 \rvert <$ 5 cm	< 0.01	+0.18
$\lvert \cos\theta_T \rvert < 0.7$	< 0.01	< 0.01
W_{QCD}	+0.01	+0.22
HERWIG	+0.01	−0.35
NLLA Fit range	< 0.01	-
Total syst. error	0.02	0.58

Table 5.2: Values of the standard result and error breakdown for ξ_0 and n_{ch} for 172 GeV. The signs indicate the direction of the change in the result for each systematic check relative to the standard analysis. The NLLA fit range only applies for the ξ_0 measurement.

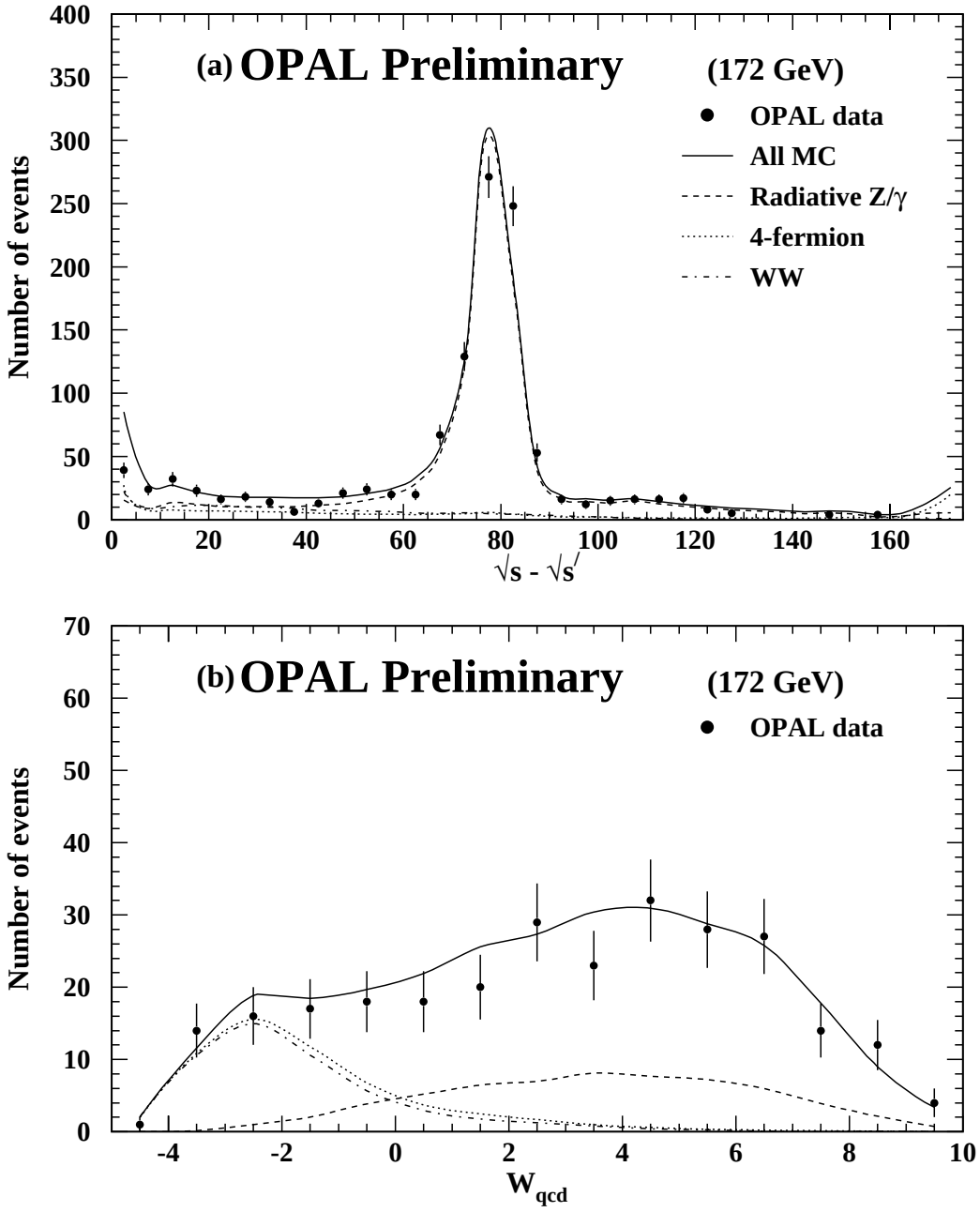

Figure 5.6: (a) The $\sqrt{s}$ - $\sqrt{s'}$ distribution for 172 GeV. The Monte Carlo predictions for 4-fermion processes, W^+W^- pairs and radiative $(Z^0/\gamma)^*$ events are also shown. (b) The $W_{\rm QCD}$ distribution for 172 GeV for events passing all cuts prior to $W_{\rm QCD}$ cut, with Monte Carlo predictions.

5.3 Charged particle momentum spectra at 183 GeV

LEP produced e^+e^- collisions at $\sqrt{s} = 183$ GeV in the summer of 1997. At this energy, the centre of mass energy is above the threshold for Z^0Z^0 pair production. In addition, the W^+W^- cross section continues to rise, but not as rapidly as from 161 to 172 GeV (see Figure 5.1). Initial state radiation still dominates over these two effects, as may be seen from Figure 5.7(a), where the difference between $\sqrt{s}$ and $\sqrt{s'}$ is shown for the data, all Monte Carlo processes and the four-fermion background (including W^+W^- events). The 183 GeV sample corresponds to an integrated luminosity of $\mathcal{L} = 55.22 \pm 0.02$ pb^{-1} [33], recorded at a centre of mass energy of 182.6 ± 0.03 GeV [83]. The backgrounds have been normalised to this luminosity.

5.3.1 The 183 GeV analysis and event selection

The analysis proceeded as did the 172 GeV analysis, using the PYTHIA 5.722, HERWIG 5.9, COJETS 6.23 and ARIADNE 4.08 event generators and the grc4f 2.0 Monte Carlo for the four-fermion background, including W^+W^- and Z^0Z^0 pairs. However, in this case, the effects from the statistical contributions of the systematic checks were negligible due to the higher statistics. The EXCALIBUR generator was considered as an alternative for the simulation of the four-fermion background, but this had a negligible effect on the results.

The standard selection cuts were used, as for the 161 and 172 GeV data, resulting in a data sample of 1345 events. Monte Carlo studies indicated that the expected four-fermion background was 27% of this sample, the W^+W^- background was 25% and the Z^0Z^0 background was 1.4%. The efficiency for selection of signal $Z^0/\gamma^* \rightarrow q\bar{q}$ events with less than 1 GeV of initial state radiation was 84%. As was the case for

the two previous analyses, $e^+e^- \to \tau^+\tau^-$ and $\gamma\gamma \to q\bar{q}$ events had a negligible effect.

To remove the W^+W^- background from the sample, the QCD matrix element W_{QCD}, as defined in Section 5.2.1, was considered. Figure 5.7(b) shows the separation possible using W_{QCD}. In addition to the values of W_{QCD} for the data, the Monte Carlo predictions for all processes passing the selection criteria up to and including the kinematic fit are shown, together with the expected four-fermion background and W^+W^- background. Applying the cut $W_{QCD} \geq -0.5$ reduced the number of selected data events to 1026, with a selection efficiency of 80% but the expected four-fermion background was reduced to 9% (0.5% Z^0Z^0 background). The expected four-fermion background, including W^+W^- and Z^0Z^0 processes, was then subtracted using Monte Carlo information.

The analysis then proceeded as previously, with the correction for detector resolution and acceptance effects, through correction factors calculated by comparing the generator level and detector level charged particle momentum spectra (see Section 5.1.3). The systematic checks of the use of the energy balance method to find $\sqrt{s'}$, the variation of $|d_0|$ from 2 to 5 cm, requiring $|\cos\theta_T| < 0.7$, the use of HERWIG to calculate the detector corrections and altering W_{QCD} to 0.0 or -0.8 and taking the maximum variation were then applied. Because of the higher statistics of the 183 GeV data sample, the statistical component of the systematic effects was negligible, and was ignored. The systematic errors from the sources above were combined in quadrature to give the total systematic error.

5.3.2 Results from 183 GeV

Charged particle momentum spectra at 183 GeV were constructed from the charged tracks of selected events. The momentum spectra for the components of momentum parallel, $p_\perp^{in}$, and perpendicular, $p_\perp^{out}$, to the event plane are shown in Figure 5.8. The predictions of PYTHIA, HERWIG, COJETS and ARIADNE Monte Carlo models

are also shown. The full error bars on the data points represent the statistical and systematic errors combined in quadrature, whilst the tick marks on the error bars indicate statistical errors only. COJETS does not model the slope of the components of momentum parallel and perpendicular to the event plane well. The COJETS $p_\perp^{\rm in}$ distribution is steeper than the data and COJETS overestimates the intermediate region of $p_\perp^{\rm out}$.

The rapidity with respect to the thrust axis, y, and the fragmentation function, the $1/\sigma_{\rm had}\,{\rm d}\sigma/{\rm d}x_p$ distribution, where $x_p = 2p/\sqrt{s}$, are shown in Figure 5.9. There is some evidence that the data shows a plateau at low rapidity. All of the Monte Carlo models except COJETS agree with the data. COJETS overestimates the production of charged particles at low rapidity and has a higher charged multiplicity than is observed in the data. Even if the difference in charged multiplicity is taken into account, COJETS does not describe the rapidity distribution well. The integration of the fragmention function yields the charged multiplicity,

$$\langle n_{\rm ch}\rangle(183\ {\rm GeV}) = 26.44 \pm 0.20({\rm stat.}) \pm 0.45({\rm syst.}) \qquad (5.6)$$

The predicted values for $n_{\rm ch}$ from Monte Carlo are 27.4 (PYTHIA), 27.3 (ARIADNE), 27.0 (HERWIG) which are all within 2σ of the measured value. COJETS predicts an $n_{\rm ch}$ of 30.2, which is over 7σ above the measured value.

The $1/\sigma_{\rm had}\,{\rm d}\sigma/{\rm d}\xi_p$ distribution, where $\xi_p = \ln(1/x_p)$, is shown in Figure 5.10(a) together with the Monte Carlo predictions. The ARIADNE prediction is indistinguishable from PYTHIA and is omitted for reasons of clarity. Whilst PYTHIA and HERWIG describe the data well, COJETS overestimates soft charged particle production and also in the region of the peak.

In addition to the Monte Carlo predictions, a prediction using the Modified Leading Log Approximation (MLLA) [84] is shown as a shaded band. In the Modified Leading Log Approximation, the most complete calculation available, the ξ_p distri-

bution is predicted in terms of two parameters, a QCD scale Λ and a normalisation factor $K(\sqrt{s})$ associated with the Local Parton Hadron Duality hypothesis [41]. The energy dependence of $K(\sqrt{s})$ is weak, but previous measurements of $K(\sqrt{s})$ [85] are consistent with a linear dependence on the centre of mass energy, $\sqrt{s}$.

The values of Λ and $K(M_{Z^0})$ have been determined from a fit of the MLLA prediction to the ξ_p distribution at $\sqrt{s} = 91.2$ GeV [85]. Figure 5.10(a) shows the MLLA prediction at $\sqrt{s} = 183$ GeV, using the value of Λ determined at $\sqrt{s} = 91.2$ GeV [85]. The upper edge of the shaded band corresponds to $K(183\ \text{GeV}) = K(M_{Z^0}) = 1.28$ whilst the lower edge corresponds to $K(183\ \text{GeV}) = 1.12$, which is the value obtained by extrapolating the value of $K(M_{Z^0})$ to $\sqrt{s} = 183$ GeV, assuming a linear centre of mass energy dependence.

The description of the data is relatively good around the region of the peak for the extrapolated value of $K(183\ \text{GeV})$ considering that there are no free parameters. The MLLA prediction is quite similar to the predictions of PYTHIA and HERWIG, except at large ξ_p where kinematic effects become important, and where perturbative QCD calculations are no longer valid. The NLLA fit of a skewed Gaussian to this distribution is also shown in Figure 5.10(a). The fit range is shown by the extent of the NLLA curve. This skewed Gaussian yields the peak,

$$\xi_0(183\ \text{GeV}) = 4.08 \pm 0.01(\text{stat.}) \pm 0.03(\text{syst.}) \tag{5.7}$$

where the systematic error includes a component due to the fit range. A full breakdown of the systematic error is given in Table 5.3.

In Figure 5.10(b) the energy evolution of the peak is shown together with the lower energy data [31,32,79,86] and an MLLA fit up to and including the 172 GeV data which is then extrapolated to 183 GeV. The extrapolation predicts a value of $\xi_0 = 4.04 \pm 0.01$ for the peak position at 183 GeV, which is consistent with this measurement. A double log approximation (DLA) fit, which does not include terms

	ξ_0	$n_{\rm ch}$
Standard result	4.08	25.48
Stat. error	0.01	0.20
Energy Balance	$+0.02$	-0.17
$\lvert d_0\rvert < 5$ cm	-0.01	-0.03
$\lvert\cos\theta_T\rvert < 0.7$	< 0.01	$+0.16$
$W_{\rm QCD}$	-0.01	-0.17
HERWIG	-0.01	-0.35
NLLA Fit range	0.01	-
Total syst. error	0.03	0.45

Table 5.3: Values of the standard result and error breakdown for ξ_0 and $n_{\rm ch}$ for 183 GeV. The signs indicate the direction of the change in the result for each systematic check relative to the standard analysis. The NLLA fit range only applies for the ξ_0 measurement.

due to coherent gluon emission, is also presented and is not in agreement with the data. The MLLA fit is dominated by two low energy data points with small errors, which effectively fix the single parameter which controls the intercept and gradient of the fit. To remove the dependence of the fit on the two lower energy data points at 29 and 35 GeV those points have been de-weighted in the fit shown in Figure 5.10(b), to give the LEPI and LEPII data points a higher weight. This results in the fit moving closer to the LEP data points. For the two results in question, the quoted errors were smaller than or similar to the combined LEPI results from all four LEPI experiments. Following consultation with OPAL colleagues who were involved in these low energy experiments, the errors on those points were set equal to the error on the $\sqrt{s} = 44$ GeV result, to minimise any possible under-estimation of the systematic error.

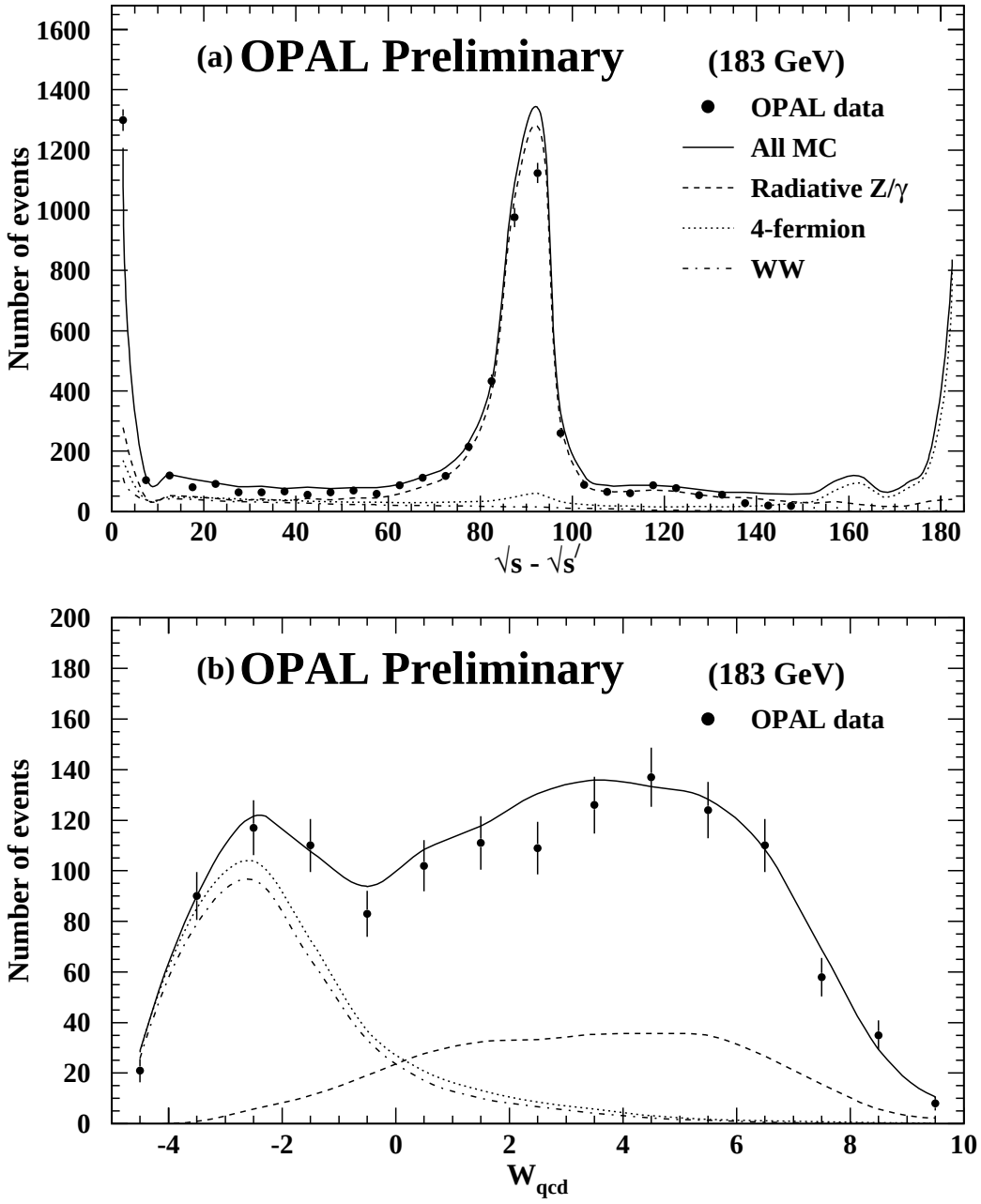

Figure 5.7: (a) The $\sqrt{s}$ - $\sqrt{s'}$ distribution for 183 GeV. The Monte Carlo predictions for 4-fermion processes, W^+W^- pairs and radiative $(Z^0/\gamma)^*$ events are also shown. (b) The $W_{\rm QCD}$ distribution for 183 GeV for events passing all cuts prior to $W_{\rm QCD}$ cut, with Monte Carlo predictions.

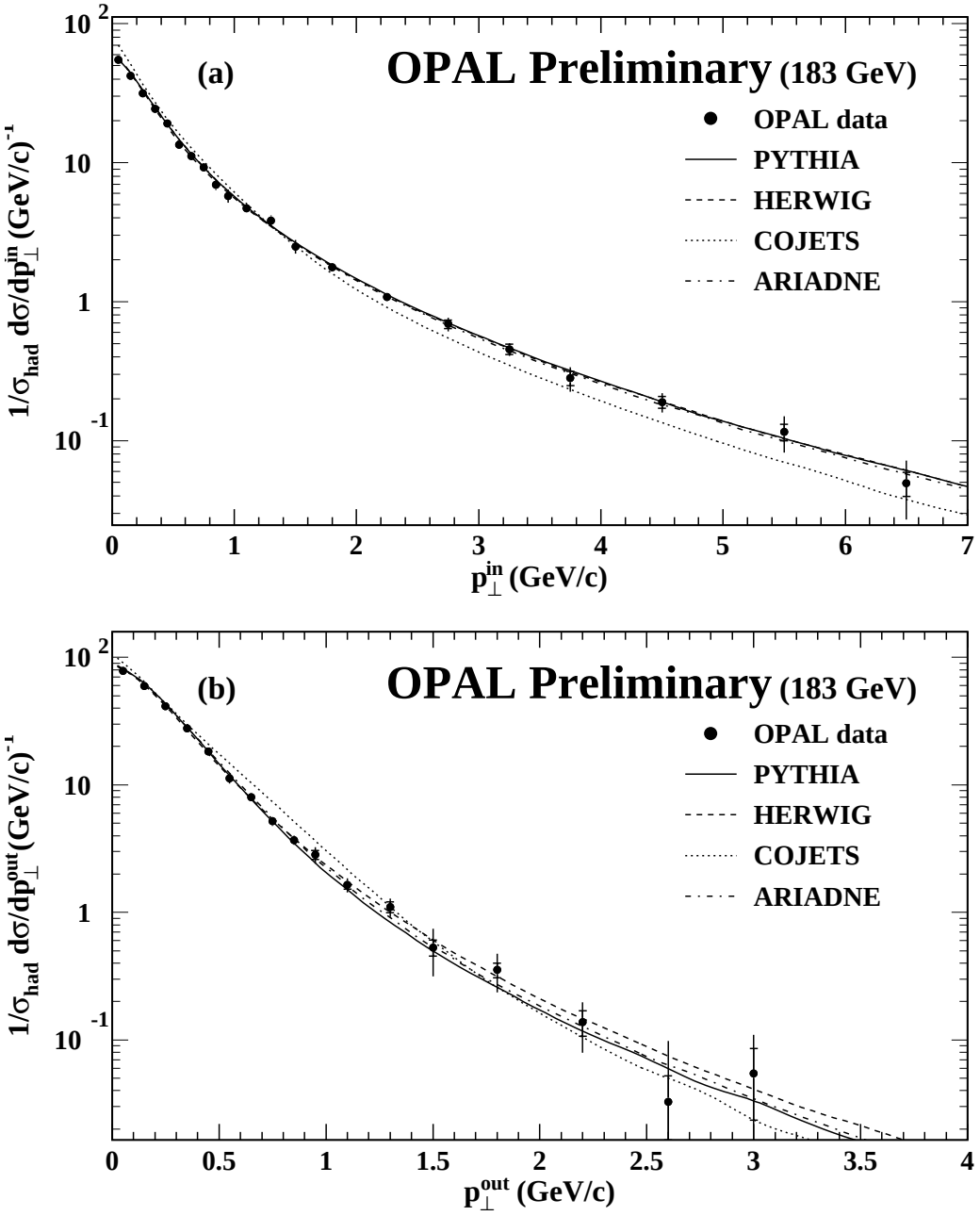

Figure 5.8: Distributions of momentum spectra in, $p_\perp^{\rm in}$, and out, $p_\perp^{\rm out}$, of the event plane for charged particles at $\sqrt{s}$ = 183 GeV, compared to PYTHIA, HERWIG, COJETS and ARIADNE.

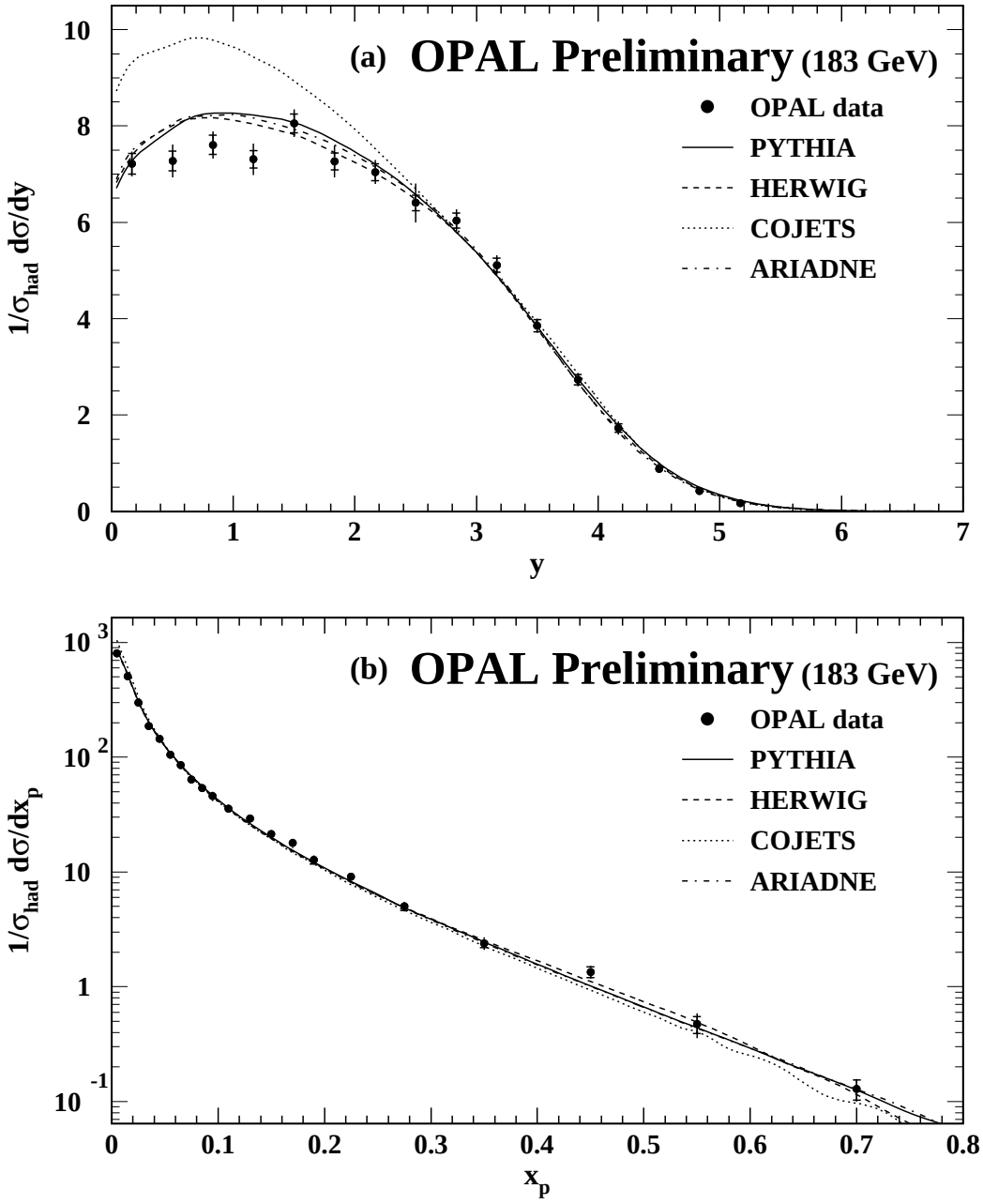

Figure 5.9: Distribution of Rapidity, y, and the fragmentation function for charged particles at $\sqrt{s} = 183$ GeV, compared to PYTHIA, HERWIG, COJETS and ARIADNE predictions.

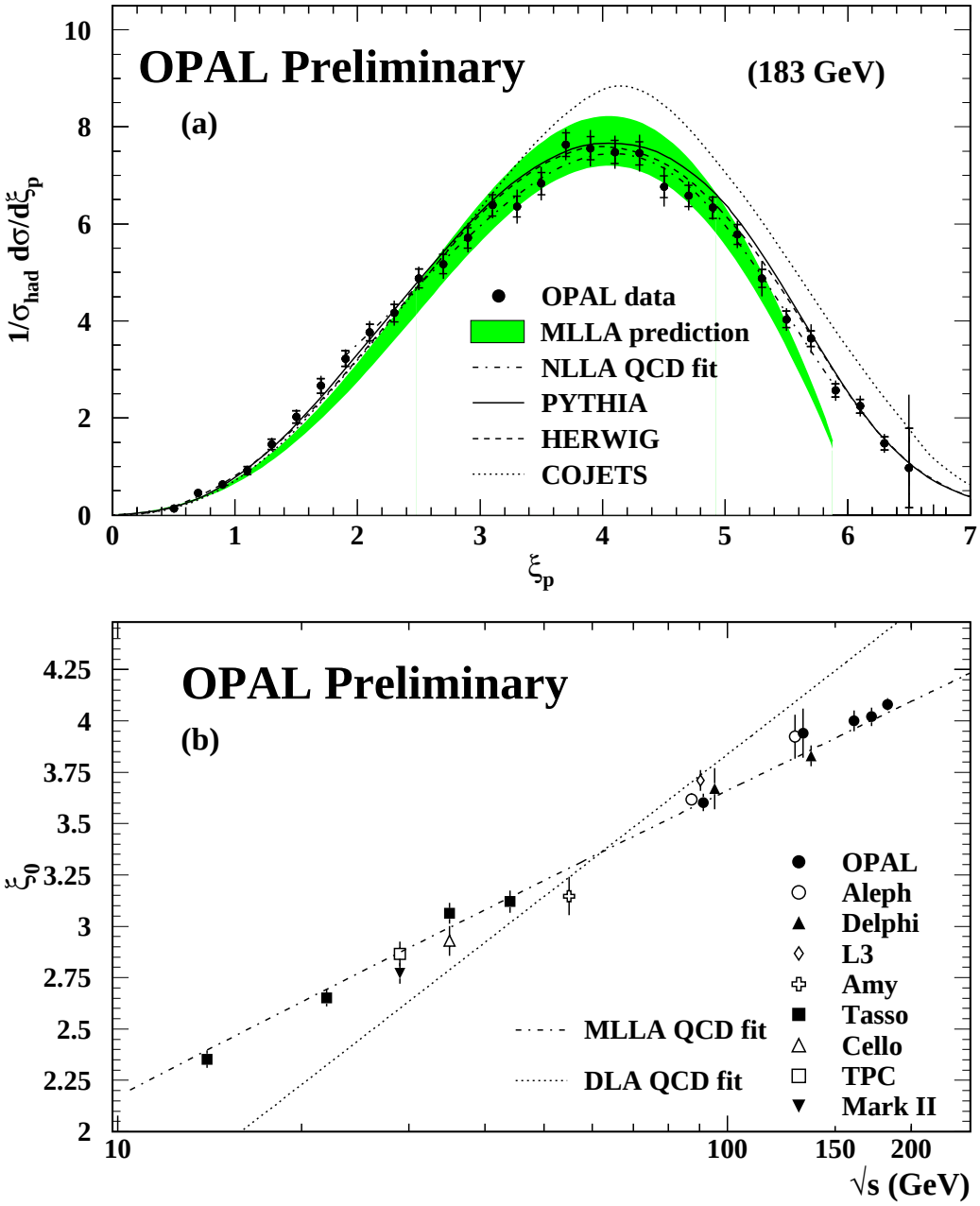

Figure 5.10: (a) Distribution of $\xi_p = \ln(1/x_p)$ for charged particles at 183 GeV. Also shown are a fit of the NLLA QCD prediction, and the MLLA QCD, PYTHIA, HERWIG and COJETS predictions. (b) Evolution of the position of the peak of the ξ_p distribution, ξ_0, with c.m. energy $\sqrt{s}$, compared with a fit of the MLLA and DLA QCD predictions up to and including the data at 172 GeV.

5.4 LEPII results: a summary

The LEPII programme has produced a wide range of centre of mass energies for e^+e^- collisions, from 161 to 183 GeV. The analysis presented here is a self-consistent treatment of these energies and offers a common framework in which to view the results as part of the study of QCD by the OPAL QCD Working Group. Charged particle momentum spectra have been investiagted at 161, 172 and 183 GeV, and show similar behaviour at all three centre of mass energies. The QCD-based event generators PYTHIA, HERWIG and ARIADNE are in good overall agrement with the data, but tend to have slightly higher multiplicites. The COJETS generator overestimates the production of charged particles at low rapidity and at high and intermediate values of ξ_p, where soft particles are produced and destructive gluon interference occurs. The MLLA prediction for the evolution of the peak position of the ξ_p distribution is in broad agreement with the data. The DLA prediction is excluded by the data, indicating the importance of colour coherence effects.

The $n_{\rm ch}$ and ξ_0 values at LEPII were found to be

$$\begin{aligned}
\langle n_{\rm ch}\rangle(161\ {\rm GeV}) &= 24.25 \pm 0.43 \pm 0.55 \\
\langle n_{\rm ch}\rangle(172\ {\rm GeV}) &= 25.48 \pm 0.56 \pm 0.58 \\
\langle n_{\rm ch}\rangle(183\ {\rm GeV}) &= 26.44 \pm 0.20 \pm 0.45
\end{aligned}$$

$$\begin{aligned}
\xi_0(161\ {\rm GeV}) &= 4.00 \pm 0.03 \pm 0.02 \\
\xi_0(172\ {\rm GeV}) &= 4.02 \pm 0.04 \pm 0.02 \\
\xi_0(183\ {\rm GeV}) &= 4.08 \pm 0.01 \pm 0.02
\end{aligned}$$

where the first errors are statistical and the second are systematic. The predictions from Monte Carlo and analytic calculations were found to be in good overall agreement with the data, with the exception of COJETS. This is thought to be because COJETS does not implement coherent gluon emission (colour coherence),

which can lead to destructive interference in soft particle production, thereby lowering the multiplicity and altering the shape of the momentum spectra.

Chapter 6

Summary

This thesis has described two analyses of hadronic Z^0 events observed in the OPAL detector at LEP. In the first analysis, planar three-jet hadronic events in which the two lowest energy jets were of approximately equal energy were selected from the LEPI data. The highest energy jet is expected to be a quark 97% of the time; thus particle production in gluon and quark jets of equal energy can be studied using these events. A tag based on the energy profile of the jet was used to anti-tag gluon jets and a gluon jet enhanced sample was compared with the inclusive lower energy jet sample. The tracks in each sample were analysed using an extended maximum likelihood fit to $\mathrm{d}E/\mathrm{d}x$ information to extract the identified charged particle rates for the two samples. A process of algebraic decomposition was used to find the rates for pure gluon and quark jets. The fully corrected ratios of identified charged particle production rates in 24.31 GeV gluon and quark jets were found to be

$$\begin{aligned}
\mathcal{R}_{gq}^{\mathrm{all}} &= 1.10 \pm 0.01 \pm 0.02 \\
\mathcal{R}_{gq}^{\pi} &= 1.17 \pm 0.01 \pm 0.05 \\
\mathcal{R}_{gq}^{\mathrm{K}} &= 0.96 \pm 0.03 \pm 0.12 \\
\mathcal{R}_{gq}^{\mathrm{p}} &= 1.12 \pm 0.10 \pm 0.11
\end{aligned}$$

where the first errors are statistical and the second are systematic. These results may be compared with the predicted JETSET 7.4 values of 1.17 for all charged tracks, 1.18 for $\pi^{\pm}$, 0.99 for $K^{\pm}$ and 1.72 for $p(\overline{p})$.

The JETSET predictions, with the exception of the $p(\overline{p})$ rate in quark jets, are in good agreement with the data. The difference in the $p(\overline{p})$ rate in quark jets accounts for the difference in $\mathcal{R}^{p}_{gq}$. The results reported here for the ratios of identified charged particle rates in gluon and quark jets agree well with previous results for all charged particles.

The ratios have also been normalised to the ratio for all charged tracks:

$$\begin{aligned}
\mathcal{R}^{\pi}_{gq}/\mathcal{R}^{\mathrm{all}}_{gq} &= 1.06 \pm 0.02 \pm 0.05 \\
\mathcal{R}^{K}_{gq}/\mathcal{R}^{\mathrm{all}}_{gq} &= 0.87 \pm 0.03 \pm 0.11 \\
\mathcal{R}^{p}_{gq}/\mathcal{R}^{\mathrm{all}}_{gq} &= 1.01 \pm 0.09 \pm 0.10
\end{aligned}$$

The JETSET predictions agree well with these values, with the exception of that for $p(\overline{p})$. The data values for $\pi^{\pm}$, $K^{\pm}$ and $p(\overline{p})$ are consistent with the values reported in [68] in a jet energy-ordering analysis. It should be noted that the jet energy-ordering method utilises far higher statistics; this accounts for the smaller errors. The jet energy-ordering analysis does not, in general, use jets of equal energies, so topology and jet energy considerations become important.

In the second analysis, the properties of charged particle momentum spectra have been investigated in hadronic events at LEPII. Data from runs at $\sqrt{s} = 161$, 172 and 183 GeV were analysed. The charged particle momentum spectra show similar behaviour at all three centre of mass energies. The charged multiplicity, n_{ch}, and the peak of the ξ_p distribution, ξ_0, were found and their values at LEPII were found to be

$$\langle n_{\rm ch}\rangle(161\ {\rm GeV}) = 24.25 \pm 0.43 \pm 0.55$$
$$\langle n_{\rm ch}\rangle(172\ {\rm GeV}) = 25.48 \pm 0.56 \pm 0.58$$
$$\langle n_{\rm ch}\rangle(183\ {\rm GeV}) = 26.44 \pm 0.20 \pm 0.45$$

$$\xi_0(161\ {\rm GeV}) = 4.00 \pm 0.03 \pm 0.02$$
$$\xi_0(172\ {\rm GeV}) = 4.02 \pm 0.04 \pm 0.02$$
$$\xi_0(183\ {\rm GeV}) = 4.08 \pm 0.01 \pm 0.02$$

The predictions from Monte Carlo simulations and analytic calculations were found to be in good overall agreement with the data, apart from the Monte Carlo models predicting slightly higher multiplicities than observed in the data. The COJETS Monte Carlo overestimates the production of charged particles at low rapidity and at high and intermediate values of ξ_p. This is thought to be because COJETS does not implement coherent gluon emission, which can lead to destructive interference in soft particle production, thereby lowering the multiplicity and altering the shape of the momentum spectra. The MLLA prediction for the energy evolution of the peak position of the ξ_p distribution is in broad agreement with the data whilst the DLA prediction is excluded, again indicating the importance of colour coherence.

Appendix A

Extended Maximum Likelihood

In situations where the number of events (or tracks in this case) is not fixed, or where the size and shape of the distribution function may have an impact on the likelihood, it may be more appropriate to use the method of extended maximum likelihood than the more usual maximum likelihood. A detailed account of the derivation, properties and use of the extended maximum likelihood method is given in [72]. A brief description may be found below.

A.1 Maximum likelihood

In the method of maximum likelihood, the likelihood function for the estimate of the particle rates $\underline{a} = (a_\pi, a_K, a_p, a_e)$ is

$$\mathcal{L} = \prod_{i=1}^{N} R((\mathrm{d}E/\mathrm{d}x)_i; \underline{a}) \tag{A.1}$$

where $R(\mathrm{d}E/\mathrm{d}x; \underline{a})$ is the probability density for the sampling variable $\mathrm{d}E/\mathrm{d}x$ and N is the number of observed tracks. In the case of the fit to $\mathrm{d}E/\mathrm{d}x$ information, for a maximum likelihood fit, R may be defined as

$$R((\mathrm{d}E/\mathrm{d}x)_i, \underline{a}) = \frac{1}{\nu} \sum_{j=\pi,K,p,e} a_j P_j((\mathrm{d}E/\mathrm{d}x)_i; \mu_j(p_i), \sigma_j, \underline{\alpha}) \tag{A.2}$$

where P_j is the single particle $\mathrm{d}E/\mathrm{d}x$ distribution for particle species j and is normalised to unity, μ_j is the expected mean $\mathrm{d}E/\mathrm{d}x$ measurement for species j, σ_j is the width of the distribution, p_i is the track momentum and the total number of expected tracks is given by $\nu = \sum_{j=\pi,K,p,e} a_j$ as in Section 4.5. The parameters $\underline{\alpha}$ determine the contribution of the tail, parameterised by a Breit-Wigner. Since any measurement of $\mathrm{d}E/\mathrm{d}x$ must return a value, the probability density is normalised to unity:

$$\int R(\mathrm{d}E/\mathrm{d}x;\underline{a})\mathrm{d}(\mathrm{d}E/\mathrm{d}x) = 1 \tag{A.3}$$

If this condition is relaxed and the normalisation is allowed to vary, then we find ourselves using an extended maximum likelihood fit. In the extended maximum likelihood, $R((\mathrm{d}E/\mathrm{d}x)_i;\underline{a})$ is replaced by $Q((\mathrm{d}E/\mathrm{d}x)_i;\underline{a})$ where

$$\int Q(\mathrm{d}E/\mathrm{d}x;\underline{a})\mathrm{d}(\mathrm{d}E/\mathrm{d}x) = \nu(\underline{a}) \tag{A.4}$$

and ν is the number of tracks that we expect to observe over the whole $\mathrm{d}E/\mathrm{d}x$ range (so $\int Q(\mathrm{d}E/\mathrm{d}x;\underline{a})\mathrm{d}(\mathrm{d}E/\mathrm{d}x) = \nu \int R(\mathrm{d}E/\mathrm{d}x;\underline{a})\mathrm{d}(\mathrm{d}E/\mathrm{d}x)$, which justifies Equation 4.2). The Q describes both the shape and the size of the $\mathrm{d}E/\mathrm{d}x$ distribution. $Q\delta(\mathrm{d}E/\mathrm{d}x)$ is the number of tracks in the range $\mathrm{d}E/\mathrm{d}x$ to $\mathrm{d}E/\mathrm{d}x + \delta(\mathrm{d}E/\mathrm{d}x)$.

For the fit to $\mathrm{d}E/\mathrm{d}x$ information, a maximum likelihood fit with four parameters, a_π, a_K, a_p and ν could be used, since ν would describe the size and shape of the distribution. This would return the same answers as the extended maximum likelihood fit in this case [87]. However, the extended maximum likelihood fit treats all four particle species in a symmetric way and is more convenient to use.

In general the extended maximum likelihood method should be used when the number of tracks (events in the general case) is not fixed or known beforehand or is subject to random (Poisson) fluctuations or if the expected value depends on the parameters being estimated [72].

A.2 Extended maximum likelihood

In the method of extended maximum likelihood, the likelihood function, $\mathcal{L}$, for the data $(\mathrm{d}E/\mathrm{d}x)_1, \ldots, (\mathrm{d}E/\mathrm{d}x)_N$ must incorporate the information that the tracks have been observed to have $\mathrm{d}E/\mathrm{d}x$ values $(\mathrm{d}E/\mathrm{d}x)_1, \ldots, (\mathrm{d}E/\mathrm{d}x)_N$ and the fact that the total number of tracks observed is N. The derivation of the likelihood function can be presented in two ways.

A.2.1 Orear's argument

Following Orear [88], let us divide the variable $\mathrm{d}E/\mathrm{d}x$ into bins of width $\Delta\mathrm{d}E/\mathrm{d}x$ such that the probability of a single bin containing more than one track is negligible. Then, by Poisson statistics the probability of a bin containing zero tracks is:

$$P_0(\mathrm{d}E/\mathrm{d}x;\underline{a}) = e^{-\Delta\mathrm{d}E/\mathrm{d}x\ Q(\mathrm{d}E/\mathrm{d}x;\underline{a})} \tag{A.5}$$

and for a bin containing a single track it is

$$P_1(\mathrm{d}E/\mathrm{d}x;\underline{a}) = \Delta\mathrm{d}E/\mathrm{d}x\ Q(\mathrm{d}E/\mathrm{d}x;\underline{a})e^{-\Delta\mathrm{d}E/\mathrm{d}x\ Q(\mathrm{d}E/\mathrm{d}x;\underline{a})} \tag{A.6}$$

where $Q(\mathrm{d}E/\mathrm{d}x;\underline{a})$ is the probability density for the system. The extended likelihood can then be written as :

$$\mathcal{L} = \prod_i \Delta\mathrm{d}E/\mathrm{d}x\ Q((\mathrm{d}E/\mathrm{d}x)_i;\underline{a}) \prod_k e^{-\Delta\mathrm{d}E/\mathrm{d}x\ Q((\mathrm{d}E/\mathrm{d}x)_k;\underline{a})} \tag{A.7}$$

where the product over i is over all bins containing an event (in our case this becomes over all tracks) and the product over k is over all bins. As $\Delta\mathrm{d}E/\mathrm{d}x \to \mathrm{d}(\mathrm{d}E/\mathrm{d}x)$ then

$$\prod_i \Delta\mathrm{d}E/\mathrm{d}x\ Q((\mathrm{d}E/\mathrm{d}x)_i;\underline{a}) \to \mathrm{d}^N(\mathrm{d}E/\mathrm{d}x) \prod_i Q((\mathrm{d}E/\mathrm{d}x)_i;\underline{a}) \tag{A.8}$$

and

$$\prod_k e^{-\Delta\mathrm{d}E/\mathrm{d}x\ Q((\mathrm{d}E/\mathrm{d}x)_k;\underline{a})} \to e^{-\sum_k \Delta\mathrm{d}E/\mathrm{d}x\ Q((\mathrm{d}E/\mathrm{d}x)_k;\underline{a})} \to e^{-\int Q(\mathrm{d}E/\mathrm{d}x;\underline{a})\mathrm{d}(\mathrm{d}E/\mathrm{d}x)} = e^{-\nu} \tag{A.9}$$

Dropping the $\mathrm{d}^N(\mathrm{d}E/\mathrm{d}x)$, we can then write the likelihood function as

$$\mathcal{L} = \left[\prod_{i=1}^{N} Q((\mathrm{d}E/\mathrm{d}x)_i; \underline{a})\right] e^{-\nu} \tag{A.10}$$

Hence the function that we actually minimise is:

$$-\ln(\mathcal{L}) = -\sum_{i=1}^{N} \ln Q((\mathrm{d}E/\mathrm{d}x)_i; \underline{a}) + \nu \tag{A.11}$$

A.2.2 Alternative derivation

A simpler derivation is to state that if a particular Q predicts a total number of tracks ν and the actual number of tracks observed is N, then this can be incorporated into the likelihood by the addition of a factor reflecting the probability of observing N tracks if the mean is ν, using Poisson statistics. So the total probability of a sample is then

$$\mathcal{L} = \left[\prod_{i=1}^{N} R((\mathrm{d}E/\mathrm{d}x)_i; \underline{a})\right] e^{-\nu} \frac{\nu^N}{N!} \tag{A.12}$$

where $R((\mathrm{d}E/\mathrm{d}x)_i; \underline{a})$ is the standard maximum likelihood probability density. Now, as $\int Q(\mathrm{d}E/\mathrm{d}x; \underline{a})\mathrm{d}(\mathrm{d}E/\mathrm{d}x) = \nu \int R(\mathrm{d}E/\mathrm{d}x; \underline{a})\mathrm{d}(\mathrm{d}E/\mathrm{d}x)$, the likelihood function may be written as

$$\mathcal{L} = \left[\prod_{i=1}^{N} Q((\mathrm{d}E/\mathrm{d}x)_i; \underline{a})\right] \frac{e^{-\nu}}{N!} \tag{A.13}$$

and since the term in $N!$ is a constant and does not affect the minimisation process, this yields

$$-\ln(\mathcal{L}) = -\sum_{i=1}^{N} \ln Q((\mathrm{d}E/\mathrm{d}x)_i; \underline{a}) + \nu \tag{A.14}$$

as the function to be minimised, as above in equation A.11, and as in equation 4.6.

Bibliography

[1] S. Myers, CERN Report 91-08 (1991)

[2] K. Ahmet et al., OPAL Collaboration, Nucl. Instrum. Meth. A 305 (1991) 275

[3] P. P. Allport et al., Nucl. Instrum. Meth. A 346 (1994) 476
P. P. Allport et al., Nucl. Instrum. Meth. A 324 (1993) 34

[4] J. R. Carter et al., Nucl. Instrum. Meth. A 286 (1990) 99

[5] M. Hauschild et al., Nucl. Instrum. Meth. A 314 (1992) 74

[6] M. Hauschild, Nucl. Instrum. Meth. A 379 (1996) 436

[7] H. Mes et al., Nucl. Instrum. Meth. A 265 (1988) 445

[8] D. Jeanne et al., Nucl. Instrum. Meth. 111 (1973) 287

[9] R. M. Sternheimer and R. F. Peierls, Phys. Rev. B3 (1971) 3681

[10] M. Akrawy et al., Nucl. Instrum. Meth. A 290 (1990) 76

[11] OPAL Collaboration, Internal Note TN 524 (1997)

[12] An Ji-Gang et al., Nucl. Instrum. Meth. A 267 (1988) 386
An Ji-Gang et al., Nucl. Instrum. Meth. A 267 (1988) 396

[13] C. Beard et al., Nucl. Instrum. Meth. A 286 (1990) 117

[14] G. Bella et al., Nucl. Instrum. Meth. A 252 (1986) 503
S. Dado et al., Nucl. Instrum. Meth. A 252 (1986) 511
G. Mikenberg, Nucl. Instrum. Meth. A 265 (1988) 223

[15] R. J. Akers et al., Nucl. Instrum. Meth. A 357 (1995) 253

[16] G. T. J. Arnison et al., Nucl. Instrum. Meth. A 294 (1990) 431

[17] The SiW Group, OPAL Collaboration, Internal Note TN 528 (1997)

[18] D. C. Imrie et al., Nucl. Instrum. Meth. A 283 (1989) 515
B. E. Anderson et al., Nucl. Instrum. Meth. A 283 (1989) 650

[19] B. E. Anderson et al., IEEE Trans. Nucl. Sci. 41 (1994) 845

[20] M. Arignon et al., Nucl. Instrum. Meth. A 313 (1992) 103

[21] M. Arignon et al., Nucl. Instrum. Meth. A 333 (1993) 330

[22] D. G. Charlton et al., Nucl. Instrum. Meth. A 325 (1993) 129

[23] C. Hawkes et al., OPAL Collaboration, Internal Note OPAL-Offline note 16/OFFL-0487 (1996)

[24] J. Allison et al., Nucl. Instrum. Meth. A 317 (1992) 47

[25] R. Brun et al., CERN Report DD/EE/84-1 (1984)

[26] G. Alexander et al., OPAL Collaboration, Zeit. f. Physik C 52 (1991) 175

[27] R. Akers et al., OPAL Collaboration, Zeit. f. Physik C 68 (1995) 179

[28] T. Sjöstrand, Comput. Phys. Commun. 82 (1994) 74

[29] M. Z. Akrawy et al., OPAL Collaboration, Zeit. f. Physik C 47 (1990) 505

[30] G. Alexander et al., OPAL Collaboration, Zeit. f. Physik C 69 (1996) 543

[31] K. Ackerstaff et al., OPAL Collaboration, Zeit. f. Physik C 75 (1997) 193

[32] OPAL Collaboration, Internal Note PN 281 (1997)

[33] OPAL Collaboration, Internal Note PN 323 (1997)

[34] G. Marchesini et al., Comput. Phys. Commun. 67 (1992) 465

[35] L. Lönnblad, Comput. Phys. Commun. 71 (1992) 15

[36] R. Odorico, Comput. Phys. Commun. 72 (1992) 238
P. Mazzanti and R. Odorico, Nucl. Phys. B 394 (1993) 267

[37] J. Fujimoto et al., Comput. Phys. Commun. 100 (1997) 128

[38] F. A. Berends, R. Pittau and R. Kleiss, Comput. Phys. Commun. 85 (1995) 437

[39] see, for example, F. Halzen and A. D. Martin, Quarks and Leptons, John Wiley and Sons (1984).
I. J. R. Aitchison and A. J. G. Hey, Gauge Theories in Particle Physics, IOP Publishing (1989)

[40] S. L. Glashow, Nucl. Phys. 22 (1961) 579.
S. Weinberg, Phys. Rev. Lett. 19 (1967) 1264.
A. Salam in Proceedings of the 8th Nobel symposium, p 367, ed. N. Svartholm. Almqvist and Wiskell, Stockholm (1968),
reprinted in Selected Papers of Abdus Salam, p 244, ed. A. Ali, C. Isham, T. Kibble and Riazuddin (1994).
C. Itzykson and J-B. Zuber, Quantum Field Theory, McGraw-Hill (1980)

[41] Ya. I. Azimov, Yu. L. Dokshitzer, V. A. Khoze and S. I. Troyan, Phys. Lett. B 165 (1985) 147 and Zeit. f. Physik C 27 (1985) 65

[42] R. K. Ellis, W. J. Stirling and B. R. Webber, QCD and Collider Physics, Cambridge University Press (1996)

[43] Yu. L. Dokshitzer, V. A. Khoze, A. H. Mueller and S. I. Troyan, Basics of Peturbative QCD, Editions Frontières (1991)

[44] Yu. L. Dokshitzer et. al., in Perturbative Quantum Chromodynamics, ed. A. H. Mueller, World Scientific (1989)

[45] Yu. L. Dokshitzer, V. A. Khoze, S. I. Troyan and A. H. Mueller, Rev. Mod. Phys. 60 (1988) 373

[46] I. G. Knowles and G. D. Lafferty, J. Phys. G: Nucl. Part. Phys. 23 (1997) 731

[47] R. D. Field and R. P. Feynman, Phys. Rev. D 15 (1977) 2590

[48] A. Kryzwicki and B. Petersson, Phys. Rev. D 6 (1972) 924
J. Finkelstein and R. D. Peccei, Phys. Rev. D 6 (1972) 2606
F. Niedermayer, Nucl. Phys. B 79 (1974) 355
A. Casher, J. Kogut and L. Susskind, Phys. Rev. D 10 (1974) 732
P. Hoyer et al., Nucl. Phys. B 161 (1979) 349
A. Ali, E. Pietarinen, G. Kramer and J. Willrodt, Phys. Lett. B 93 (1980) 155

[49] F. E. Paige and S. D. Protopopescu, in Proc. UCLA Workshop, ed. H.-U. Bengtsson et. al., World Scientific (1986)

[50] R. D. Field, Nucl. Phys. B 264 (1986) 687

[51] T. Sjöstrand, Nucl. Phys. B 248 (1984) 469

[52] B. Andersson, G. Gustafson and T. Sjöstrand, Phys. Scr. 32 (1985) 574

[53] B. Andersson, G. Gustafson and C. Peterson, Zeit. f. Physik C 1 (1979) 105

[54] T. Sjöstrand, Lund University Report LU TP 95-20 (1995)

[55] G. Ingelman, in Pro. Workshop on Physics at HERA, eds. W. Buchmüller and G. Ingelman, DESY (1991)

[56] C. D. Buchanan and S. B. Chun, UCLA preprint UCLA-HEP-95-2 (1995)
S. B. Chun and C. D. Buchanan, Phys. Lett. B 308 (1993) 153

[57] T. D. Gottschalk and D. A. Morris, Nucl. Phys. B 288 (1987) 729

[58] B. R. Webber, Nucl. Phys. B 238 (1984) 492

[59] G. Marchesini and B. R. Webber, Nucl. Phys. B 238 (1984) 1
I. G. Knowles, Nucl. Phys. B 310 (1988) 571
I. G. Knowles, Comput. Phys. Commun. 58 (1990) 271
S. Catini, B. R. Webber and G. Marchesini, Nucl. Phys. B 349 (1991) 635
M. H. Seymour, Comput. Phys. Commun. 90 (1995) 95
G. Marchesini and B. R. Webber, Nucl. Phys. B 330 (1990) 261

[60] D. Buskulic et al., ALEPH Collaboration, Phys. Lett. B 384 (1996) 353

[61] R. Barate et al., ALEPH Collaboration, Zeit. f. Physik C 76 (1997) 191

[62] K. P. Das and R. C. Hwa, Phys. Lett. B 68 (1977) 459

[63] K. Ackerstaff et al., OPAL Collaboration, Euro. Physical Journal C 1 (1998) 479

[64] G. Alexander et al., OPAL Collaboration, Phys. Lett. B 388 (1996) 659

[65] P. Abreu et al., DELPHI Collaboration, Zeit. f. Physik C 70 (1996) 179

[66] P. Abreu et al., DELPHI Collaboration, Phys. Lett. B 401 (1997) 118

[67] K. Ackerstaff et al., OPAL Collaboration, CERN-EP/98-058, Sub. to Euro. Physical Journal C

[68] OPAL Collaboration, Internal Note PN 299 (1997)
Submitted to the XVIII International Symposium on Lepton-Photon Interactions, Hamburg, July 1997 and the International Europhysics Conference on High Energy Physics, Jerusalem, August 1997

[69] OPAL Collaboration, Internal Note TN 381 (1996)

[70] R. Akers et al., OPAL Collaboration, Zeit. f. Physik C 63 (1994) 197

[71] A. Böhrer, Physics Rep., 291 (1997) 107

[72] R. J. Barlow, Nucl. Instrum. Meth. A 297 (1990) 496

[73] MINUIT Manual, CERN Program Library Long Writeup D506 (1994)

[74] S. Catani et al., Phys. Lett. B 269 (1991) 432

[75] R. Akers et al., OPAL Collaboration, Zeit. f. Physik C 63 (1994) 181

[76] LEP Energy Working Group, Internal Note 97/01 (1997)

[77] D. Bardin et al., Nucl. Phys. B (Proc. Suppl.) 37 B (1994) 148
D. Bardin et al., DESY 96-233, hep-ph/9612409 (1996)

[78] OPAL Collaboration, Internal Note PN 331 (1998)

[79] G. Alexander et al., OPAL Collaboration, Zeit. f. Physik C 72 (1996) 191

[80] G. Alexander et al., OPAL Collaboration, Phys. Lett. B 376 (1996) 232

[81] S. Catani and M. H. Seymour, CERN-TH/96-28 (1996)

[82] R. K. Ellis, D. A. Ross and A. E. Terrano, Nucl. Phys. B 178 (1981) 421

[83] LEP Energy Working Group, Internal Note 98/01 (1998)

[84] Yu. L. Dokshitzer, V. A. Khoze, and S. I. Troyan, Int. J. Mod. Phys. A 7 (1992) 1875

[85] M. Z. Akrawy et al., OPAL Collaboration, Phys. Lett. B 247 (1990) 617

[86] D. Buskulic et al., ALEPH Collaboration, Zeit. f. Physik C 73 (1997) 409
P. Abreu et al., DELPHI Collaboration, Zeit. f. Physik C 73 (1997) 229
W. Braunschweig et al., TASSO Collaboration, Zeit. f. Physik C 47 (1990) 187
A. Petersen et al., MARK II Collaboration, Phys. Rev. D 37 (1988) 1
H. Aihara et al., TPC Collaboration, LBL-23727 (1988)
Y. Li et al., AMY Collaboration, Phys. Rev. D 41 (1990) 2675
D. Buskulic et al., ALEPH Collaoration, Zeit. f. Physik C 55 (1992) 209
P. Abreu et al., DELPHI Collaboration, Phys. Lett. B 275 (1992) 231
B. Adeva et al., L3 Collaboration, Phys. Lett. B 259 (1991) 199

[87] R. J. Barlow, University of Manchester, private communication

[88] J. Orear, Notes on Statistics for Physicists, University of California rep UCRL-8417 (1958)